

PHYSICS-BASED CRYSTAL PLASTICITY MODELING OF SINGLE CRYSTAL NIOBIUM

By

Tias Maiti

A DISSERTATION

Submitted to  
Michigan State University  
in partial fulfillment of the requirements  
for the degree of

Materials Science and Engineering – Doctor of Philosophy

2017

## ABSTRACT

### PHYSICS-BASED CRYSTAL PLASTICITY MODELING OF SINGLE CRYSTAL NIOBIUM

By

Tias Maiti

Crystal plasticity models based on thermally activated dislocation kinetics has been successful in predicting the deformation behavior of crystalline materials, particularly in face-centered cubic (fcc) metals. In body-centered cubic (bcc) metals success has been limited owing to ill-defined slip planes. The flow stress of a bcc metal is strongly dependent on temperature and orientation due to the non-planar splitting of  $a/2\langle 111 \rangle$  screw dislocations. As a consequence of this, bcc metals show two unique deformation characteristics: (a) thermally-activated glide of screw dislocations - the motion of screw components with their non-planar core structure at the atomistic level occurs even at low stress through the nucleation (assisted by thermal activation) and lateral propagation of dislocation kink pairs; (b) break-down of the Schmid Law, where dislocation slip is driven only by the resolved shear stress.

Since the split dislocation core has to constrict for a kink pair formation (and propagation), the non-planarity of bcc screw dislocation cores entails an influence of (shear) stress components acting on planes other than the primary glide plane on their mobility. Another consequence of the asymmetric core splitting on the glide plane is a direction-sensitive slip resistance, which is termed twinning/atwinning sense of shear and should be taken into account when developing constitutive models.

Modeling thermally-activated flow including the above-mentioned non-Schmid effects in bcc metals has been the subject of much work, starting in the 1980s and gaining increased interest in recent times. The majority of these works focus on single crystal deformation of commonly used

metals such as Iron (Fe), Molybdenum (Mo), and Tungsten (W), while very few published studies address deformation behavior in Niobium (Nb). Most of the work on Nb revolves around fitting parameters of phenomenological descriptions, which do not capture adequately the macroscopic multi-stage hardening behavior and evolution of crystallographic texture from a physical point of view. Therefore, we aim to develop a physics-based crystal plasticity model that can capture these effects as a function of grain orientations, microstructure parameters, and temperature.

To achieve this goal, first, a new dilatational constitutive model is developed for simulating the deformation of non-linear geometries (foams or geometries with free surfaces) using the spectral method. The model has been used to mimic the void-growth behavior of a biaxially loaded plate with a circular inclusion. The results show that the proposed formulation provides a much better description of void-like behavior compared to the pure elastic behavior of voids. Using the developed dilatational framework, periodic boundary conditions arising from the spectral solver has been relaxed to study the tensile deformation behavior of dogbone-shaped Nb single crystals.

Second, a dislocation density-based constitutive model with storage and recovery laws derived from Discrete Dislocation Dynamics (DDD) is implemented to model multi-stage strain hardening. The influence of pre-deformed dislocation content, dislocation interaction strengths and mean free path on stage II hardening is then simulated and compared with in-situ tensile experiments.

*I dedicate this thesis to my parents, who have always loved me unconditionally and whose good examples have taught me to work hard for the things that I aspire to achieve.*

## ACKNOWLEDGMENTS

First, I would like to express my sincere gratitude to my advisor Dr. Philip Eisenlohr for the continuous support of my Ph.D. study and related research, for his patience, motivation, and immense knowledge. His guidance helped me in all the time of research and writing of this thesis.

Besides my advisor, I would like to thank the rest of my thesis committee: Prof. Thomas Bieler, Prof. Donald Morelli, and Prof. Roozbeh Dargazany, for their insightful comments and encouragement, but also for the hard questions that gave me incentive to widen my research from various perspectives.

My sincere thanks also go to Prof. Carl Boehlert, and Prof. Martin Crimp, who provided me an opportunity to access to their laboratory and research facilities. Without the valuable support, it would not be possible to conduct this research.

I am also very grateful to Dr. Pratheek Shanthraj, Max Planck Institut für Eisenforschung GmbH, for his scientific advice and many insightful discussions and suggestions. He was my primary resource for getting my numerical questions answered and was instrumental in helping me develop constitutive models.

I thank my fellow colleagues Tridip Das, Aritra Chakraborty, Chen Zhang, Dr. Ajith Chakke-dath, and Zhuowen Zhao for the stimulating discussions and all the fun we have had in the last four years.

Last but not the least, I would like to thank my parents for the constant source of inspiration throughout writing this thesis and my life in general.

## TABLE OF CONTENTS

LIST OF TABLES . . . . .	viii
LIST OF FIGURES . . . . .	ix
CHAPTER 1 INTRODUCTION AND RESEARCH BACKGROUND . . . . .	1
1.1 Superconducting Radio Frequency Cavity . . . . .	2
1.2 Material for SRF cavity application . . . . .	4
1.3 Challenges associated with using Nb as material for SRF application . . . . .	6
1.4 Objective . . . . .	8
CHAPTER 2 PLASTIC DEFORMATION IN BODY CENTERED CUBIC METALS . . . . .	9
2.1 Slip systems in BCC crystals . . . . .	10
2.2 Orientation dependent strain hardening in BCC single crystals . . . . .	12
2.3 Non-Schmid effects . . . . .	15
2.4 Kink-pair assisted dislocation motion . . . . .	18
2.5 Temperature dependence of flow stress . . . . .	20
2.6 Overview of deformation in Nb single crystals . . . . .	23
CHAPTER 3 MODELING NON-COMPACT GEOMETRIES USING SPECTRAL METHOD . . . . .	26
3.1 Constitutive model for void like regions . . . . .	29
3.1.1 Solution to mechanical boundary value problem . . . . .	31
3.2 Comparison between a dilatational and soft elastic void . . . . .	32
3.3 Uniaxial tension of dogbone-shaped sample of oligocrystalline aluminum . . . . .	35
3.4 Selection of parameters for void material description and its associated sensitiv- ity on the simulation results . . . . .	37
CHAPTER 4 CONSTITUTIVE MODELS . . . . .	41
4.1 Phenomenological Model . . . . .	42
4.2 Dislocation density based model . . . . .	42
4.2.1 Influence of elastic anisotropy on dislocation interaction strengths . . . . .	47
4.2.2 Dislocation storage and recovery framework . . . . .	49
4.2.3 Dislocation multiplication . . . . .	52
4.2.4 Dislocation annihilation . . . . .	55
CHAPTER 5 RESULTS AND DISCUSSION . . . . .	57
5.1 Calibration of Crystal Plasticity constitutive model . . . . .	57
5.2 Phenomenological constitutive model results . . . . .	60
5.3 Dislocation density based crystal plasticity model results . . . . .	62
5.3.1 Slip activity maps as a function of orientation . . . . .	63
5.3.2 Influence of slip family on spatially resolved deformation behavior . . . . .	64
5.3.3 Model sensitivity to initial dislocation density . . . . .	66

5.3.4	Influence of dislocation interaction coefficients on strain hardening . . . . .	71
5.3.5	Inverse optimization of dislocation mean free path coefficient . . . . .	73
CHAPTER 6	CONCLUSION . . . . .	77
6.1	Recommendations for future work . . . . .	78
CHAPTER 7	ADDITIONAL PROJECTS . . . . .	80
7.1	Influence of geometric reconstruction accuracy on grain-averaged aggregate me- chanics . . . . .	80
7.1.1	Introduction . . . . .	80
7.1.2	Spatial reconstruction method . . . . .	82
7.1.3	Volume statistics of real and artificial grain structures . . . . .	83
7.1.4	Comparison of 3D reconstruction of grain aggregates in presence/absence of grain volume information . . . . .	86
7.1.5	Grain averaged lattice strains of reconstructed structures . . . . .	89
7.1.6	Discussion . . . . .	94
7.2	Cumulative volume fraction of log-normal grain size distributions . . . . .	96
7.3	Grain size normalization . . . . .	96
7.4	Generation of synthetic grain structures . . . . .	97
BIBLIOGRAPHY	. . . . .	98

## LIST OF TABLES

Table 1.1: Superconducting properties of some promising materials for SRF applications. . . . .	5
Table 3.1: Material parameters; elastic constants $C_{ij}$ , reference strainrate $\dot{\epsilon}_0$ , stress exponent $n$ , initial and saturation flowstress $\tau_0$ and $g_\infty$ , hardening parameters $h_0$ and $a$ , and Taylor factor $M = 3$ . . . . .	33
Table 4.1: Material variables for Peirce et al. [1] model; elastic constants $C_{ij}$ , reference shear rate $\dot{\gamma}_0$ , stress exponent $n$ , initial and saturation slip resistance $\tau_0^\xi$ and $g_\infty^\xi$ , hardening parameters $h_0, q^{\xi\beta}$ , and $a$ . . . . .	43
Table 4.2: Dislocation interaction matrix in BCC lattice. . . . .	46
Table 4.3: Types of possible interaction in BCC lattice [2] . . . . .	46
Table 4.4: Modified dislocation interaction matrix in BCC lattice taking into account asymmetric junction configurations [3]. . . . .	48
Table 4.5: Types of possible interaction in BCC lattice with asymmetric junction configurations [3]. . . . .	49
Table 4.6: Material variables for dislocation density based model . . . . .	56
Table 5.1: Comparison of CPFFT computation time between simplified reduced geometry of gauge section and a proper dogbone shaped geometry. Material described by crystal plasticity law is shown in blue and the dilatational buffer layer is shown in light gray. . . . .	59
Table 5.2: Constitutive material parameters of pure Nb used for the crystal plasticity simulations of uniaxial tension. The asterisk (*) indicates fitting parameters. . . . .	63
Table 5.3: Variability in constitutive parameter values resulting from minimizing the deviation in single crystal stress–strain response for eight distinct tensile directions. . . . .	75
Table 7.1: Material parameters; elastic constants $C_{ab}$ , reference shear rate $\dot{\gamma}_0$ , stress exponent $n$ , initial and saturation slip resistance $\tau_0$ and $g_\infty$ , hardening parameters $h_0, q^{\xi\beta}$ , and $a$ . . . . .	91
Table 7.2: DREAM.3D pipeline for generating synthetic grain structures. . . . .	97

## LIST OF FIGURES

Figure 1.1:	A typical accelerating cavity geometry, showing particle beam and fundamental fields of the RF cavity. . . . .	3
Figure 1.2:	Mechanical fabrication path of an SRF cavity. . . . .	7
Figure 1.3:	Surface defects in a well prepared SRF cavity cell. . . . .	7
Figure 2.1:	Potential slip systems in BCC lattice . . . . .	10
Figure 2.2:	Areas of activation of the 110 and 112 planes in the standard triangle [4] . . . .	11
Figure 2.3:	Shear stress – shear strain curves as a function of orientation in $\alpha - Fe$ (top) and Nb (bottom), according to [5, 6]. . . . .	12
Figure 2.4:	Schematic illustration of Taylors angles $\chi$ and $\phi$ . The loading direction is marked in the standard triangle by the angles $\chi$ and $\phi$ [7] . . . . .	13
Figure 2.5:	Influence of the orientation of the load on the shear stress-strain curves with slip only in $\{110\}$ system. (Left) effect of angle $\phi$ , (Right) effect of angle $\chi$ [7].	15
Figure 2.6:	Evolution of lattice reorientation with plastic deformation depending on the initial orientation [8, 9, 10]. . . . .	16
Figure 2.7:	Illustration showing core configuration of screw dislocations in a BCC lattice .	17
Figure 2.8:	Intrinsic lattice resistance (Peierls-Nabarro Barrier) to slip in BCC materials. . .	19
Figure 2.9:	Temperature dependence of flow stress, slip mechanisms (schematics) in pure BCC metals (Mo) [11]. . . . .	21
Figure 2.10:	Surface topography of deformed single crystal Nb [12] . . . . .	24
Figure 2.11:	In situ uniaxial tensile test results reported by Baars [12]. Left : Inverse pole figure showing rotation of tensile axis as a function of orientation for as-cast samples. Center: axial stress–strain curves for the as-cast samples with same orientations in the left inverse pole figure map. Right : axial stress–strain curves for the annealed samples with the same orientations. . . . .	24
Figure 3.1:	Multiplicative decomposition of deformation gradient [13] . . . . .	27
Figure 3.2:	Schematic diagram showing calculation of $\mathbf{S}$ as a function of $\mathbf{F}$ . . . . .	28

Figure 3.3:	Schematics of VON MISES plasticity model in principle stress space. The state of stress at a material point is represented by the vector $\mathbf{s}$ (black), which can be additively decomposed into the pressure vector $\mathbf{p}$ (red) and the deviatoric stress vector $\mathbf{s}'$ (green). The light green surface represents the yield surface of the material point. . . . .	32
Figure 3.4:	Comparison of mechanical field maps of a (fully periodic) two-dimensional plastic plate containing a circular inclusion of area fraction 0.8 % and loaded biaxially to an average deformation of $\langle F_{xx} \rangle = \langle F_{yy} \rangle = 1.4$ . Void volume is described by an isotropic elastic material model (left, “elastic”) or by an isotropic phenomenological plasticity model with dilatational capabilities (right, “dilatational”). The stiffness of the inclusion in the elastic case is set to be 1000× softer than the plate. . . . .	34
Figure 3.5:	Influence of external boundary conditions on in-plane VON MISES strain fields and lattice reorientation. Simulated geometries with fully periodic gauge section of dog-bone (first row), quasi-periodic, i.e. periodic along the thickness direction (second row), and free surfaces normal to $x$ and $z$ (third and last row) compared to experimental results measured by DIC and EBSD (fourth row, from [14]). Gray (green) semi-transparent volume in the simulated domain column uses the proposed dilatational (isotropically elastic) material model; regions of constant color reflect individual grains. Inverse pole figure (IPF, last column) coloring of lab direction $z$ is mapped on the undeformed configuration, except for the measured result (fourth row). . . . .	39
Figure 3.6:	Computational cost (top right) and void representation quality (bottom) of the elastic and the dilatational material model for the case of biaxial expansion of a hole in a plastic plate (top left) up to $\langle F_{xx} \rangle = \langle F_{yy} \rangle = 1.2$ . Strain evolution of median interface traction (lower left, collected from voxels immediately inside and outside of interface, i.e. blue and red ring at top left) indicates the void is reaching the flow stress level ( $\approx Mg$ ) of the surrounding plate in case of the elastic and strongest dilatational material (plastic strength ratio of $10^0$ ); softer dilatational cases (darker red) saturate much earlier at flow stress levels far below the plate flow stress (plastic strength ratio of $10^{-1}$ and $10^{-2}$ ). Median interface tractions collected at $\langle F_{xx} \rangle = \langle F_{yy} \rangle = 1.2$ (bottom right) confirm marginal influence of elastic stiffness on void representation quality for the dilatational material. . . . .	40
Figure 4.1:	A schematic figure showing dislocation reaction between segments on active slip-system $\xi$ (blue) and a forest system $\beta$ (red). . . . .	52
Figure 5.1:	Left : Optimization function minimizing the area between two curves. The gray line represents the standard curve, which the dashed black line represents the trial curve. Right : Flow diagram of the optimization process used by Chakraborty and Eisenlohr [15]. . . . .	58

Figure 5.2: Comparison of stress components of simplified reduced geometry and gauge length section of dogbone geometry in terms of kernel density estimation maps. The top row shows the correlation of the normal stress components and the bottom row shows the correlation of shear stress components. . . . .	60
Figure 5.3: Comparison of experimentally observed axial stress-curves with the ones predicted using phenomenological crystal plasticity model as function of orientation. Solid lines indicate the measured stress-strain curves while the predicted ones are shown in dashed lines. . . . .	61
Figure 5.4: Adjustable phenomenological model parameters (initial CRSS $\tau_0$ saturation CRSS $g_\infty$ and hardening slope $h_0$ ) for pure Niobium obtained from stress-strain curve optimization of 8 single crystal orientations. The crosses represent a parameter for a particular orientation. The mean of the parameters for all orientations is represented by a solid dot. . . . .	62
Figure 5.5: Active slip family based on net accumulated shear $\Gamma_{acc}$ as a function of orientation. The contribution of a slip family for each of the orientations is represented by a color varying from blue for pure $\{112\}$ to red for pure $\{110\}$ slip. Left: active slip family maps at $\epsilon \sim 0.002$ . Right: active slip family maps at $\epsilon \sim 0.050$ . . . . .	64
Figure 5.6: Local $\langle 010 \rangle$ lattice reorientations maps of the deformed dogbone samples. Rows in descending order represent the simulation results obtained assuming $\{110\}$ , $\{110\}$ - $\{112\}$ and $\{112\}$ slip family respectively. . . . .	65
Figure 5.7: Local von Mises strain $\epsilon_{vM}$ maps of the deformed dogbone samples. Rows in descending order represent the simulation results obtained assuming $\{110\}$ , $\{110\}$ - $\{112\}$ and $\{112\}$ slip family respectively. . . . .	66
Figure 5.8: Local von Mises stress $\sigma_{vM}$ maps of the deformed dogbone samples. Rows in descending order represent the simulation results obtained assuming $\{110\}$ , $\{110\}$ - $\{112\}$ and $\{112\}$ slip family respectively. . . . .	67
Figure 5.9: Influence of pre-deformed dislocation content on stress-strain response (lower left) simulated by dislocation density based model. The top row shows several instances of inhomogeneous distribution of dislocation content on individual slip systems for a chosen log-normal dislocation statistics. Each slip system is denoted by a color key given in the lower right legend. . . . .	68

Figure 5.10: Influence of pre-deformed dislocation content on lattice reorientation for three different orientations simulated by dislocation density based model. The left column shows the probability distribution of pre-deformed dislocation content with $\rho^m = 1 \times 10^{13} \text{ m}^{-2}$ and different variances. The corresponding lattice reorientation trajectories for three orientations are shown in the right three columns. . . . .	70
Figure 5.11: Results predicted by the dislocation density based model with isotropic $\alpha - Fe$ interaction coefficients. Left: $\langle 010 \rangle$ inverse pole figure for the 8 orientations showing the tensile axis re-orientation as a function of strain ( $\epsilon_{\text{max}} = 0.30$ ). The initial tensile axis orientation is denoted by the blue dot. The final orientation after 30 % strain is indicated by the red dot. The black dots in-between represents the trajectory of reorientation. Right: Corresponding axial stress-strain ( $\sigma - \epsilon$ ) predicted by the crystal plasticity model. . . . .	71
Figure 5.12: Influence of elastic anisotropy on strain hardening behavior for a particular orientation. The interaction coefficients for Fe assuming isotropic elasticity was calculated by Queyreau et al. [2]. The dislocation interaction coefficients assuming anisotropic elastic for Nb was taken from the works of Madec and Kubin [3]. . . . .	72
Figure 5.13: Comparison of experimentally observed (solid) and predicted (dashed) uniaxial stress–strain response for different orientations. The coefficients for mean free path $K_{hkl}$ and dynamic recovery $y_{hkl}$ in the model by Devincre et al. [16] were estimated using inverse optimization of the measured stress–strain curves. . . . .	74
Figure 5.14: Variability in predicted single–crystal response under unidirectional tension due to different distributions among the slip systems for fixed total initial dislocation content. . . . .	76
Figure 7.1: Polycrystalline aggregates (a) measured by various 3D techniques [17, 18, 19, 20] and associated grain statistics (blue curves in (b) and (c)). Sequence of four gray curves represents log-normal grain volume distributions of different variance (Eq. (7.9)); the black curve corresponds to closest fit at variance $\sigma_{\text{distr}} = 1.2$ . Dotted line represents average grain volume. . . . .	83
Figure 7.2: Synthetic polycrystals (a) generated by DREAM.3D [21, 22] using cube octahedra (top row) or super ellipsoids (bottom row) as grain shapes. Orange and brown curves in (b) and (c) show the associated grain statistics for both selections of grain shapes. Black line (optimal fit to experimental data) is same as in Fig. 7.1. . . . .	84

Figure 7.3: Ratio of largest to smallest principal moment of inertia (‘shape factor’) for all cube octahedral (orange) and super ellipsoidal (brown) grains. Solid lines correspond to synthetic (reference) structures shown in Fig. 7.2(a). The fainter curves result after reconstructing the reference structures using either grain volumes (dashed) or centroid distances (dotted) as a basis for Laguerre tessellation weights. In general, cube octahedral grain structures are closer to being equiaxed than those based on super ellipsoids. . . . . 86

Figure 7.4: Joint probability of correct grain volume (normalized by average grain size) and relative deviation in the reconstructed grain volume  $V_{\text{tess}}/V_{\text{ref}}$  or grain shape factor  $\kappa_{\text{tess}}/\kappa_{\text{ref}}$ . Grain reconstruction uses Laguerre tessellation with grain centroids as seed positions. Seed point weights are derived from known grain volumes (upper half) or estimated from the distance to the nearest grain centroid (lower half). Left and right panels correspond to cube hexahedral and super ellipsoidal grain shapes, respectively, that were used in generating the underlying synthetic data sets (Fig. 7.2(a)). Red maps correspond to direct use of grain centroids as seed positions, while green maps illustrate changes due to a seed position adjustment [23] that considers the new centroid location of each resulting tessellated grain. The comparisons of shape factor deviations (yellow maps) utilized only those latter reconstructed structures. . . . . 88

Figure 7.5: Deviations of normal, shear, and deviatoric normal components of grain-averaged Cauchy stress  $\sigma_{\text{tess}}$  in reconstructed grain structures relative to corresponding stress components  $\sigma_{\text{ref}}$  resulting in the (cube octahedron) reference grain structures. Tessellations in upper panel employ known grain volume information ( $r_{\text{equiv}}$ ) for Laguerre weights, while in lower panel the nearest centroid distances ( $d_{\text{nn}}$ ) are used instead. The seed positions were adjusted [23] in both tessellation alternatives. . . . . 90

Figure 7.6: Joint probability of volume  $V_{\text{ref}}$  of synthetic grains and the distance  $d_{\text{nn}}$  from each grain centroid to the nearest neighboring one. Quantities are normalized by the average grain volume  $\langle V_{\text{ref}} \rangle$  and its equivalent radius  $r_{\text{equiv}} = (3\langle V_{\text{ref}} \rangle / 4\pi)^{1/3}$ , respectively. Cumulative probability is scaled to unity within each (vertical) bin of normalized grain volume. Centroid distance progressively deviates from expected relation (dashed line) with decreasing volume of grain, resulting in a weak correlation between the distance to the nearest grain centroid and the volume of a grain. . . . . 93

Figure 7.7: Joint probability of stress magnitudes  $\sigma_{\text{ref}}$  in reference structure and relative deviations  $\sigma_{\text{tess}}/\sigma_{\text{ref}}$  combined from both tessellated structures. Cumulative probability is scaled to unity within each bin of stress magnitudes. Solid lines exemplify relative deviations in stress due to absolute differences of 5 MPa and 10 MPa. With increase in magnitude of stress, the relative deviations in stress due to difference in grain morphologies diminishes. . . . . 95

## CHAPTER 1

### INTRODUCTION AND RESEARCH BACKGROUND

Advancements in particle physics rely heavily on advances in particle accelerators. Originally, particle accelerators were developed to do fundamental research in sub-atomic particle physics: the study of the elemental forces and building blocks of matter. Today, many diverse real life applications make use of particle accelerators, such as in life sciences, chemistry, medical diagnosis and treatment, material characterization, and luggage interrogation for homeland security defense applications. A few of the ongoing projects based on particle accelerator technology involves x-ray laser oscillators, continuous wave (CW) and pulsed free electron lasers, energy recovery linac (ERL) based light sources, electrons and ions colliders, nuclear waste transmutation, and accelerator driven systems (ADS) for medical isotope production. Researchers are working on developing a new type of nuclear reactors based on particle accelerators, which could solve the nuclear waste disposal problem.

Many parameters influence the performance of the accelerator, and the physics they make accessible. A critical parameter among them is the energy of the particle beams. Particle beams of higher energy allow for finer measurement of the fundamental properties of the particles constituting them. The technology for accelerating particles also depends on the type of particle being accelerated. Heavy particle (proton) accelerators are mostly circular machines, with their technological challenges lying in the area of high field magnet development. The Tevatron, at Fermilab, and the Large Hadron Collider (LHC) at Conseil Européen pour la Recherche Nucléaire (CERN) are examples of these type of machines. Electron-positron colliders have been almost exclusively circular machines up to the present. The synchrotron radiation which results from accelerating

charged particles in a circle makes circular machines impractical for further increase in energy. For this reason, the next generation of electron-positron colliders will have to be linear. A linear collider with the center of mass energy in the 1 TeV range would be a machine complementary to the previously mentioned LHC. Several proposals have been put forward for the construction of such a device, [24, 25] one of which would be a Super conducting Radio Frequency (SRF) based machine. These SRF based machines are composed of smaller units stacked in series known as SRF cavities or cells.

## 1.1 Superconducting Radio Frequency Cavity

An SRF cavity is a device in which particles are accelerated by a resonating radio wave. In most electron-positron colliders, cavities are microwave resonators of "toroidal" shape connected by tubes, to allow particles to accelerate through them. Fig. 1.1 shows a schematic of a typical cylindrically symmetric cavity for lowest RF frequency mode (TM 010). The electrical and magnetic fields lines are depicted by arrows and crosses respectively. The electric field is parallel to the beam axis and decays to zero radially upon approaching the cavity walls. Boundary conditions demand that the electric field is normal to the surface of the cavity cell with the peak being located near the iris or the region where the cavity is attached to the connecting tubes. The magnetic field runs in the azimuthal direction, with the highest magnetic field located near the equator of the cavity and diminishing towards the cavity axis.

As the particle beam traverses through the cavity, it experiences an acceleration along the axis of the cavity due to the electric field. Since the RF fields alternate in time, the particle beam must be in the proper phase with the fields so that the force is accelerating in nature rather than decelerating. As the particles take a finite time to travel through the cavity, the accelerating field is

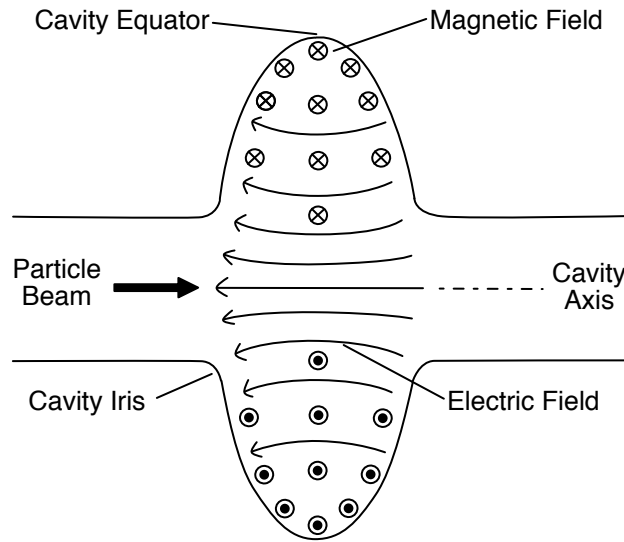


Figure 1.1: A typical accelerating cavity geometry, showing particle beam and fundamental fields of the RF cavity.

considered as the time average of the electric field along the particle path.

Surface currents in mega Ampere (MA) range are required to flow through the metal walls of the cavity structure to achieve the desired accelerating field of  $1 \cdot 10^6 \text{ V m}^{-1}$ . Such huge surface currents produce an enormous amount of heat in a normally conducting metal such as copper, which is costly to cool. Also, the cavity structure near the particle beam has disruptive effects on it, limiting its density and thereby restricting the accelerator's use for modern day applications. These detrimental effects can be overcome by the use of superconducting cavities. When cooled below a critical temperature  $T_c$ , many materials lose all of its Direct Current (DC) electrical resistance. These materials are known as superconductors. Below  $T_c$ , the electrons of a conducting material gain a small net attraction through their interaction with the surrounding lattice. As a result, the electrons form "Cooper pairs" which move through the lattice without any resistance. The superiority of superconducting cavities over those made of normal-conducting metal is in its ability to store a large amount of energy with much lower dissipation.

To determine which materials are suitable for producing high-performing SRF cavities, one should look for certain properties. One of them being the Quality factor  $Q_0$  measuring the performance of a SRF cavity. The Quality factor is given as,

$$Q_0 = \frac{G}{R_s} \quad (1.1)$$

where  $G$  is a parameter, which depends on the cavity geometry and  $R_s$  is the average surface resistance of the inner cavity walls (function of the accelerating gradient,  $E_{acc}$ ). In order to reach the theoretical limit of current and future accelerators, increasing the quality factor and accelerating gradient is one of the main topics of research on SRF cavities. For a large  $E_{acc}$ , a large superheating field  $B_{sh}$  is desirable, as it is the relevant critical field for RF applications. In SRF cavities, the objective is to exclude flux, not to pin it inside the superconductor. Pinned normal conducting vortex cores dissipate energy strongly in RF fields.

It is energetically favorable for the vortices to be inside the superconductor above the first critical field  $B_c^1$ , and only an energy barrier prevents the flux penetration above this field. For an ideal surface, the barrier disappears at  $B_{sh}$ , making it the ultimate limit for SRF applications. Surface defects of size on the order of the coherence length  $\xi$  (spatial amplitude of the superconducting wave function) can reduce the barrier to vortex penetration. Thus, the fields close to  $B_{sh}$  cannot be realized without vortex entry. Therefore it is important to have a large enough  $\xi$  so that the performance is not affected by the presence of small defects even on a well-prepared surface, such as grain boundaries. How large of  $\xi$  is large enough, is still an open question.

## 1.2 Material for SRF cavity application

For an optimum cavity operation, the building material must possess the following attributes:

- Easy to fabricate in a way that it conforms to a complex geometry.
- High thermal conductivity or be able to be deposited on a substrate with high thermal conductivity to evade thermal breakdown
- Minimal surface defects to prevent field emissions.
- Less prone to surface contamination upon cleaning.

Table 1.1: Superconducting properties of some promising materials for SRF applications.

<b>Material</b>	$\lambda(\mathbf{0})$ [nm]	$\xi(\mathbf{0})$ [nm]	$\mathbf{B}_{sh}$ [mT]	$\mathbf{T}_c$ [K]	$\rho_n$ [ $\mu\Omega\text{cm}$ ]
<b>Nb<sub>3</sub>Sn</b> [26]	111	4.2	410	18	8
<b>MgB<sub>2</sub></b> [27, 28]	185	4.9	210	40	0.1
<b>NbN</b> [29]	375	2.9	160	16	144
<b>Nb</b> [30]	50	22	210	9.2	2

The superconducting properties of four promising SRF cavity materials are listed in Table 1.1. Nb<sub>3</sub>Sn is a material with an enormous potential for SRF applications. It has a large  $T_c \sim 18\text{ K}$  (twice that of niobium). However, Nb<sub>3</sub>Sn is brittle and has low thermal conductivity, which limits it to be used in a film form. Therefore it faces challenges associated with thin films in SRF Cavity applications. MgB<sub>2</sub> is another alternative that was discovered recently. It has a  $T_c$  of approximately 40 K, but it is not as well developed as Nb<sub>3</sub>Sn. The challenges here lies in obtaining a minimal oxygen background in the coating chamber to fabricate MgB<sub>2</sub>, as magnesium is highly reactive with it. The  $\delta$  phase of NbN also has the potential to be a SRF material, with a high  $T_c$  of 15–17 K. NbN has a very complex phase diagram, which makes it very challenging to achieve the superconducting delta phase during fabrication. Some success has been achieved with sputtering,

but with heat treatment in a nitrogen atmosphere, no reliable procedure has been developed that could be applied to cavities.

Niobium is currently the material of choice for superconducting cavities. It has been an essential transition metal because of its uses in the manufacturing of stainless steels and superalloys for aerospace applications [31]. The primary reason for the choice of niobium as an SRF material is due to its highest critical transition temperature ( $T_c = 9.2$  K) of all pure metals, and it is relatively easy to fabricate. Also, it is readily available and has a high thermal conductivity. None of the materials mentioned earlier can match niobium in terms of its ease of use and performance with increasing RF fields. For a typical cavity made of Nb, the resonating frequencies fall in range 0.5–2.0 GHz operating at a temperature of  $\sim 2.0$  K. The quality factor for such a cavity is about  $10^{10}$ – $10^{11}$  range [32].

### **1.3 Challenges associated with using Nb as material for SRF application**

High purity Niobium ingots are produced using high-vacuum multiple electron beam melting process which results in a large-grain structure in the center and smaller columnar grains at the periphery of the 20–30 cm diameter ingots. Sheets and tubes are produced by rolling and forging these ingots, resulting in a polycrystalline microstructure. However, homogenizing this microstructure is difficult, since each of the few large and differently oriented grains responds in a strongly anisotropic way to the deformation process, which causes variability in the crystallographic texture of different batches of rolled niobium sheets [33]. Other problems associated with polycrystalline Nb include magnetic flux pinning and phonon scattering near grain boundaries. To mitigate these problems cavities can be made from wire cut slices of large-grain Nb ingots containing a handful of single crystals.

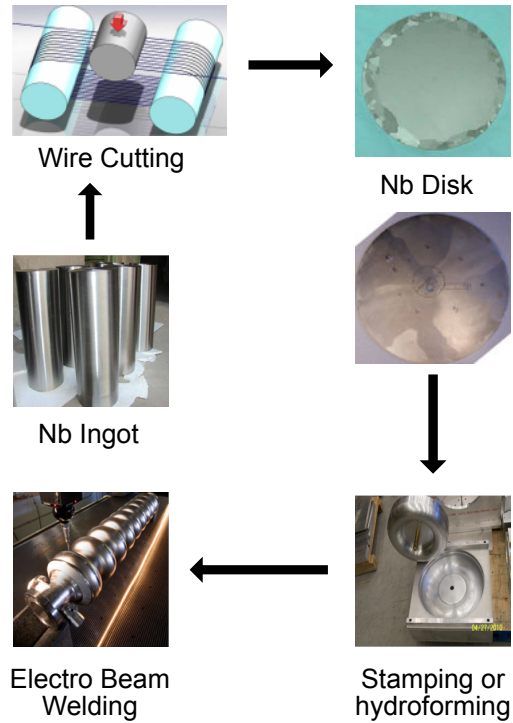


Figure 1.2: Mechanical fabrication path of an SRF cavity.



Figure 1.3: Surface defects in a well prepared SRF cavity cell.

A typical work-flow of an SRF cavity fabrication process is shown in Fig. 1.2[34, 35]. The inherent deformation anisotropy of the individual grains leads to variability in the forming process (see Fig. 1.3[34, 36, 37]). Deformation paths involving surface working, such as spinning, introduce gradients of deformation from the surface inward, with a higher density of defects near the surface. These defects act as hot-spots for electric field emission and subsequent thermal breakdown [38, 39]. Thus, to gain precise control of the forming process, it is essential to understand

the mesoscopic deformation behavior in terms of stresses necessary to activate dislocation slip on various slip systems, and the resulting work hardening behavior from the interaction of dislocations in them. Identification of these criteria are important for predicting how crystal orientations and flow behavior will evolve in more complex forming operations.

## **1.4 Objective**

The primary objective of this thesis is to develop a finite strain crystal plasticity model at mesoscopic scale for predictions of strain hardening and lattice reorientation in pure Niobium over a broad range crystal orientations. To achieve this goal, the boundary value problem associated with mechanical testing of materials is solved computationally. A new dilatational constitutive model is introduced into the finite strain framework (described in Chapter 3) for simulating deformation of non-compact geometries using a FOURIER-based spectral method. The developed constitutive model is then used to mimic free-surface boundary conditions within a periodic hexahedral cell, thus providing a way to test constitutive models for single crystal on a standard dogbone shaped geometry. In Chapter 4, a physics based crystal plasticity model is combined with internal state evolution laws consistent with Discrete Dislocation Dynamics (DDD). Parameters critical for simulating multi-stage strain hardening are identified and discussed. Finally, in chapter 5, the developed finite strain framework combined with a DDD informed physics-based model makes it is possible to successfully predict multistage hardening and crystal rotation with respect to the tensile axis as a function of crystal orientation at finite strain levels.

## CHAPTER 2

### PLASTIC DEFORMATION IN BODY CENTERED CUBIC METALS

Deformation by slip in crystalline materials occurs by movement of dislocations in certain crystallographic planes along certain crystallographic directions. Generally, these are crystallographic planes lattice planes with high planar density. For example, in Face Centered Cubic (FCC) crystals, dislocations move on  $\{111\}$  slip planes and along  $\langle 110 \rangle$  slip directions. These high density planes together with a tightly packed direction constitute a slip system. When shear stresses in a particular slip system exceed a threshold stress, a dislocation starts moving on those systems. This threshold stress, in general, is constant for a particular slip system and is independent of the direction of slip [40]. Deformation takes place on those systems which offer the least resistance to the dislocation motion, which is observed macroscopically by the formation of slip traces (slip step) on a polished surface after deformation. In other words, the slip system that has the maximum resolved shear stress will be favorable for slip. This orientation dependence of resolved shear stress is known as the Schmid law [40] and have been extensively verified for  $\{111\}\langle 110 \rangle$  systems in FCC and basal slip systems  $\{0001\}\langle 1120 \rangle$  in Hexagonally Packed (HP) metals.

Niobium exists in the Body Centered Cubic (BCC) crystal structure from  $T = 0\text{K}$  to its melting point. Therefore, to predict the deformation behavior of pure Niobium, it is important to have a detailed knowledge of the crystal structure of the material. The first part of this chapter will therefore concentrate on describing the deformation behavior BCC metals in general. Then, in the second part, the characteristics of dislocation microstructure in a BCC lattice will be detailed.

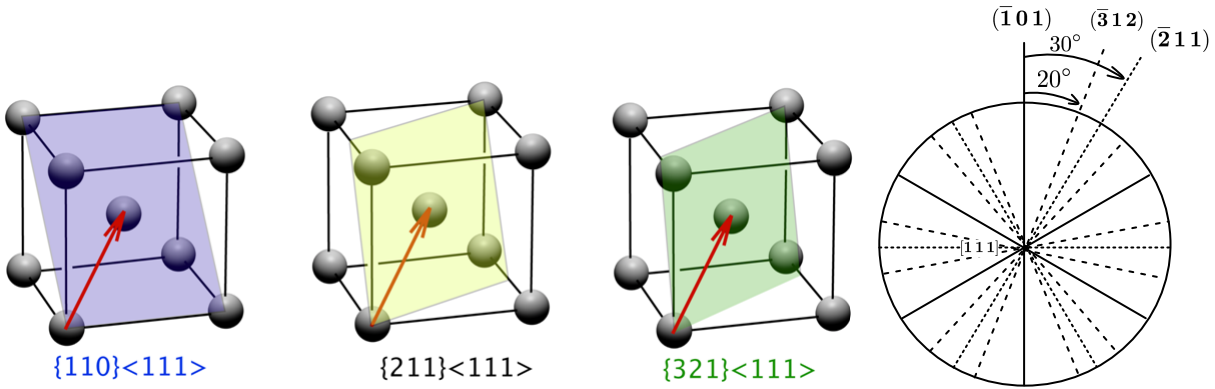


Figure 2.1: Potential slip systems in BCC lattice

## 2.1 Slip systems in BCC crystals

The question of slip systems in BCC metals has long been the subject of research since earlier times. The direction of slip is always observed to be the  $\langle 111 \rangle$  direction [41] of the BCC structure, but no conclusive evidence of the slip plane has been reported. There are, however, three major points of view in the literature concerning slip planes. Early studies of iron single crystals first suggested that slip occurs on  $\{110\}$ ,  $\{112\}$  as well as  $\{123\}$  planes, which are in the zone of the slip direction  $\langle 111 \rangle$  [42, 43, 44, 45]. Other authors then reported that the slip did not occur on planes of low indices, but took place on planes close to the Maximum Resolved Shear Stress Plane (MRSSP) [46]. This theory is often referred to as non-crystallographic glide. These two ideas of slip in iron are mainly based on the observation of visible slip traces. But as shown in Fig. 2.1 (right), the projections of the different planes available for slip along the slip direction are quite close. The planes closest to the families  $\{112\}$ , and  $\{123\}$  are separated only by  $10^\circ$ . It is therefore clear that the proximity and the multiplicity of the available slip planes make the interpretations of the slip traces rather delicate. Also, they are often very winding and branched. This observation has consequently given rise to a third proposition according to which the macroscopic

slip traces, which at first sight coincide with a plane  $\{123\}$  [47], are in fact composed of short slip traces on planes of the family  $\{110\}$  [48, 49, 50, 4].

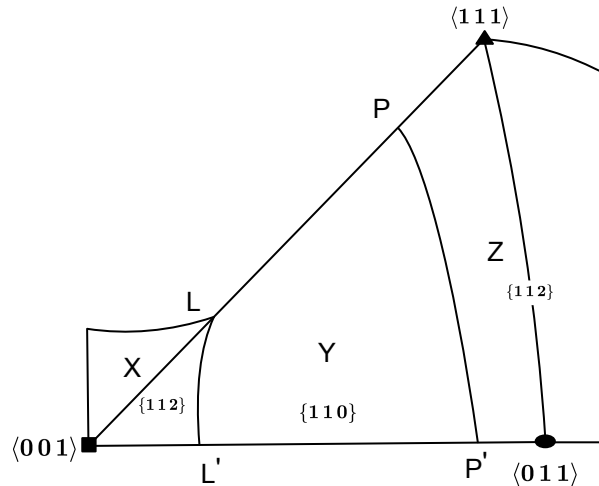


Figure 2.2: Areas of activation of the 110 and 112 planes in the standard triangle [4]

Franciosi [4], Duesbery and Foxall [10] defined the activation zones for slip families  $\{110\}$  and  $\{112\}$  in the standard triangle (see Fig. 2.2). For this purpose, they have compared the Schmid factors of the two families of planes, assuming that the critical constraints on each of them are equivalent. These authors thus show the existence of three activation domains: the Y domain, which is the most extensive, corresponds to the activation of a  $\{110\}$  plane system, and the X and Z domains coinciding with the zones of activation of a  $\{112\}$  system. The particular loading directions which lie on the boundary between two different activation domains is equivalent to the simultaneous activation of two systems, as was already the case with a single family of sliding planes. For example, loading on LP leads to the activation of two systems of the family of planes  $\{110\}$ , loading along the boundaries LL' or PP' induces the activation of two systems of different natures  $\{110\}$  and  $\{112\}$ . The same authors also carried out tensile tests to verify the position of these three domains and the mixed boundaries separating them (LL' and PP'). Franciosi [4]

states that he confirmed the existence of some of these boundaries through the observation of slip traces. The only exception was for a loading close to the PP' border. The double mixed slip on the expected  $\{110\}$  and  $\{112\}$  systems has not been observed in favor of a simple slip on a  $\{110\}$  system.

## 2.2 Orientation dependent strain hardening in BCC single crystals

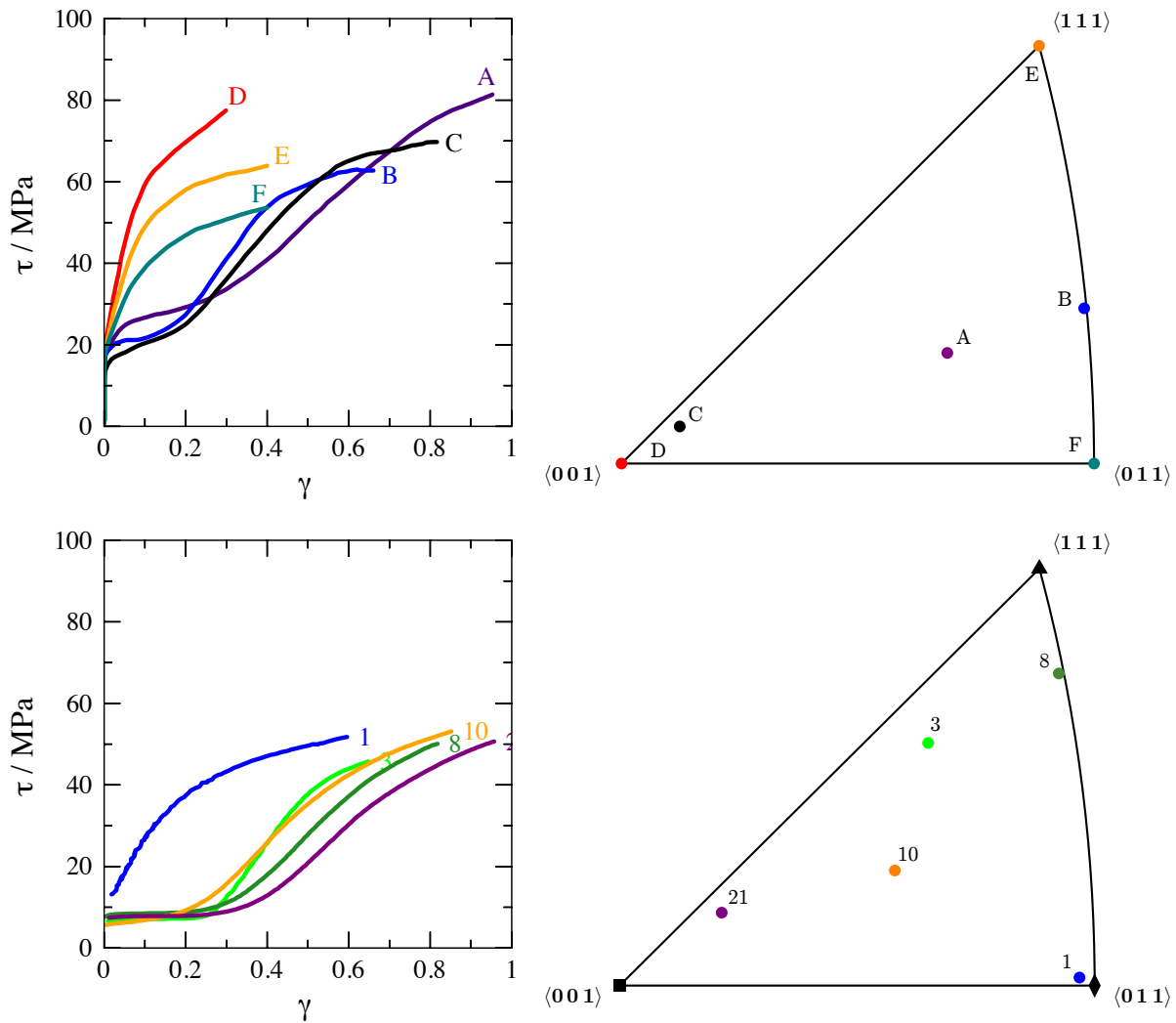


Figure 2.3: Shear stress – shear strain curves as a function of orientation in  $\alpha$  – Fe (top) and Nb (bottom), according to [5, 6].

In BCC single crystals two different types of deformation behavior are reported at strain-rate

independent temperatures. Fig. 2.3 shows several uniaxial tension deformation curves obtained in pure Iron and Niobium at ambient temperature by Spitzig and Keh, and Keh and Nakada [5, 6, 10]. Most of the tensile axis within the standard stereographic triangle show well-known three-stage stress-strain behavior (curves A, B, C, 10, and 3 in Fig. 2.3). Loading directions close to the high symmetry orientations, such as  $[001]$ ,  $[111]$  and  $[011]$ , show pseudo-parabolic behavior (curves D, E, F, and 1 of Fig. 2.3). In these orientations, slip operates on several systems from the beginning of the plastic deformation, which is responsible for a very high rate of hardening. The comparison of the three curves D, E and F (top row Fig. 2.3) leads to a prioritization of the hardening between the orientations of high symmetry. Thus the hardening is decreasing for the loadings in the order  $\{001\}$ ,  $\{011\}$ , and  $\{111\}$ . This hierarchy has also been observed by other authors [9, 8] and depends on the number of systems involved.

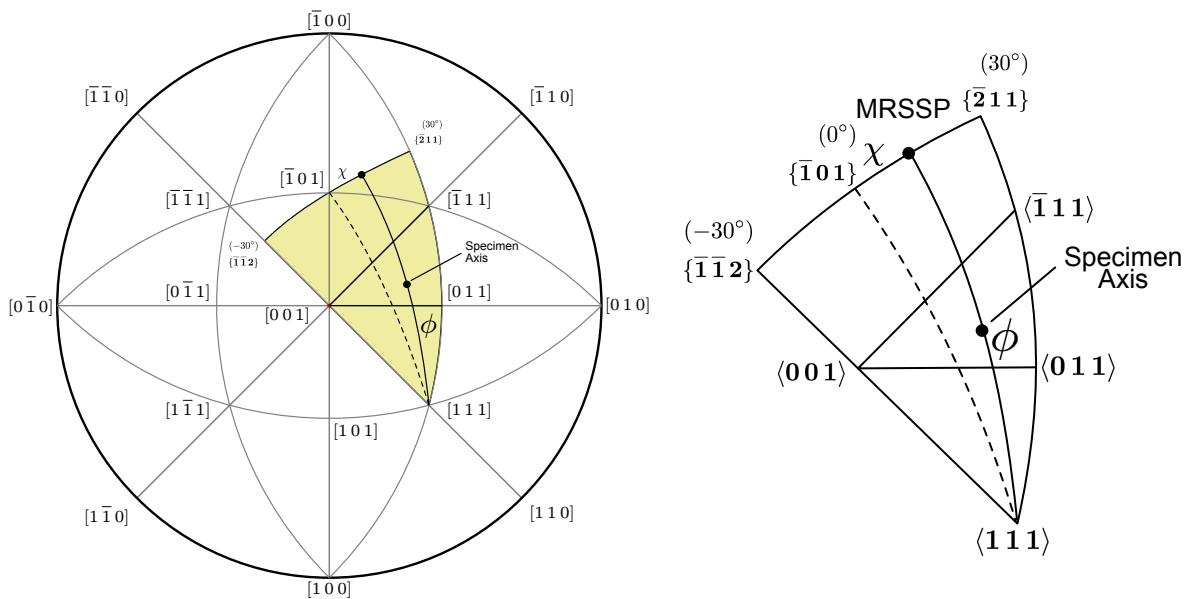


Figure 2.4: Schematic illustration of Taylor's angles  $\chi$  and  $\phi$ . The loading direction is marked in the standard triangle by the angles  $\chi$  and  $\phi$  [7]

In addition to the type and number of slip systems, the loading direction also affects the shape

of the three-stage curves as shown by a number of studies on this subject. This is a substantial effect, as the degree of hardening and the length of the stages are modified. There are few studies in which systematic identification of the direction of loading in the standard triangle by two angles  $\chi$  and  $\phi$  (see Fig. 2.4) are defined [49, 5, 7].  $\chi$  is the angle between the MRSSP and the plane (101), while  $\phi$  is the angle between the load direction and the boundary [001] - [011]. Most of these works were done in materials with dominant {110} slip behavior. The effect of angle  $\chi$  has been somewhat discussed [49, 5, 7] in comparison with the angle  $\phi$  [6, 7]. The results obtained by Kumagai et al. [7] are given in Fig. 2.5. The length of stage I increases with the angle  $\phi$ , while the degree of hardening of stage II decreases. The rate of work-hardening is lowered from  $\mu/600$  (curve A) to  $\mu/1000$  (curve C). The results obtained by [6] are similar. The elongation of stage I with  $\phi$  is often explained by the rotation of the loading direction with the plastic deformation.

Jaoul and Gonzalez [8], Keh [9], Duesbery and Foxall [10] identified the initial and final orientations of the loading direction during their tensile tests. A synthesis of their results is proposed in the standard triangle in Fig. 2.6. Under simple slip conditions on a plane {110}, the loading direction turns in the slip direction, which is [111] in the example figure. Upon reaching the [001] - [011] boundary, the activation of a second system should, in theory, turn the loading towards the [011] axis. However, this is not always the case, since the direction of loading exceeds the boundary (or overshoot) by sometimes  $6^\circ$  to  $10^\circ$  [8, 9, 7, 10]. The reason for these overruns is not well understood yet. A loading along the [111] - [011] boundary, is directed towards the [011] direction while loading on the [001] - [011] boundary, move towards the [011] axis. [8] showed that a load near [001] would correspond to a simple slip along a plane {112}.

Kumagai et al. [7] also reported that with increase in the angle  $\chi$ , the length of Stage I decreases along with increased hardening in Stage II (see right column of Fig. 2.5 ). The strain hardening

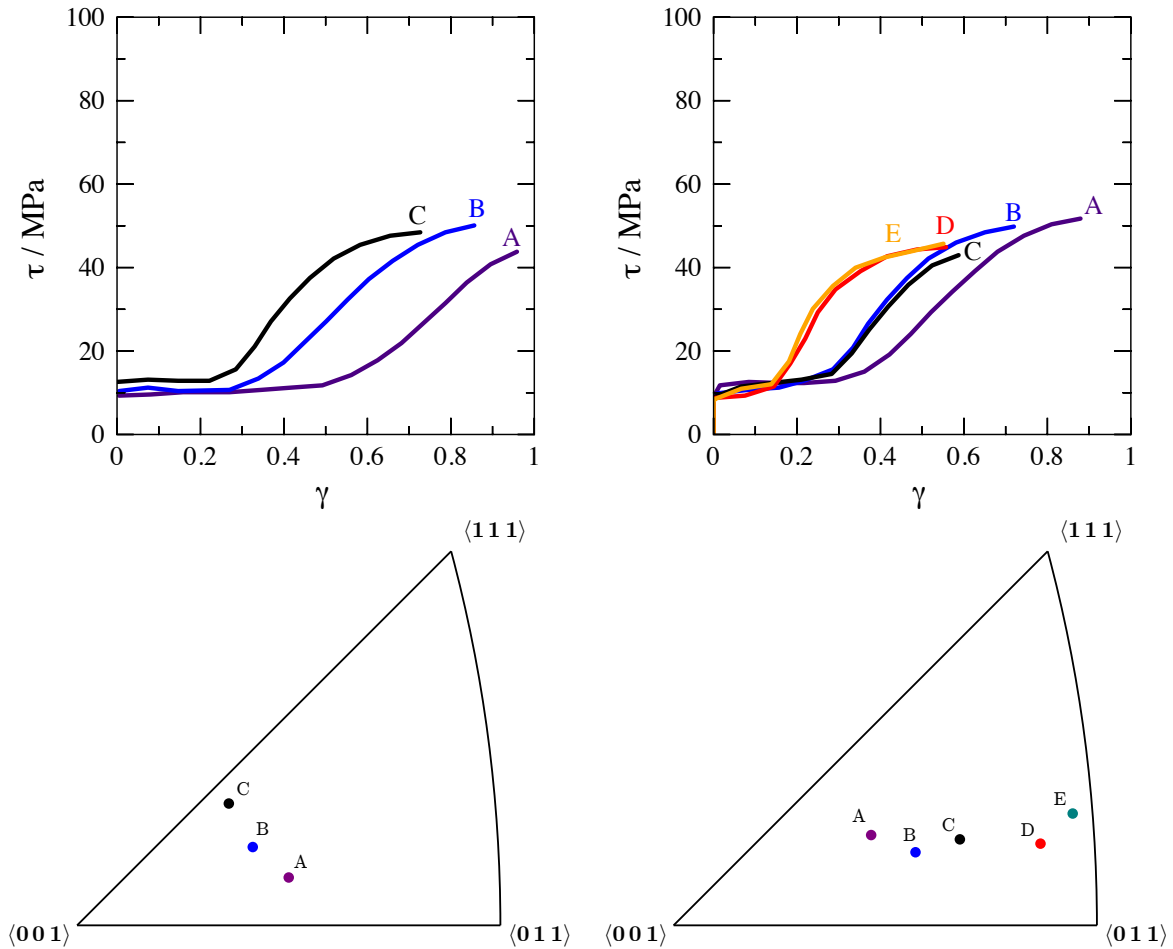


Figure 2.5: Influence of the orientation of the load on the shear stress-strain curves with slip only in  $\{110\}$  system. (Left) effect of angle  $\phi$ , (Right) effect of angle  $\chi$  [7].

rate increases from  $\mu/800$  for orientation A to  $\mu/400$  in curve E. Unfortunately, these results can not be compared with any other study, because the majority of existing works vary  $\chi$  and  $\phi$  simultaneously, preventing any conclusion on the role of each alone.

### 2.3 Non-Schmid effects

BCC metals are known for their direction dependent slip i.e. tension-compression asymmetry. The underlying cause of this behavior can be traced back to the core configuration of screw dislocations in BCC lattice. Due to the polarization of screw dislocation core (see Fig. 2.7), BCC metals

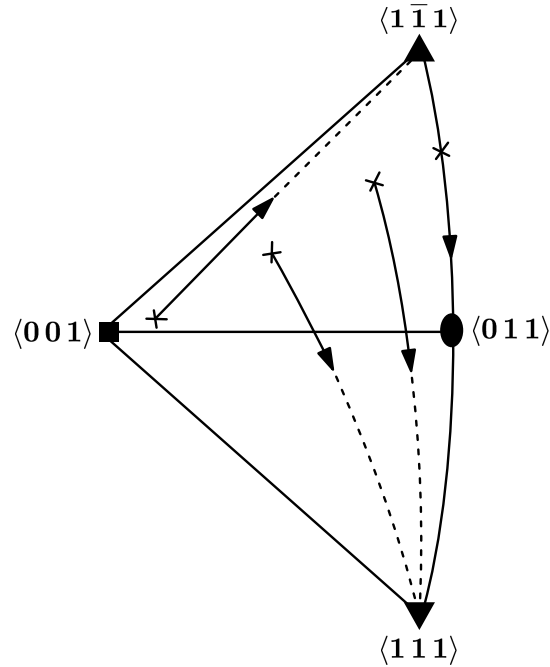


Figure 2.6: Evolution of lattice reorientation with plastic deformation depending on the initial orientation [8, 9, 10].

show a glide direction sensitive slip behavior. It means the slip resistance in one direction is not the same in the opposite direction. This direction sensitive slip behavior is called twinning/anti-twinning asymmetry in BCC metals and arises due to lattice symmetry based reasons. Neuman's principle [51] states that physical properties of the material have a similar kind of symmetry owned by the crystal structure itself. There is no symmetry based reason to believe that positive and negative shear in the  $\{111\}$  slip direction to be equivalent to each other (except on  $\{110\}$  planes for which the  $\{110\}$  dyad axis imposes this symmetry). Observations suggest that for most orientations where the MRSS is  $\{211\}$ , the CRSS for the slip in twinning direction is lower than that of atwinning direction [52, 53, 54]. Hence, it is very likely for the BCC materials to show this anisotropy irrespective of its electronic structure, type of bonding and in the absence of stress. In practical terms, this twinning / anti-twinning effect is observable for pure shear stresses in the direction of the burgers vector. Direct measurement of this phenomenon is difficult, as much larger

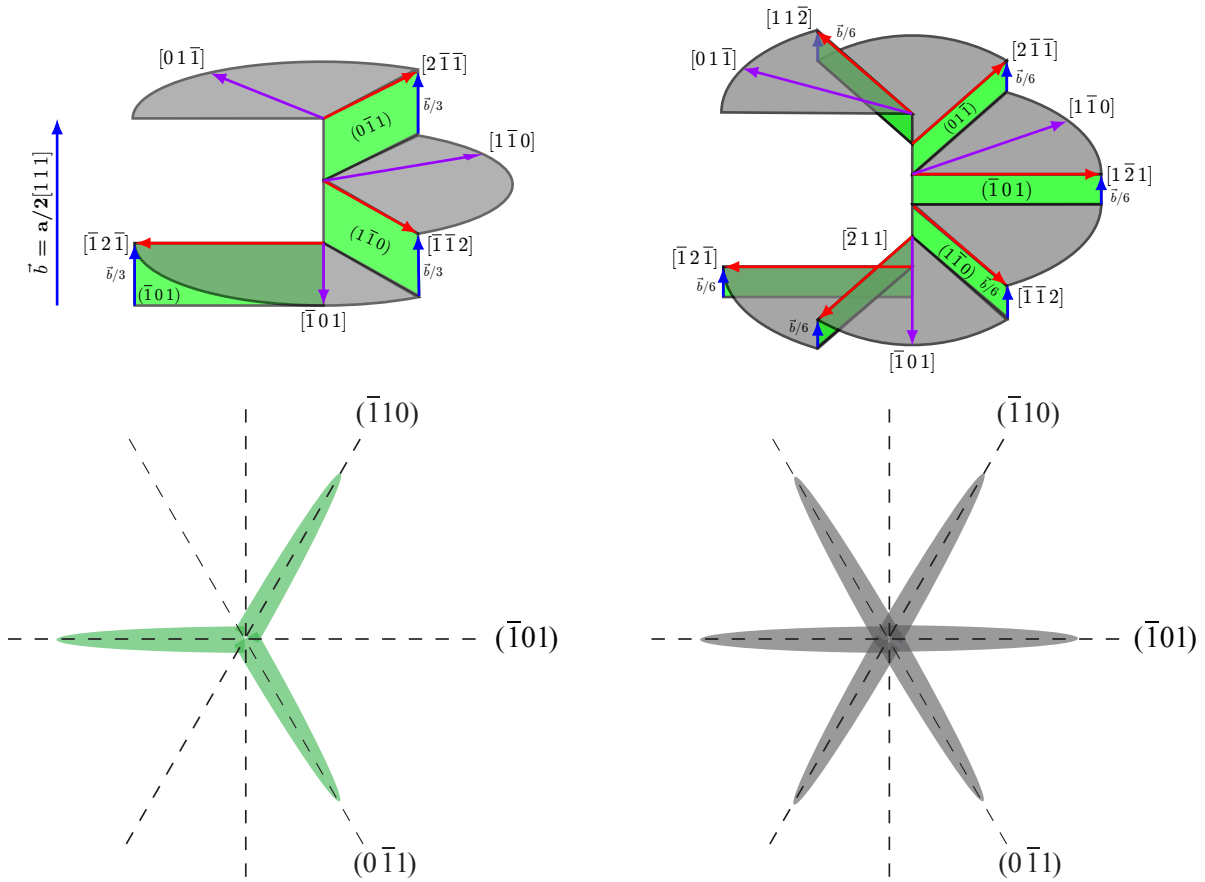


Figure 2.7: Illustration showing core configuration of screw dislocations in a BCC lattice

non-glide stresses often masks it.

Moreover, due to a small fraction of edge components in the partials forming screw the dislocation core, the non-glide components of the applied stress affect the movement of dislocations through the lattice. For these reasons, the Schmid Law breaks down in BCC metals. Macroscopically the violation of Schmid Law is observed in tension-compression asymmetry and movement of screw dislocations even at low stresses. Qin and Bassani [55] suggested non-Schmid effects, to capture the anomalies resulting from the core of screw dislocations. The influence of CRSS by the components of applied stress other than that causing force on displacement was first observed by Escaig [56, 57] while studying cross-slip of partials in FCC materials. The  $1/6\langle 211 \rangle$  partials

dissociated from screw dislocations have edge components. Thus shear stresses in the direction perpendicular to the total Burgers vector widens or narrows the splitting. This is known as *Escaig Effect* in cross-slip and is not only important in FCC [58] but also in  $L1_2$  intermetallic structures. The edge components of Shockley partials of  $a/2\langle 110 \rangle$  dislocations in FCC are fixed, but in the case of fractional dislocations forming the core of  $a/2\langle 111 \rangle$  screw dislocation in BCC, the edge components change with applied stress. As long the vector sum of the edge components in the polarized screw dislocation core is zero, it is possible for the core to have some edge character. Edge components of fractional dislocations are small in the unstressed state. However, non-glide components may induce edge components significantly which change the symmetry and width of the dislocation core. Atomistic investigation suggests that components of applied stress acting to the burgers vector normal to the screw dislocation line heavily influence the width of the dislocation core. The calculated value of Peierls stress decreases by a factor of four [53] if these non-screw components are suppressed and thereby prevent relaxation of the screw dislocation core along directions perpendicular to the dislocation line. The effect of non-glide components of the applied stress is prominent in VIB metals (Cr, Mo, W) while in VB metals (V, Nb, Ta) it is weak or absent. It is to note that most of these atomistic calculations were done on rigid dislocations at zero temperature. At finite temperature, dislocations move by the nucleation and propagation of double kinks, which is discussed in next section.

## **2.4 Kink-pair assisted dislocation motion**

The flow stress of pure BCC metals strongly depends on temperature and strain-rate. In-situ electron microscopy observation of dislocations in BCC metals suggests that edge dislocations have high mobility compared to screws [59, 60, 61]. High mobility of edge dislocations enables

them to exit out of the crystal forming slip steps and leaving screw dislocations behind, which in turn control the strain rate [62, 63]. The low mobility of screws explains the rapid increase of flow stress with decreasing temperature or increasing strain rate [64, 62]. The difference in mobility arises from the fact that for a dislocation to be mobile, it has to overcome the intrinsic periodic lattice resistance (Peierls potential, Fig. 2.8), which is different for different dislocation types [62, 65]. Edge dislocations have a low Peierls energy barrier compared to screws, and thus have higher mobility [64, 62]. At temperatures higher than a critical one (knee temperature  $T_k$ ), slip occurs at stresses lower than that required for overcoming the Peierls barrier [66]. Above  $T_k$ , Screw dislocation of sufficient length can change plane on the simple condition that the effective stress in the deflection plane is greater than that in the primary slip plane. Given the high multiplicity of the possible plane for the deviation, such behavior is quite probable.

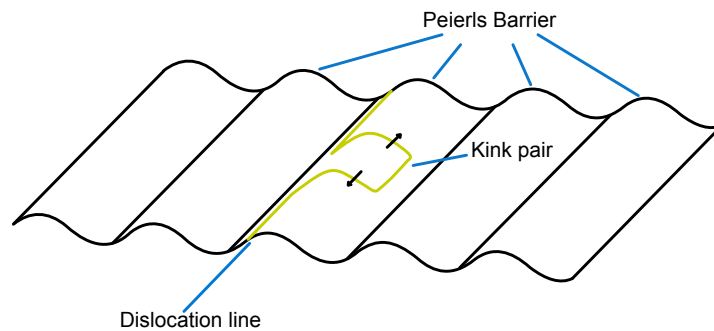


Figure 2.8: Intrinsic lattice resistance (Peierls-Nabarro Barrier) to slip in BCC materials.

Above the knee temperature, screw dislocations lying on low index crystallographic planes can overcome their Peierls barrier [67] by lifting a short segment of the dislocation over the barrier from time to time and letting the segments connecting the two adjacent valleys migrate along the Peierls hills [68]. Shockley gave the name 'kinks' to these segments of dislocations crossing the Peierls barrier. The kinks experience periodic potential energy variation by its position  $z$  along the hills. This position dependent potentials energy is referred to as the *Peierls potential of the*

*second kind or kink potential*. Whether the kink potential is of the same value or smaller than that required for kink formation is determined by the bonding in crystals [62]. For the first case, the kinks are confined to a separation of two neighboring atoms. Such confinement of kinks requires directionality in bonding. In metals due to non-directional bonding, the kink potential is lower than that required for kink formation. As a consequence of this, the kink width is larger compared to interatomic distance. The activation volume of kink migrations is in the order of magnitude of only  $b^3$  [68]. As a result, thermal activation is highly probable. Additionally, the applied resolved shear stress can lower the barrier height, thereby assisting the generation of kink pairs even at low applied stress and on slip systems with a low Schmid factor. Such anomaly of slip behavior as a function of temperature was explained by Seeger and Wasserbach [11] in terms of kink-pair configurations.

## 2.5 Temperature dependence of flow stress

Seeger and Wasserbach [11] showed that the flow stress dependence of temperature in BCC metals could be classified into three temperature regimes and two stress regimes, based on the active mechanism of slip at that particular stress and temperature (Fig. 2.9). The numerical values in Fig. 2.9 correspond to the experiments performed by Hollang et al. [69] on ultra-pure Mo crystal. As mentioned earlier, below the knee temperature  $T_K$  the flow stress of BCC materials is controlled by the mobility of  $a_0/2[1\ 1\ 1]$  screw dislocations given that most of the non-screw components have been removed by pre-deformation. Experiments performed by Hollang et al. [69] on ultra pure Mo demonstrated that the flow stress of BCC single crystals could be given as

$$\sigma = \sigma_M + \sigma^* \quad (2.1)$$

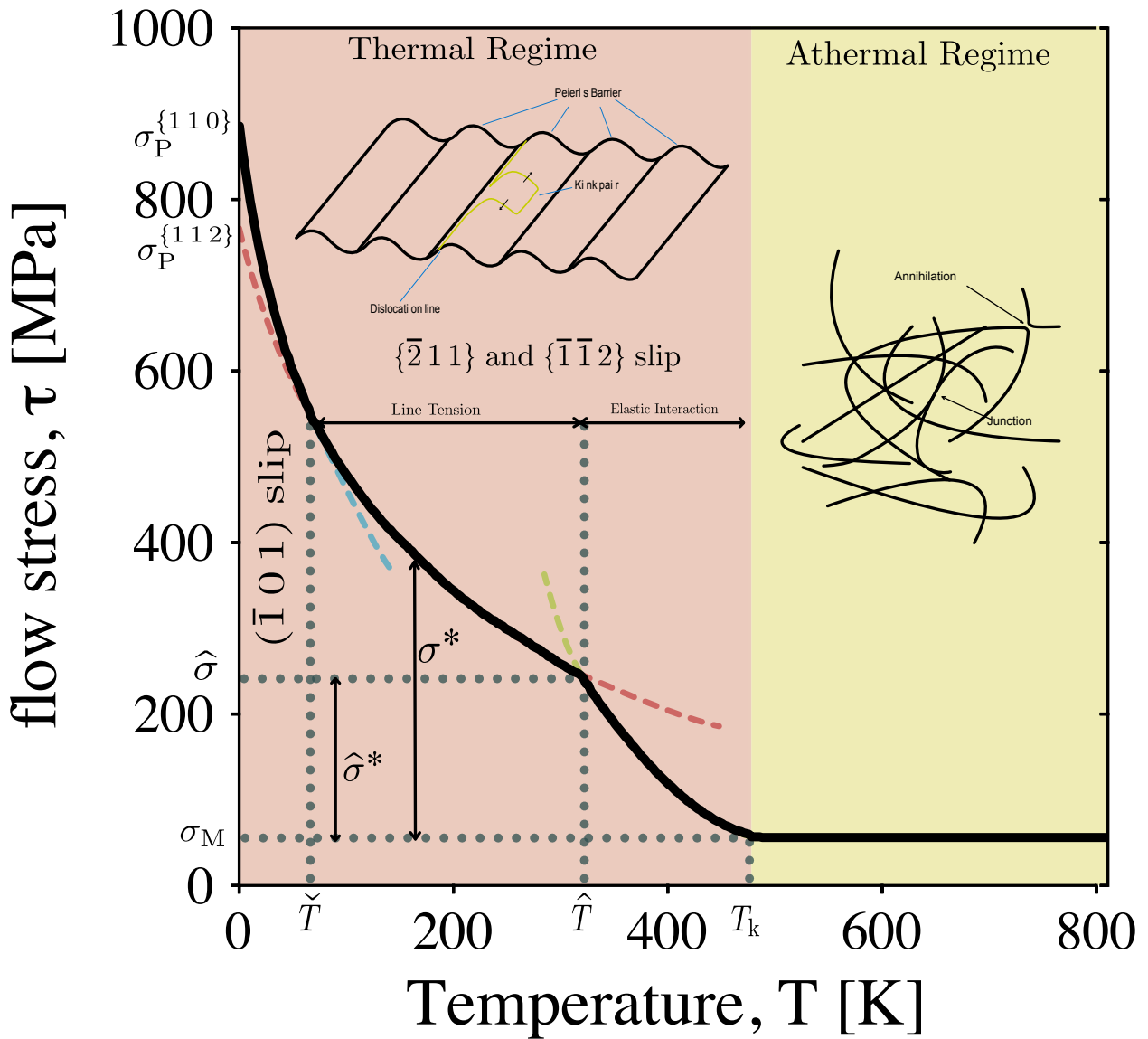


Figure 2.9: Temperature dependence of flow stress, slip mechanisms (schematics) in pure BCC metals (Mo) [11].

where  $\sigma_M$  is the strain-rate-independent flow stress and  $\sigma^*$  is the effective stress required for movement of  $a_0/2[111]$  screw dislocations. Above the knee temperature  $T_K$ , the mobilities of the screw and non-screw components are quite comparable, which is why the flow stress reduces to a strain-rate-independent value  $\sigma_M$ . Below the knee temperature, screw dislocations have low mobility due to a large Peierls barrier compared to the non-screw components. As mentioned

before, this barrier can be overcome by thermally activated, and stress assisted formation of kink pairs. At temperatures  $T$  ( $\check{T} < T < T_k$ ) and effective stress  $\sigma^*$  is less than a critical value  $\hat{\sigma}^*$ , the flow stress is determined by the interaction of the pair of kinks of opposite sign and is known as *elastic-interaction regime*. The formation enthalpy of kink pairs in this regime is given as

$$H_{kp}(\sigma^*) = 2H_k(\sigma^*) - 2\alpha\sigma^{*1/2} \quad (2.2)$$

where  $\alpha^2 = a^3b\gamma_0/2$ .  $2H_k$  denotes the formation energy of the two widely separated kinks of opposite sign,  $a$  the kink height and  $\gamma_0$  the pre-factor proportional to the square of dislocation strength.  $\alpha$  can be determined experimentally, and from that, the kink height  $a$  can be deduced. Seeger and Wasserbach [11] reported that for kink height  $a = \sqrt{2}a_0$ , which corresponds to the distance between Peierls valleys in  $\{112\}$  planes, the experimental data matches the above equation supporting that at higher temperatures  $\{112\}$  slip is favored.

At effective stresses higher than a critical value ( $\sigma^* > \hat{\sigma}^*$ ), the kink - pair formation enthalpy is determined by line tension of dislocations and is known as *line tension regime*. Ackermann et al. [70] showed that approaching the critical effective stress  $\hat{\sigma}^*$  from both top and bottom, using line tension model and elastic interaction model respectively, results in a different activation volume. Hence, the mechanism of kink pair formation changes. This has been verified experimentally by Hollang et al. [69] in ultra pure Mo single crystals. At lower temperatures  $T < \check{T}$ , extrapolation of the above-described line tension model predicts a lower flow stress compared to what has been observed in experiments. Seeger and Wasserbach [11] hypothesized that at  $T < \check{T}$  the core of the screw dislocations assume ground state configuration i.e. the configuration with lowest line energy. The screw dislocations in this configuration exhibit threefold symmetry of the  $\langle 111 \rangle$

crystallographic direction and can glide on any one of the three  $\{110\}$  planes of that zone. On application of finite shear stress, the symmetry of the dislocation core is broken in such a way that the slip plane with highest Schmid factor is chosen as the slip plane for dislocation motion. This phenomenon explains the high flow stress of BCC metals at low temperatures and observance of  $\{110\}$  slip lines for orientations in the middle of standard stereographic triangle.

## 2.6 Overview of deformation in Nb single crystals

Some of the earlier work on the plasticity of pure Niobium (Nb) was carried out by Mitchell et al. [71], Votava [72], Taylor and Christian [73] in the 1960s. They reported that under suitable conditions of purity, orientation, temperature and strain rate, the stress-strain curves in shear show a 3-stage hardening behavior similar to that observed in FCC metals and alloys. Multi-stage hardening in Nb single crystals grown by electron beam zone melting technique were also reported by Duesbery et al. [74]. Mitchell et al. [71] reported that, the work hardening rate in stage II was equal to about  $\mu/600$  for a strain rate of  $4.4 \times 10^{-5} \text{ s}^{-1}$ . This value was later modified by Duesbery et al. [74] to about  $\mu/500$  for the standard conditions used in their work. Annealing of these samples caused the work hardening rate in stage II to increase from  $\mu/700$  to  $\mu/400$  (closer to that of FCC metals  $\mu/300$ ) for an annealing time of more than 12 h. For an orientation lying in the center of the standard stereographic triangle, slip on  $\{110\}$  planes were observed. Straight slip lines were seen on the side faces while those on the top face were shorter and wavy. During the transition from stage I to stage II and stage III, extremely coarse '*hills*' and '*valleys*' were formed on the top face (See Fig. 2.10). Correlation of these '*hills*' with side faces indicated that the '*hills*' were formed in the region of unrestricted primary slip and the '*valleys*' correspond to conjugate slip activity.

In a following article by the same group, a detailed study was done on the tensile axis reorien-



Figure 2.10: Surface topography of deformed single crystal Nb [12]

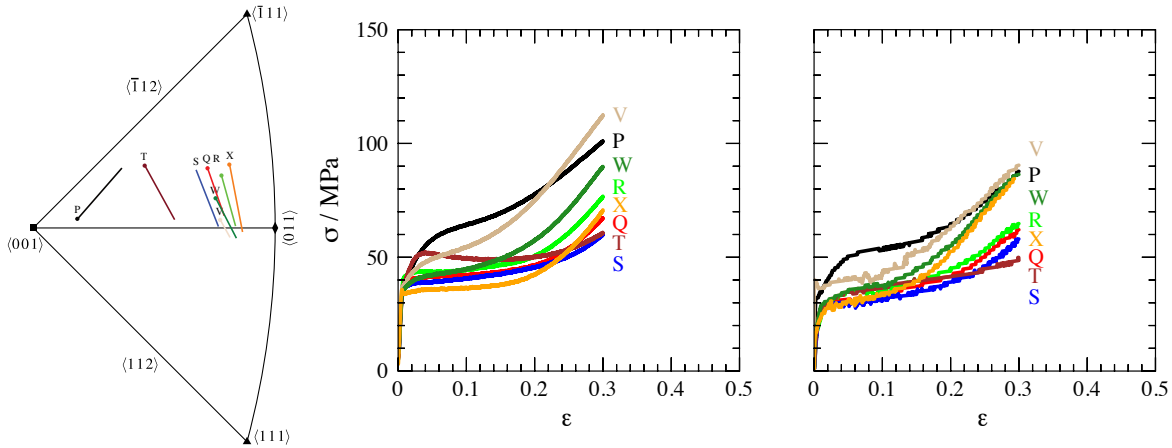


Figure 2.11: In situ uniaxial tensile test results reported by Baars [12]. Left : Inverse pole figure showing rotation of tensile axis as a function of orientation for as-cast samples. Center: axial stress–strain curves for the as-cast samples with same orientations in the left inverse pole figure map. Right : axial stress–strain curves for the annealed samples with the same orientations.

tation in pure Nb single crystals grown by zone melting. The extent and rate of re-orientation were studied as a function of orientation. Most the specimens having orientations in the center right part of the standard stereographic triangle showed trajectories that overshoot the  $[001]$ – $[101]$  boundary. This behavior suggested that most of the orientations started with a single slip system until the tensile axis had moved a small distance beyond the  $[001]$ – $[101]$  boundary when conjugate slip occurs. The maximum distance after crossing the boundary at which conjugate slip takes place was about  $6^\circ$  for orientations in the central upper regions of the triangle. This angular distance was less for the initial orientations belonging to lower right part of the standard stereographic triangle.

Recently, uniaxial in-situ tensile tests performed by Baars [12] on single crystal Nb showed

multi-stage hardening in macroscopic stress-strain curves and texture evolution similar to Duesbery and Foxall [10]. They also observed the formation of 'hills' and 'valleys' on the surface of the sample along with bowed slip lines. The stress-strain behavior of eight single crystals in the as-cast (left) conditions are shown in Fig. 2.11 [12], with the crystal orientation of the tensile axis is indicated by letters in the standard stereographic triangle. The stress-strain curves suggest that different orientations deform very differently, but the trend is that orientations near the  $\langle 111 \rangle$  corner require the most stress, while those in the center of the triangle require the least stress. This general trend persists despite an initial annealing treatment that reduced the dislocation content resulting in 20 % lower flow stresses. The tensile axis re-orientation relative to the crystal frame suggested that slip occurred predominantly on  $\{112\}$  planes for the as-cast condition, but this changed to slip occurring mostly on  $\{110\}$  planes in the pre-annealed samples [75]. The strain hardening rates increased as the tensile orientations move closer to the boundaries of the stereographic triangle, consistent with the activation of slip on additional planes with the same  $\langle 111 \rangle$  directions.

## CHAPTER 3

### MODELING NON-COMPACT GEOMETRIES USING SPECTRAL METHOD

A framework for simulating the deformation behavior of materials involves two important aspects, thermodynamics and kinematics of the deformation process. The former describes why the deformation takes place, while the latter deals with the mechanism by which the material is deformed. In this chapter, an emphasis is given to the kinetic aspect of deformation. As deformation comprises of rotation and distortion, it is necessary to define two separate configurations i.e. an undeformed configuration  $\mathcal{B}_0$  and a deformed configuration  $\mathcal{B}$ . Mechanical fields such deformation and stress can be represented in either configuration. For a material that has been deformed to a finite extent, the deformation is defined by an operation, involving linear mapping of the materials points in the undeformed configuration to the deformed one [76]. This linear mapping is known as the deformation gradient,  $\mathbf{F}$ . The boundary value problem solver (FEM or spectral solver using a fast Fourier transform) determines the boundary condition in the form of an average deformation gradient  $\bar{\mathbf{F}}$  and the material point model provides the corresponding average first Piola-Kirchhoff stress  $\bar{\mathbf{P}}$ . For a finite strain elasto-plastic deformation, the total deformation gradient  $\mathbf{F}$  is decomposed multiplicatively into two parts, the elastic deformation gradient  $\mathbf{F}_e$  and the plastic deformation gradient  $\mathbf{F}_p$  [77]. A schematic illustration of the multiplicatively decomposed deformation process is provided in Fig. 3.1. The multiplicative decomposition introduces an intermediate configuration so that the deformation process occurs in two steps. First, the material deformed plastically to a stress-free state. After that, an elastic deformation is imposed to account for the final shape change as observed in the deformed configuration.

Following this finite strain framework, Roters et al. [78] developed a material point model

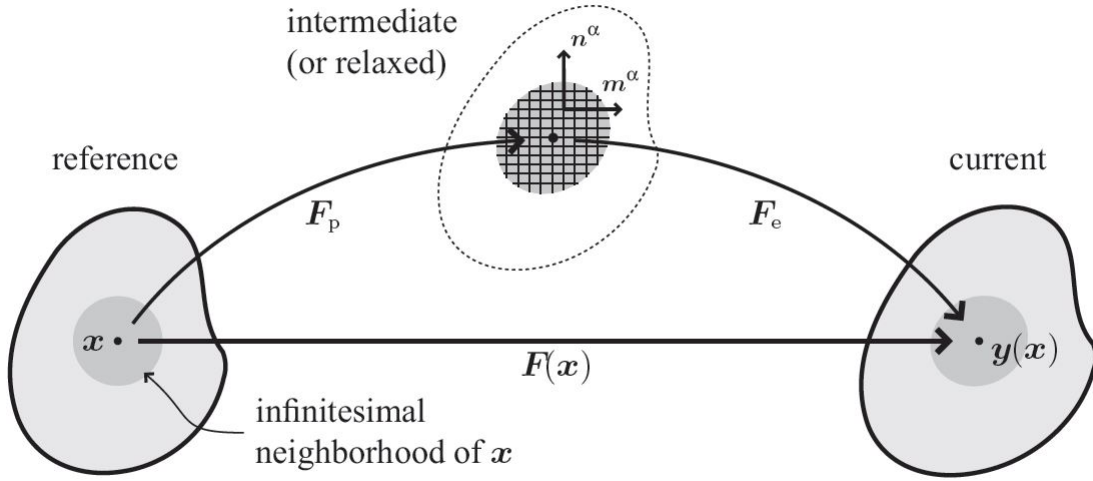


Figure 3.1: Multiplicative decomposition of deformation gradient [13]

DAMASK [79], to capture the mechanical response of a material as a function of its microstructure. In this material point model the elastic deformation gradient  $\mathbf{F}_e$  is related to the second PIOLA–KIRCHHOFF stress tensor (acting on intermediate configuration)  $\mathbf{S} = \mathbb{C} : (\mathbf{F}_e^T \mathbf{F}_e - \mathbf{I}) / 2$ , where  $\mathbb{C}$  is the elastic stiffness tensor. The second PIOLA–KIRCHHOFF stress  $\mathbf{S} = f(\mathbf{F}, \dot{\mathbf{F}}, \eta)$  acts indirectly as the driving force for the plastic velocity gradient  $\mathbf{L}_p$  which is a function of microstructural parameters  $\eta$  in the constitutive model. Depending on the type of material and computation cost involved, a constitutive model can then be formulated as a function of  $\eta$  and  $\mathbf{S}$  to calculate  $\mathbf{L}_p$ . Once  $\mathbf{L}_p$  is calculated the plastic deformation gradient can be estimated as  $\mathbf{F}_p = \mathbf{L}_p^{-1} \dot{\mathbf{F}}_p$ , which is then used to calculate  $\mathbf{F}_e$ . The interdependence of  $\mathbf{L}_p$  and  $\mathbf{S}$  is solved using self-consistency (see Fig. 3.2) at each discretized point within a material static equilibrium is attained. Using the formalism mentioned above, the partial differential equations describing the mechanical loading of a material can be solved for static equilibrium with a boundary value solver such as Finite Element Method (FEM). This has led to the development of a separate area of research in computational mechanics known as Crystal Plasticity Finite Element Method (CPFEM).

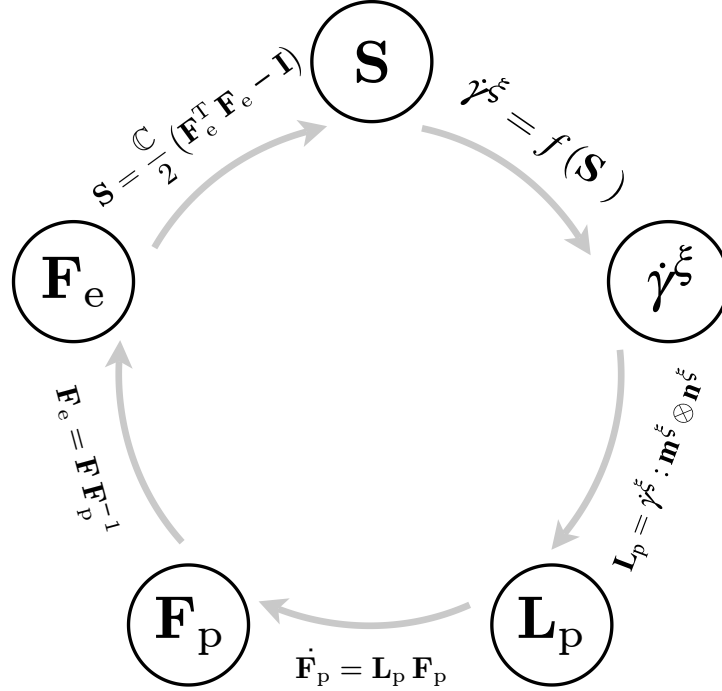


Figure 3.2: Schematic diagram showing calculation of  $\mathbf{S}$  as a function of  $\mathbf{F}$ .

CPFEM has been the vehicle of choice to simulate and understand the mechanical behavior of engineering components with structural dimensions approaching the grain size of the intrinsic microstructure. Examples of such oligocrystalline mechanics can be found in the fields of lead-free solder joints, thin wires, cardiovascular stents, and mesostructured materials such as foams or photonic crystals. The spatial resolutions achievable by CPFEM within reasonable computation times are limited by the substantial numerical effort inherent in the FEM strategy to solve the underlying partial differential equation system.

Spectral methods have emerged as an efficient [80, 81, 82] substitute for CPFEM [83, 84, 85, 86], but only recently were improved sufficiently to overcome their unfavorable convergence when large gradients in mechanical properties are present [87, 88]. This enhanced capability allows the mechanics of porous structures to be solved using spectral methods by replacing the open space (or voids) with soft material [89] in the simulated periodic domain. Examples of such simulations have

been demonstrated in recent works [90, 91, 92, 19]. The methodology used in these works tightly links the behavior of the spectral solution *algorithm* to the specifics of the constitutive behavior of each material point, i.e., making a binary distinction between how to address void and filled points. Furthermore, any nucleation of additional voids not yet present in the initial geometry will require to propagate the information about such a change in local constitutive behavior to the spectral solution algorithm. Such a rigid approach is akin to element elimination in FEM simulations of crack propagation, where a particular constitutive response, i.e. loss of stiffness, is treated through *ad hoc* modification of the geometry instead of properly at the constitutive level, as achieved by, for instance, cohesive zone elements. Following this spirit of keeping any boundary value problem solver as general as possible, i.e., independent of the constitutive material behavior that is simulated, voids should only distinguish themselves through their constitutive model, which, classically, has been vanishingly small elastic stiffness. Here, to describe void regions, a plastically dilatational material is proposed that enables simulations of non-compact geometries such as open or closed-cell foams, or other geometries with free surfaces, by means of established spectral methods without any particular adaptations.

A plastic plate with a circular inclusion under biaxial extension and a dogbone-shaped tensile sample of oligocrystalline aluminum serve to compare this dilatational material model to a low-stiffness isotropically elastic model of all void regions.

### **3.1 Constitutive model for void like regions**

A finite strain framework incorporating two intermediate configurations is adopted, similar to the work of Tjahjanto et al. [93] and following Shanthraj et al. [94]. The total deformation gradient  $\mathbf{F} = \mathbf{F}_e \mathbf{F}_i \mathbf{F}_p$  at each material point is multiplicatively decomposed into isochoric, and

lattice preserving, plastic deformation  $\mathbf{F}_p$ , non-isochoric, but stress-free, dilatation  $\mathbf{F}_i$ , and elastic deformation  $\mathbf{F}_e$ , consecutively mapping the reference configuration into the “lattice” configuration ( $\mathbf{F}_p$ ), then into the “intermediate” configuration ( $\mathbf{F}_i$ ), and finally into the deformed one ( $\mathbf{F}_e$ ). Only the elastic lattice distortion gives rise to stress, which takes the form  $\mathbf{S}_p = \mathbb{C} : \frac{1}{2}\mathbf{F}_i^T (\mathbf{F}_e^T \mathbf{F}_e - \mathbf{I}) \mathbf{F}_i$  in the lattice configuration and  $\mathbf{S}_i = \mathbf{F}_i \mathbf{S}_p \mathbf{F}_i^T / \det \mathbf{F}_i$  in the intermediate one. The stress  $\mathbf{S}_i$  drives the dilatational velocity gradient  $\mathbf{L}_i(\mathbf{S}_i, \boldsymbol{\eta}) = \dot{\mathbf{F}}_i \mathbf{F}_i^{-1}$ , while  $\mathbf{S}_p$  drives the plastic velocity gradient  $\mathbf{L}_p(\mathbf{S}_p, \boldsymbol{\eta}) = \dot{\mathbf{F}}_p \mathbf{F}_p^{-1}$  and the evolution  $\dot{\boldsymbol{\eta}}$  of internal state variables. The total velocity gradient follows as  $\mathbf{L} = \mathbf{L}_e + \mathbf{F}_e \mathbf{L}_i \mathbf{F}_e^{-1} + \mathbf{F}_e \mathbf{F}_i \mathbf{L}_p \mathbf{F}_i^{-1} \mathbf{F}_e^{-1}$ .

To capture the mechanical response of a void, an isotropic plasticity model that combines an isochoric response due to the deviatoric stress with a dilatational response due to the hydrostatic pressure (mean stress) is formulated. The kinetics and internal state parameterization of the model are inspired by the phenomenological crystal plasticity model introduced by Peirce et al. [95] that postulates a power-law relation and an internal deformation resistance, termed  $\tau_0$ .

Thus, in an isotropic setting, the strain rate  $\dot{\epsilon}_p$  connected to isochoric deformation is given as

$$\dot{\epsilon}_p = \dot{\epsilon}_0 \left( \frac{\sqrt{3}J_2}{M\tau_0} \right)^n = \dot{\epsilon}_0 \left( \sqrt{\frac{3}{2}} \frac{\|\mathbf{S}_p'\|}{M\tau_0} \right)^n, \quad (3.1)$$

with  $J_2$  as the second invariant of  $\mathbf{S}_p'$  (deviatoric second PIOLA–KIRCHHOFF stress), stress exponent  $n$ , Taylor factor  $M$ , and  $\|\cdot\|$  the FROBENIUS norm. The associated plastic velocity gradient  $\mathbf{L}_p$ , acting in the lattice configuration, is then formulated as

$$\mathbf{L}_p = \dot{\epsilon}_p \frac{\mathbf{S}_p'}{\|\mathbf{S}_p'\|} = \dot{\epsilon}_0 \left( \sqrt{\frac{3}{2}} \frac{1}{M\tau_0} \right)^n \mathbf{S}_p' \|\mathbf{S}_p'\|^{n-1}. \quad (3.2)$$

To mimic the dilatational response of a void region, a similar constitutive law but for the dilatational expansion rate  $\dot{\epsilon}_i$  and the dilatational velocity gradient  $\mathbf{L}_i$  is formulated in the intermediate

configuration

$$\dot{\epsilon}_i = \dot{\epsilon}_0 \left( \frac{p}{M\tau_0} \right)^n \quad (3.3)$$

$$\mathbf{L}_i = \dot{\epsilon}_i \frac{\mathbf{I}}{\|\mathbf{I}\|} = \dot{\epsilon}_0 \left( \frac{p}{M\tau_0} \right)^n \mathbf{I} \quad (3.4)$$

where  $p$  is the hydrostatic pressure calculated from  $\mathbf{S}_i$ , and  $\mathbf{I}$  is the 2<sup>nd</sup> order identity tensor. The evolution of deformation resistance follows

$$\dot{g} = M\dot{\epsilon}_p h_0 \left| 1 - \frac{\tau_0}{g_\infty} \right|^a \text{sign} \left( 1 - \frac{\tau_0}{g_\infty} \right) \quad (3.5)$$

where  $a$ ,  $\dot{\epsilon}_0$ , and  $h_0$  are adjustable parameters.

The above formulated dilatational plasticity model is closely connected to the VON MISES yield surface shown in Fig. 3.3 in principal stress space. Each point on this cylindrical surface represents a state of stress at which the material deforms plastically. Any position vector  $\mathbf{s}(\sigma_1, \sigma_2, \sigma_3)$  to a point on the yield surface can be represented as a sum of a pressure vector and a deviatoric stress vector, i.e. a component  $\mathbf{p}(\sigma_1 = \sigma_2 = \sigma_3 = \sigma_{\text{sph}})$  along the diagonal and a component  $\mathbf{s}'(\sigma_1 - \sigma_{\text{sph}}, \sigma_2 - \sigma_{\text{sph}}, \sigma_3 - \sigma_{\text{sph}})$  that is perpendicular to the pressure vector. The isochoric deformation rate  $\mathbf{L}_p$  depends, usually, only on the deviatoric stress vector, while the non-isochoric contribution  $\mathbf{L}_i$  is sensitive to (and follows) the pressure vector, i.e., there is a flow stress ‘‘cap’’ that moves along the pressure axis with dilatation.

### 3.1.1 Solution to mechanical boundary value problem

To solve the mechanical boundary value problem of static equilibrium, the finite strain spectral method outlined in [82, 88] and implemented as part of the Dsseldorf Advanced Material Simulation Kit (DAMASK) is used. The constitutive law described above was integrated into the flexible

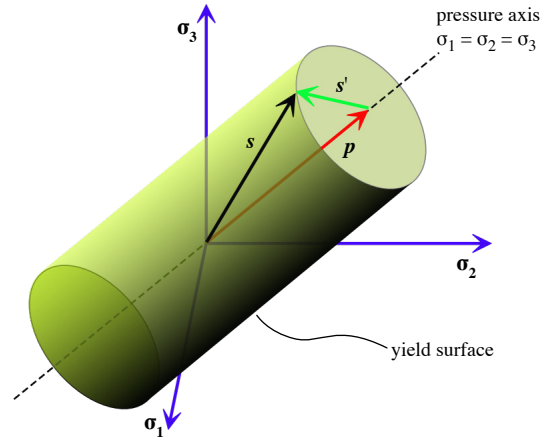


Figure 3.3: Schematics of VON MISES plasticity model in principle stress space. The state of stress at a material point is represented by the vector  $\mathbf{s}$  (black), which can be additively decomposed into the pressure vector  $\mathbf{p}$  (red) and the deviatoric stress vector  $\mathbf{s}'$  (green). The light green surface represents the yield surface of the material point.

material point model offered by DAMASK. Since the solution fields resulting from the spectral method are a superposition of a homogeneous and a fluctuating part, where the mean value of the latter vanishes over the domain, any boundary conditions can only prescribe the average (homogeneous) fields.

### 3.2 Comparison between a dilatational and soft elastic void

Using a plastically isotropic plate with a circular void at its center as an exemplary case, the response of the dilatational material model outlined above is contrasted to an alternative description of the void as a (relatively) soft and purely elastic inclusion. Table 7.1 lists the material parameters used to model the plastic plate as well as the elastic and the dilatational version of the void. The largest elastic stiffness constant  $C_{11}$  of the dilatational and elastic version of the void is scaled down, respectively, one and three orders of magnitude relative to the plate surrounding it, with  $C_{12}$  and  $C_{44}$  calculated such that elastic isotropy and vanishing Poisson ratio for the void is ensured in both versions. The flow stress of the dilatational version of the void is set to be two orders of

Table 3.1: Material parameters; elastic constants  $C_{ij}$ , reference strainrate  $\dot{\epsilon}_0$ , stress exponent  $n$ , initial and saturation flowstress  $\tau_0$  and  $g_\infty$ , hardening parameters  $h_0$  and  $a$ , and Taylor factor  $M = 3$ .

	plate	void		
		elastic	dilatational	
$C_{11}$	100	0.1	10	GPa
$C_{12}$	60	0	0	GPa
$C_{44}$	30	0.05	5	GPa
$\frac{2C_{44}}{C_{11} - C_{12}}$	1.5	1	1	
$\dot{\epsilon}_0$	$10^{-3}$		$10^{-3}$	$s^{-1}$
$n$	20		20	
$\tau_0$	30		0.3	MPa
$g_\infty$	60		0.6	MPa
$a$	2		2	
$h_0$	80		1	MPa

magnitude lower than that of the plate material. The chosen values reflect a compromise between vanishing stress in void regions and the associated computational cost, as detailed in the supplementary material. A  $512 \times 512 \times 1$  regular grid is used to discretize the fully periodic geometry, resulting in about 2100 grid points within the void taking up an area fraction of 0.8 %. The plate is subjected to biaxial tensile elongation along the  $x$  and  $y$  direction (see top row of Fig. 3.4), which is enforced by fixing eight of the components of the average deformation gradient rate and requiring the remaining complementary first PIOLA–KIRCHHOFF stress component  $P_{zz}$  to vanish, i.e.

$$\frac{\langle \dot{\mathbf{F}} \rangle}{10^{-3} s^{-1}} = \begin{bmatrix} 1 & 0 & 0 \\ 0 & 1 & 0 \\ 0 & 0 & * \end{bmatrix} \quad \text{and} \quad \frac{\langle \mathbf{P} \rangle}{\text{Pa}} = \begin{bmatrix} * & * & * \\ * & * & * \\ * & * & 0 \end{bmatrix}, \quad (3.6)$$

where ‘\*’ indicates that stress (or deformation) needs to be iteratively adjusted since deformation (or stress) is prescribed. In the simulations, the conditions of Eq. (3.6) are maintained for 400 increments of 1 s each (such that the final  $\langle F \rangle_{xx} = \langle F \rangle_{yy} = 1.4$ ).

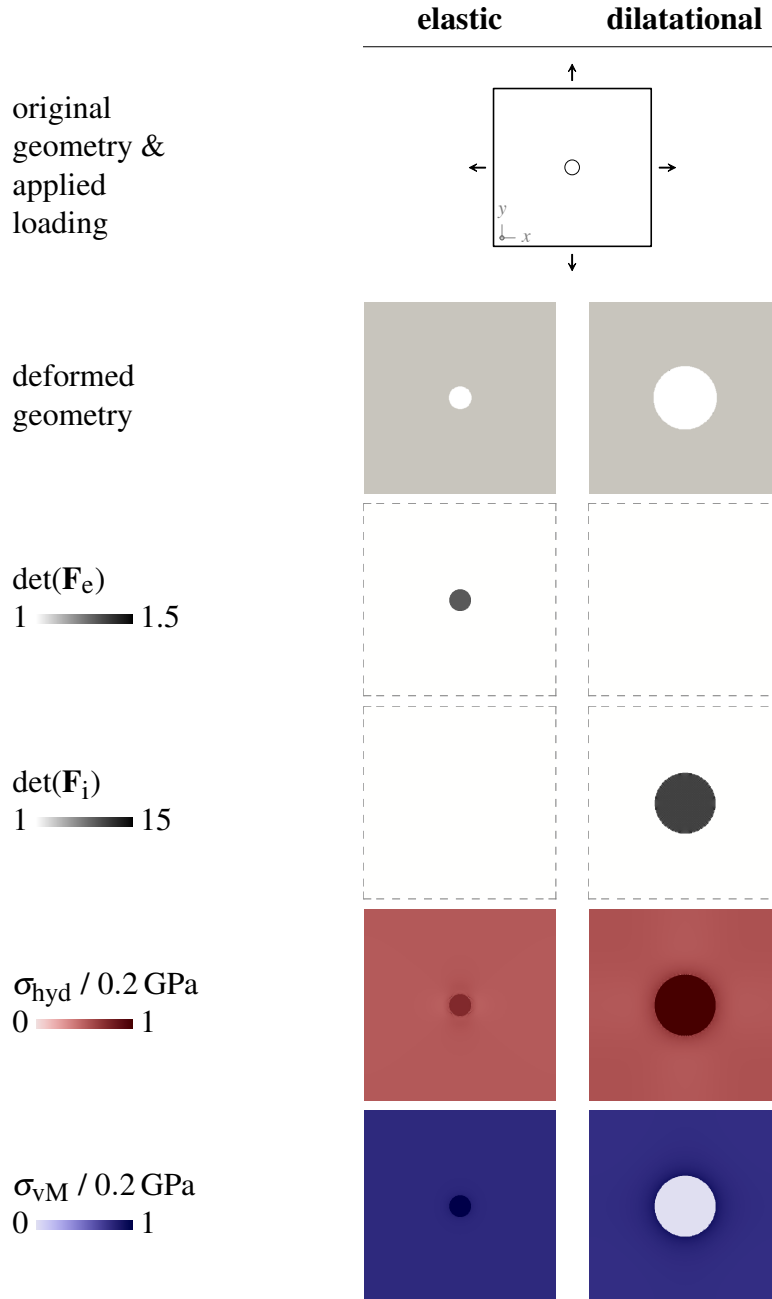


Figure 3.4: Comparison of mechanical field maps of a (fully periodic) two-dimensional plastic plate containing a circular inclusion of area fraction 0.8% and loaded biaxially to an average deformation of  $\langle F_{xx} \rangle = \langle F_{yy} \rangle = 1.4$ . Void volume is described by an isotropic elastic material model (left, “elastic”) or by an isotropic phenomenological plasticity model with dilatational capabilities (right, “dilatational”). The stiffness of the inclusion in the elastic case is set to be  $1000\times$  softer than the plate.

The elastic and dilatational version of the void are contrasted in the first and second row of Fig. 3.4, showing the simulation results at the final simulation step in terms of deformed geometry,

determinant of deformation gradients (i.e. relative change in volume), hydrostatic stress, and VON MISES stress. The two cases reveal markedly different results. For the same final planar geometry (second column), the dilatational void expands to about six times its original diameter, while the purely elastically modeled void only about doubles its diameter. As the volume of the plastic plate is preserved, its final thickness is about 10 % smaller when containing the elastically modeled void. The volumetric expansion of the void is fully carried by  $\det(\mathbf{F}_e)$  for the elastic version, whereas the values of  $\det(\mathbf{F}_e)$  are minute compared to  $\det(\mathbf{F}_i)$  in the dilatational void version (third and fourth column). Since only the hydrostatic *elastic* strain connected to  $\det(\mathbf{F}_e)$ , but not  $\det(\mathbf{F}_i)$ , is giving rise to a hydrostatic stress  $\sigma_{\text{hyd}} = K \varepsilon_{\text{hyd}}$ , with  $K = 0.43 \text{ GPa}$ , the  $\sigma_{\text{hyd}}$  inside the elastic void is much larger than inside the dilatational void and even exceeds the hydrostatic stress experienced by the surrounding plastic plate (column five). To the contrary, the dilatational void does not exhibit any appreciable hydrostatic stress as well as deviatoric stress (column six) since it is *plastically* growing in volume at a flowstress much lower than the flowstress of the plastic plate.

### **3.3 Uniaxial tension of dogbone-shaped sample of oligocrystalline aluminum**

To demonstrate the usefulness of the proposed framework for non-linear geometries, the study performed by Zhao et al. [14] that compares measured to simulated local deformation behavior of a thin oligocrystalline Al dogbone tension sample is reevaluated. In that investigation, the grain structure on the sample front and back face were established through electron backscatter diffraction (EBSD) before and after straining to about 0.1. The local in-plane deformation field was acquired using digital image correlation (DIC) at strain increments of  $5 \cdot 10^{-4}$ . Since most of the about 20 grains in the thin gage section are almost columnar, the modeled geometry was based on a through-thickness extrusion of the grain structure on the front face. Contrary to Zhao

et al. [14], three different boundary conditions are considered in the present study, namely “fully periodic” (periodic copies of hexahedral dogbone gauge section), “quasi-periodic” (periodic along thickness direction, i.e. infinite thickness), and “free surface” conditions. The geometries are discretized by a regular grid of  $273 \times 112$  points and either 10 (fully periodic and quasi-periodic) or 20 points (free surface) across the thickness. A buffer layer of either the dilatational material described above or an isotropic soft-elastic material (see Table 7.1) encases the dogbone geometry for the quasi-periodic and free surface boundary conditions to arrive at a periodic hexahedral cell required by the spectral solver (see left column in Fig. 3.5). The constitutive model used to describe the behavior of the crystalline material is the same as used by Zhao et al. [14]. Uniaxial tension up to a strain of 0.1 along the  $y$  direction, discretized into 1000 equal time increments, is enforced by setting the average deformation gradient rate and complementary first PIOLA–KIRCHHOFF stress to

$$\frac{\langle \dot{\mathbf{F}} \rangle}{10^{-3} \text{ s}^{-1}} = \begin{bmatrix} * & 0 & 0 \\ 0 & 1 & 0 \\ 0 & 0 & * \end{bmatrix} \quad \text{and} \quad \frac{\langle \mathbf{P} \rangle}{\text{Pa}} = \begin{bmatrix} 0 & * & * \\ * & * & * \\ * & * & 0 \end{bmatrix}. \quad (3.7)$$

Figure 3.5 maps the in-plane VON MISES strain and lattice orientation (as inverse pole figure) of the three simulated boundary conditions with dilatational voids, the experiment, and the free surface boundary condition using soft-elastic voids (top to bottom). In the boundary condition sequence using dilatational voids (first to third row), the VON MISES strain is most homogeneous for the fully periodic case, which differs significantly from the measured VON MISES strain. For the quasi-periodic and free surface boundary conditions, the VON MISES strain localizes in grains with softer crystallographic orientations (i.e. higher Schmid factor) enabled by the non-compactness of the simulated geometry. The locations, i.e. the (groups of) grains that deform most, are completely

different between the quasi-periodic and free surface case. When compared to the DIC measured VON MISES strain, only the free surface boundary condition with either the dilatational or soft-elastic voids captures the most relevant strain localization features (third and last row). Despite this agreement, only with dilatational voids does the simulation properly capture the experimentally observed crystal lattice reorientations (last column). The extent and location of strain heterogeneity is not only influenced by microtexture as reported, for instance, by Raabe et al. [96]), but it appears also essential to reflect the correct boundary conditions in a simulation when attempting one-to-one correlations of experimental and simulated data.

In the present study, volumetric dilatation capability is added to an existing isotropic material model to capture the behavior of void-like regions in FOURIER-based spectral solvers. The ability to mimic empty space is essential to address non-compact geometries within the periodicity constraints imposed by such solvers. The model has been applied to simulate the plastic growth of a circular void in a plate under biaxial tension and the known grain-scale deformation behavior of a tensile sample containing a limited number of grains. Both cases show that the proposed formulation provides a more accurate description of void-like behavior compared to assuming a soft-elastic behavior for void volumes.

### **3.4 Selection of parameters for void material description and its associated sensitivity on the simulation results**

To study the influence of material parameter values of the elastic and the dilatational material model for voids, a systematic series of biaxial hole expansion simulations up to  $\langle F_{xx} \rangle = \langle F_{yy} \rangle = 1.2$  was performed. Elastic stiffness ratios between void material and plate spanned the range 1 to  $10^{-3}$ ; strength ratios between the dilatational (void) material and the plate ranged from 1 to  $10^{-2}$ .

The computational cost was quantified by the total number of iterations required to arrive at the solution (on a grid of  $128 \times 128 \times 1$ ). The median value of normal tractions across the plate–void interface collected from all voxels in the immediate neighborhood of that interface (colored ring in Fig. 3.6 top left) serves as quality measure of how well the chosen material description reflects a void.

Figure 3.6 (bottom left) compares the evolution of void quality with biaxial extension among both material descriptions for the two lowest stiffnesses, i.e., ratios of  $10^{-2}$  and  $10^{-3}$ . With increasing hole expansion, the interface traction for the elastic material description asymptotically reaches values slightly in excess of the flow stress of the surrounding plate (estimated by  $Mg$ ), i.e., the void turns from a relatively soft to an effectively hard inclusion. The level of strain at which this transition occurs increases with reduced elastic stiffness of the void material. In contrast, interface tractions of voids described by the dilatational material model are not (except at a plastic strength ratio of  $10^0$ ) increasing up to the plate flow stress, but are limited by their intrinsic flow stress value (as given by the respective plastic strength ratio). Therefore, variations in the elastic stiffness have virtually no influence on the response of voids described by the dilatational material—except for the numerical difficulty to integrate the solution with strain increments that exceed the elasto-plastic transition strain (ratio of dilatational flow stress to stiffness) of the dilatational material (see Fig. 3.6 bottom right). A comparison of the cost to solve the biaxial expansion using either of the two tested void descriptions (Fig. 3.6 top right) shows that there is a marginal penalty (about a factor of two) associated with using the dilatational material model. Nevertheless, this increased effort is generally outweighed by the better quality, unless the void material undergoes only a small amount of strain.

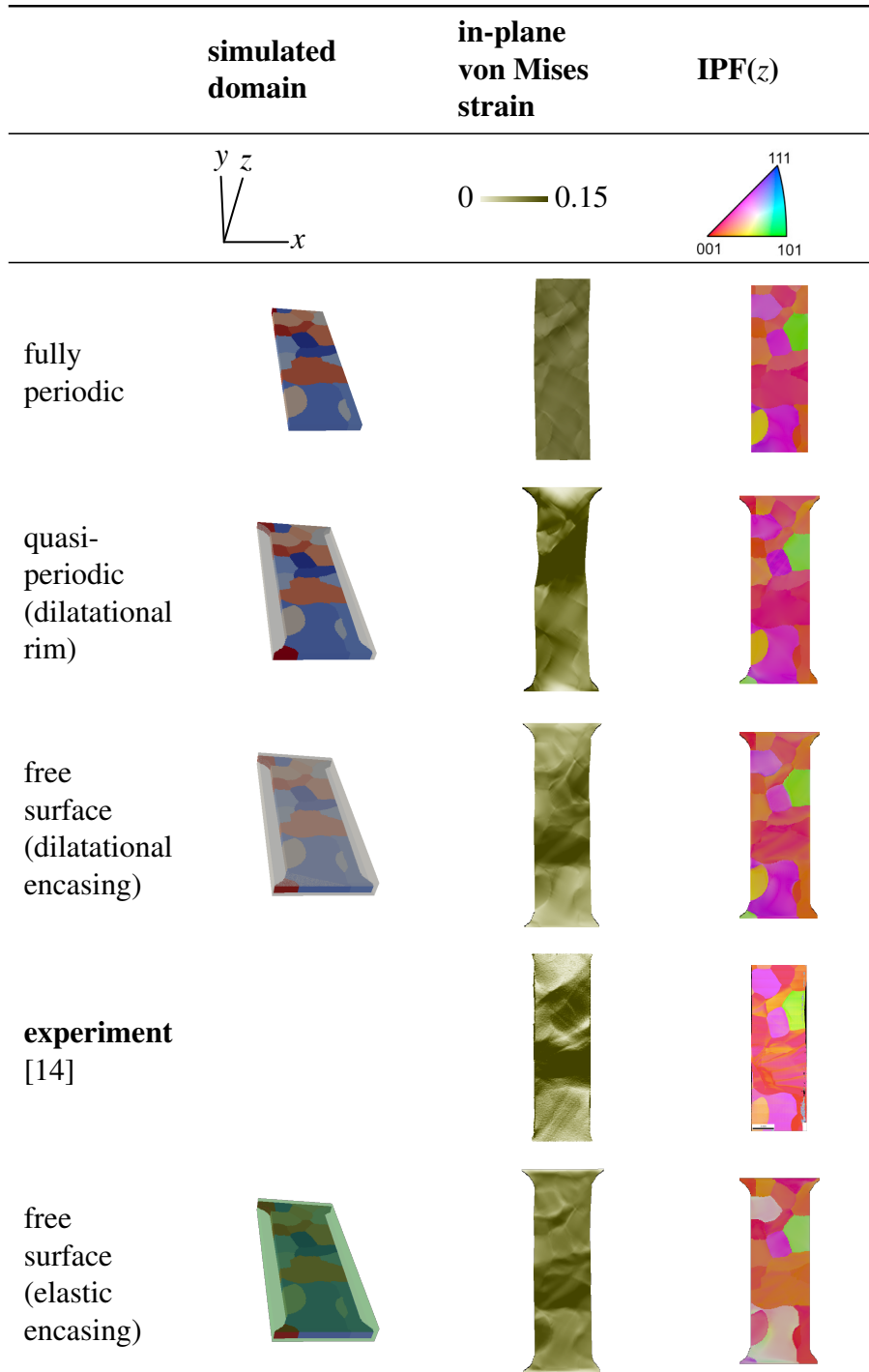


Figure 3.5: Influence of external boundary conditions on in-plane VON MISES strain fields and lattice re-orientation. Simulated geometries with fully periodic gauge section of dogbone (first row), quasi-periodic, i.e. periodic along the thickness direction (second row), and free surfaces normal to  $x$  and  $z$  (third and last row) compared to experimental results measured by DIC and EBSD (fourth row, from [14]). Gray (green) semi-transparent volume in the simulated domain column uses the proposed dilatational (isotropically elastic) material model; regions of constant color reflect individual grains. Inverse pole figure (IPF, last column) coloring of lab direction  $z$  is mapped on the undeformed configuration, except for the measured result (fourth row).

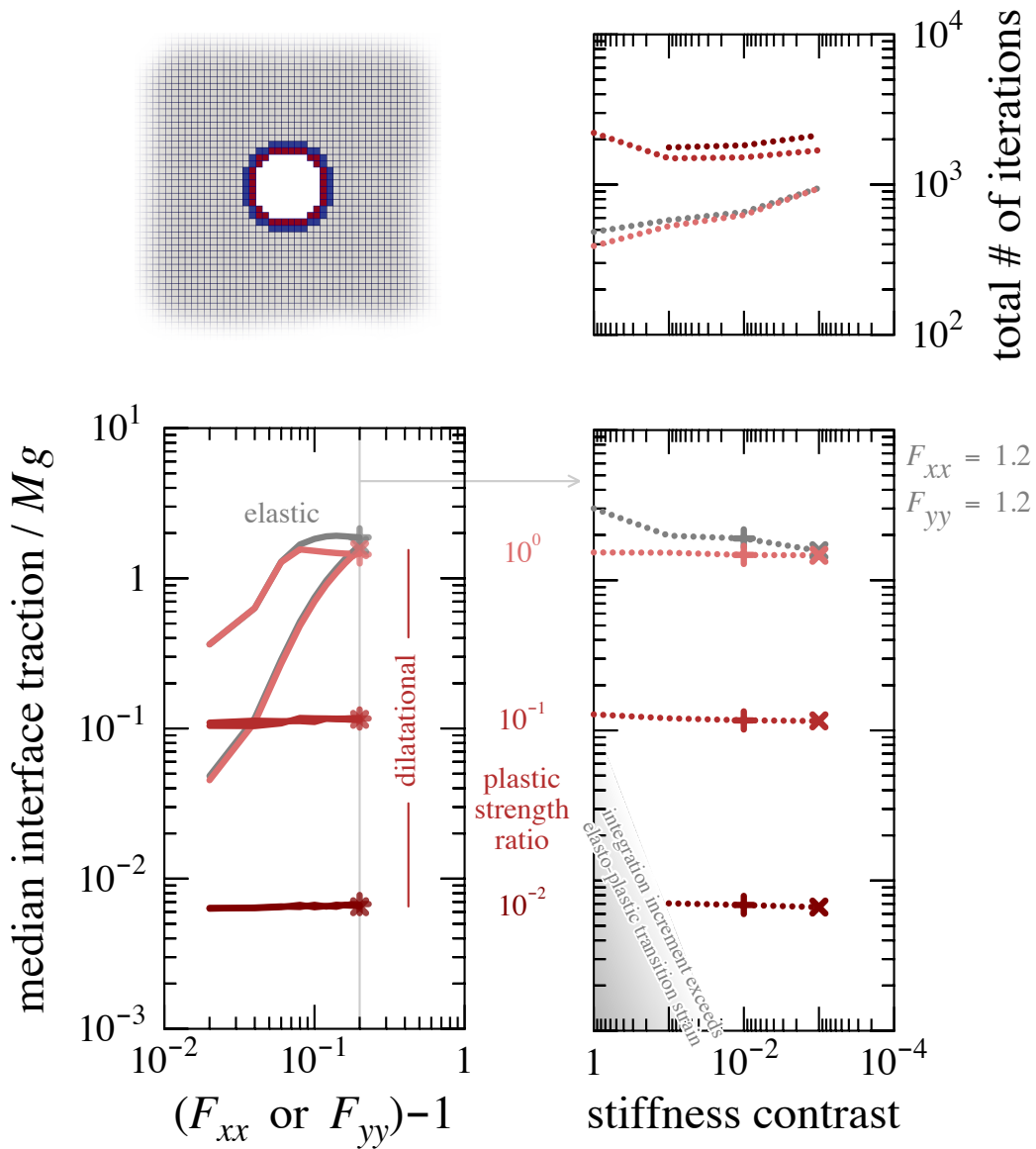


Figure 3.6: Computational cost (top right) and void representation quality (bottom) of the elastic and the dilatational material model for the case of biaxial expansion of a hole in a plastic plate (top left) up to  $\langle F_{xx} \rangle = \langle F_{yy} \rangle = 1.2$ . Strain evolution of median interface traction (lower left, collected from voxels immediately inside and outside of interface, i.e. blue and red ring at top left) indicates the void is reaching the flow stress level ( $\approx Mg$ ) of the surrounding plate in case of the elastic and strongest dilatational material (plastic strength ratio of  $10^0$ ); softer dilatational cases (darker red) saturate much earlier at flow stress levels far below the plate flow stress (plastic strength ratio of  $10^{-1}$  and  $10^{-2}$ ). Median interface tractions collected at  $\langle F_{xx} \rangle = \langle F_{yy} \rangle = 1.2$  (bottom right) confirm marginal influence of elastic stiffness on void representation quality for the dilatational material.

## CHAPTER 4

### CONSTITUTIVE MODELS

A constitutive model relates the response of the material to an external load i.e. it relates a stress (see stress measures [97]) to strain (see strain measures [97]). This relation is necessary to complement the static mechanical equilibrium and the strain compatibility condition. In comparison to general constitutive models, crystal plasticity models take into account the anisotropic stress-strain relation of the crystalline materials. The regular arrangement of atoms in crystalline materials at solid state leads to anisotropic behavior. When stress applied to a crystalline material, the stress is resolved on some particular slip systems  $\xi$  i.e. along a specific crystallographic direction (slip direction) on some particular crystallographic planes (slip plane). The resolved component of the applied stress is known as the Resolved Shear Stress (RSS)  $\tau^\xi$  is expressed as

$$\tau^\xi = \mathbf{S} : \mathbf{m}_0^\xi \otimes \mathbf{n}_0^\xi \quad (4.1)$$

where  $\mathbf{m}^\xi$  and  $\mathbf{n}^\xi$  are the unit vectors of the slip directions and slip plane normal in the current configuration, and  $\mathbf{m}_0^\xi$  and  $\mathbf{n}_0^\xi$  are the slip direction and slip plane normal vector in reference configuration. Plastic deformation is then described by taking into account the total sum of shear of all slip systems. By determining the shear rate  $\dot{\gamma}^\xi$  (function of  $\tau^\xi$ ) with respect to the slip system  $\mathbf{m}_0^\xi \otimes \mathbf{n}_0^\xi$ , the plastic velocity gradient  $\mathbf{L}_p$  as well evolution of plastic deformation can be formulated.

$$\mathbf{L}_p = \dot{\mathbf{F}}_p \mathbf{F}_p^{-1} = \sum_{\xi} \dot{\gamma}^\xi \mathbf{m}_0^\xi \otimes \mathbf{n}_0^\xi \quad (4.2)$$

In the next few sections of this chapter, two most commonly used ideologies to formulate shear-rate  $\dot{\gamma}$  on these slip systems  $\xi$  are discussed.

## 4.1 Phenomenological Model

The phenomenological model is based on the assumption that when the resolved shear stress  $\tau$  exceeds a critical value  $\tau_0$  (Critical Resolved Shear Stress - CRSS), plastic deformation takes place. The resolved shear stress depends on the amount of the applied stress, the angle between the loading direction and the plane normal, and the angle between the loading direction and the slip direction Eq. (4.1). The exact relation is known as Schmid law [40]. In the present study, the constitutive model used, is similar to the phenomenological description of Peirce et al. [1] for cubic lattice symmetry. The internal state is captured through slip resistances  $\tau_0^\xi$  per slip system  $\xi$ , which evolves with shear  $\gamma$  according to a relationship initially proposed by Hutchinson [98] and later improved by Kalidindi et al. [99]

$$\dot{g}^\xi = q^{\xi\beta} h_0 \left| 1 - \frac{\tau_0^\beta}{g_\infty^\beta} \right|^a \text{sign} \left( 1 - \frac{\tau_0^\beta}{g_\infty^\beta} \right) |\dot{\gamma}^\beta|. \quad (4.3)$$

The slip system interactions are controlled by the hardening matrix  $q^{\xi\beta}$ . The shear rate on each system is given by

$$\dot{\gamma}^\xi = \dot{\gamma}_0 \left| \frac{\tau^\xi}{\tau_0^\xi} \right|^n \text{sign } \tau^\xi \quad (4.4)$$

where  $\dot{\gamma}_0$  is a reference shear rate,  $n$  the stress exponent, and  $\tau^\xi = \mathbf{S} : (\mathbf{m}^\xi \otimes \mathbf{n}^\xi)$  the resolved shear stress. Table 7.1 summarizes the list of variables used in the model, with adjustable parameters  $h_0$ ,  $a$ ,  $\tau_0^\xi$ ,  $g_\infty^\xi$ , and  $q^{\xi\beta}$ .

## 4.2 Dislocation density based model

Phenomenological models have been successful in predicting deformation behavior of polycrystalline materials [100, 99, 101, 102]. However, as shown in an earlier section, the phenomenological models fails to capture the intrinsic anisotropic deformation of BCC materials at the single

Table 4.1: Material variables for Peirce et al. [1] model; elastic constants  $C_{ij}$ , reference shear rate  $\dot{\gamma}_0$ , stress exponent  $n$ , initial and saturation slip resistance  $\tau_0^\xi$  and  $g_\infty^\xi$ , hardening parameters  $h_0, q^{\xi\beta}$ , and  $a$ .

Elastic			Plastic			Strain hardening				
$C_{11}$	$C_{12}$	$C_{44}$	$\dot{\gamma}_0$	$n$	$\tau_0^\xi$	$g_\infty^\xi$	$a$	$h_0$	$q^{\xi\xi}$	$q^{\xi\beta}$
GPa	GPa	GPa	$s^{-1}$		MPa	MPa		MPa		

crystal level. Therefore, to better understand deformation in complex slip conditions, a crystal plasticity model considering statistical properties of an ensemble of dislocations and their mutual interactions is needed. These models are based on the idea that, for a dislocation to move it has to overcome the energy barriers. As discussed earlier, there are two kinds of barrier: a short range one which can be overcome by thermal activation such as Peierls potentials, solid solution impurity atoms, and long-range barriers like forest dislocations, grain boundaries and internal stresses of the athermal type. The total resistance to slip is then defined as the sum of thermal ( $s_t^\xi$ ) and athermal resistance ( $s_a^\xi$ ) to dislocation motion.

$$s^\xi = s_t^\xi + s_a^\xi \quad (4.5)$$

The average velocity of dislocations is given by an Arrhenius type relationship,

$$v_{avg}^\xi = v_0^\xi \exp \left\{ \frac{-\Delta G}{k_B T} \right\} \quad (4.6)$$

Where  $\Delta G$  is the activation energy,  $v_0$  the reference velocity,  $k_B$  the Boltzman constant and  $T$  the temperature. This temperature dependence of the average velocity of dislocation can be substituted back into Orowan equation ( $\dot{\gamma}^\xi = \rho \xi b v_{avg}^\xi$ ) to have a shear rate that is dependent on temperature and applied stress.

$$\dot{\gamma}^\xi = \begin{cases} 0 & \text{if } \tau_{eff}^\xi \leq 0 \\ \dot{\gamma}_0^\xi \exp \left\{ \frac{-\Delta G}{k_B T} \right\} & \text{if } \tau_{eff}^\xi > 0 \end{cases} \quad (4.7)$$

where  $\dot{\gamma}_0^\xi = \rho^\xi b v_0^\xi$  is the reference strain rate and  $\tau_{\text{eff}}^\xi = \left| \tau^\xi \right| - s_a^\xi$  the effective resolved shear stress acting on slip system  $\xi$ . The activation energy barrier can be calculated using an approach suggested by Kocks [103].

$$\Delta G = \Delta G_0 \left\{ 1 - \left( \frac{\tau_{\text{eff}}^\xi}{s_t^\xi} \right)^p \right\}^q \quad (4.8)$$

Where  $\Delta G_0$  is the activation energy for obstacle free dislocation motion. The parameters  $p$  and  $q$  can be fitted to get an accurate description of the activation profile. Combining these ideas one can arrive at an expression of shear rate that is temperature dependent.

$$\dot{\gamma}^\xi = \rho^\xi b v_0^\xi \exp \left[ \frac{-\Delta G_0}{k_B T} \left\{ 1 - \left( \frac{\tau_{\text{eff}}^\xi}{s_t^\xi} \right)^p \right\}^q \right] \quad (4.9)$$

The primary state variables characterizing the microstructural state are the dislocation densities  $\rho^\xi$  on each slip system. Plastic flow at lower length scales, occurs as a succession of dislocation avalanches with each avalanche triggered by the dislocation interactions [16]. When two dislocation segments moving in non-coplanar slip planes intersect each other, a junction is formed, if the Frank criterion is satisfied. The two segments are then zipped together to form a sessile segment. These sessile segments are destroyed when the work done by the local resolved stress  $\tau$  on one arm of the parent dislocations, of length  $l_u$ , is sufficient to unzip the junction. The amount of work done in formation of the junction per unit length is  $W_j = \tau b l_u$ , where  $b$  is the Burgers vectors of the parent dislocations of length  $l_u$ . The change in elastic energy due to the newly formed dislocation segment can also be written as  $\Delta E = \alpha \mu b^2$ , where  $\alpha$  describes the strength of the junction formed. Comparing work done with the change in elastic energy,  $\alpha$  can be expressed as,

$$\alpha = \frac{\tau l_u}{\mu b} \quad (4.10)$$

Taylor [104] first proposed a relation between athermal resistance to deformation  $s_a$  and the total dislocation density  $\rho$  utilizing the dislocation interaction  $\alpha$ .

$$s_a = \mu b \alpha \sqrt{\rho} \quad (4.11)$$

where  $\mu$  is the isotropic shear modulus and  $b$  is the Burgers vector. This expression Eq. (4.11) was latter vectorized by Franciosi et al. [105].

$$s_a^\xi = \mu b \sqrt{\sum_{\beta} A_{\xi\beta} \rho \beta} \quad (4.12)$$

where the interaction coefficients  $A_{\xi\beta}$  are dimensionless components of the so-called interaction matrix (Table 4.2). They measure the strength of the interaction between the primary slip system  $\xi$  and other slip systems  $\beta$ . The strengthening coefficients  $\alpha_{\xi\beta} = \sqrt{A_{\xi\beta}}$  are often used to make comparisons between experiment and theoretical estimates [106]. These interactions coefficient are calculated using DDD simulations. Queyreau et al. [2] reported the interaction coefficients for BCC  $\alpha$ -Fe, and since then it has been used by several authors to model dislocation behavior in other BCC materials [107, 108]. There are 6 distinct kinds of interaction possible for dislocations in BCC lattice as shown with their corresponding values for  $\alpha$ -Fe in Table 4.3. The values reported in Table 4.3 were calculated at a reference dislocation forest density ( $\rho_{ref}$ ) of  $2 \times 10^{13} \text{ m}^{-2}$ . The nature of these dislocation interactions are inherently elastic, as it removes a significant amount of line energy from the crystal. This behavior has been well documented in experimental works of Basinski and Basinski [109] in FCC metals. Basinski and Basinski [109] also showed that the unzipping action of a junction is influenced by line tension and curvature of the dislocation line, which in turn depends on the forest density. Hence, a logarithmic factor Eq. (4.13) needs to be

Table 4.2: Dislocation interaction matrix in BCC lattice.

	{110}										{112}													
{110}	1	2	6	6	5	4	4	3	4	3	5	4	6	6	4	3	3	4	6	6	4	3	6	6
	2	1	6	6	4	3	5	4	5	4	4	3	6	6	3	4	4	3	6	6	3	4	6	6
	6	6	1	2	4	5	3	4	4	5	3	4	4	3	6	6	6	6	3	4	6	6	4	3
	6	6	2	1	3	4	4	5	3	4	4	5	3	4	6	6	6	6	4	3	6	6	3	4
	5	4	4	3	1	2	6	6	3	4	5	4	3	6	4	6	6	4	6	3	4	6	3	6
	4	3	5	4	2	1	6	6	4	5	4	3	4	6	3	6	6	3	6	4	3	6	4	6
	4	5	3	4	6	6	1	2	5	4	3	4	6	3	6	4	4	6	3	6	6	4	6	3
	3	4	4	5	6	6	2	1	4	3	4	5	6	4	6	3	3	6	4	6	6	3	6	4
	4	5	4	3	3	4	5	4	1	2	6	6	3	6	6	4	4	6	6	3	6	4	3	6
	3	4	5	4	4	5	4	3	2	1	6	6	4	6	6	3	3	6	6	4	6	3	4	6
5	4	3	4	5	4	3	4	6	6	1	2	6	3	4	6	6	4	3	6	4	6	6	3	
4	3	4	5	4	3	4	5	6	6	2	1	6	4	3	6	6	3	4	6	3	6	6	4	
{112}	6	6	4	3	3	4	6	6	3	4	6	6	1	5	6	6	5	6	6	3	5	6	3	6
	6	6	3	4	6	6	3	4	6	6	3	4	5	1	6	6	6	5	3	6	6	5	6	3
	4	3	6	6	4	3	6	6	6	6	4	3	6	6	1	5	6	3	5	6	3	6	5	6
	3	4	6	6	6	6	4	3	4	3	6	6	6	6	5	1	3	6	6	5	6	3	6	5
	3	4	6	6	6	6	4	3	4	3	6	6	5	6	6	3	1	6	5	6	5	3	6	6
	4	3	6	6	4	3	6	6	6	6	4	3	6	5	3	6	6	1	6	5	3	5	6	6
	6	6	3	4	6	6	3	4	6	6	3	4	6	3	5	6	5	6	1	6	6	6	5	3
	6	6	4	3	3	4	6	6	3	4	6	6	3	6	6	5	6	5	6	1	6	6	3	5
	4	3	6	6	4	3	6	6	6	6	4	3	5	6	3	6	5	3	6	6	1	6	6	5
	3	4	6	6	6	6	4	3	4	3	6	6	6	5	6	3	3	5	6	6	6	1	5	6
6	6	4	3	3	4	6	6	3	4	6	6	3	6	5	6	6	6	5	3	6	5	1	6	
6	6	3	4	6	6	3	4	6	6	3	4	6	3	6	5	6	6	3	5	5	6	6	1	

Table 4.3: Types of possible interaction in BCC lattice [2]

ID	Interaction Type	Interaction Coefficient
1	self	$0.0068 \pm 0.001$
2	coplanar	$0.0068 \pm 0.001$
3	collinear	$0.5300 \pm 0.040$
4	mixed asymmetric	$0.0390 \pm 0.005$
5	mixed symmetric	$0.0630 \pm 0.006$
6	edge junction	$0.0360 \pm 0.006$

considered for these effects.

$$A_{\xi\beta} = A_{\xi\beta}^{\text{ref}} \frac{\ln\left(\frac{1}{b}\sqrt{A_{\xi\beta}\rho_f^\beta}\right)}{\ln\left(\frac{1}{b}\sqrt{A_{\xi\beta}\rho_{\text{ref}}^\beta}\right)} \quad (4.13)$$

$\rho_f^\xi$  is the existing dislocation density and  $\rho_{\text{ref}}^\xi$  is the reference dislocation density at which the interaction coefficients are calculated by DDD.

#### 4.2.1 Influence of elastic anisotropy on dislocation interaction strengths

In pure BCC single crystals above the knee temperature,  $T_k$  i.e athermal regime, the reactions between dislocation segments offers to most of the resistance to dislocation motion. Therefore, the interaction coefficients defining the junctions strengths are critical in reproducing the macroscopic deformation behavior. Initially these interaction coefficients were considered to be dependent only on the crystal structure, until recently it was shown by Madec and Kubin [3] that this is not necessarily true. Two effects namely, “Poisson ratio” and “asymmetric junction configurations” influence the strength of interactions between dislocation segments. These two effects are more prominent in BCC metals than in FCC metals. In their study, strengths of dislocation interaction among  $\langle 111 \rangle \{110\}$  and  $\langle 111 \rangle \{112\}$  slip systems were determined using dislocation dynamics simulations at high homologous temperatures for five BCC transition metals. They predicted that the use of accurate material-dependent coefficients would notably improve the predictive ability of current models for strain hardening.

Madec and Kubin [3] made use of Scattergood and Bacon’s shear moduli and Poisson’s ratios [110] to approximate the behavior of curved dislocations in an anisotropic medium. The results concluded that in a BCC metal (compared to FCC), the strength of junctions is mainly governed by the orientation dependence (angle between the interacting slip planes) of the line energies. This angle affects the magnitude of short-range interactions between dislocation segments influencing the limit between attraction and repulsion for non-coplanar dislocation reactions. The value of the Poisson ratio affects all the strengthening coefficients to various extents ranging from small

Table 4.4: Modified dislocation interaction matrix in BCC lattice taking into account asymmetric junction configurations [3].

		{110}											{112}											
{110}	1	2	2	3	5	5	6	4	7	6	7	4	8	9	9	11	13	13	14	17	18	17	14	18
	2	1	2	4	6	7	5	3	5	7	6	4	9	9	8	17	14	18	13	11	13	17	18	14
	2	2	1	4	7	6	7	4	6	5	5	3	9	8	9	17	18	14	18	17	14	11	13	13
	3	5	5	1	2	2	6	7	4	6	4	7	11	13	13	8	9	9	17	14	18	14	17	18
	4	6	7	2	1	2	7	6	4	5	3	5	17	14	18	9	9	8	17	18	14	13	11	13
	4	7	6	2	2	1	5	5	3	7	4	6	17	18	14	9	8	9	11	13	13	18	17	14
	6	4	7	6	7	4	1	2	2	3	5	5	18	14	17	18	17	14	9	9	8	13	13	11
	5	3	5	7	6	4	2	1	2	4	6	7	13	13	11	14	17	18	9	8	9	14	18	17
	7	4	6	5	5	3	2	2	1	4	7	6	14	18	17	13	11	13	8	9	9	18	14	17
	6	7	4	6	4	7	3	5	5	1	2	2	18	17	14	18	14	17	13	13	11	9	9	8
	7	6	4	5	3	5	4	6	7	2	1	2	14	17	18	13	13	11	14	18	17	9	8	9
5	5	3	7	4	6	4	7	6	2	2	1	13	11	13	14	18	17	18	14	17	8	9	9	
{112}	8	9	9	10	16	16	19	12	15	19	15	12	1	2	2	20	21	21	23	22	24	22	23	24
	9	9	8	12	15	19	15	12	19	16	16	10	2	1	2	22	24	23	24	22	23	20	21	21
	9	8	9	12	19	15	16	10	16	15	19	12	2	2	1	22	23	24	21	20	21	22	24	23
	10	16	16	8	9	9	19	15	12	19	12	15	20	21	21	1	2	2	22	23	24	23	22	24
	12	15	19	9	9	8	16	16	10	15	12	19	22	24	23	2	1	2	20	21	21	24	22	23
	12	19	15	9	8	9	15	19	12	16	10	16	22	23	24	2	2	1	22	24	23	21	20	21
	15	12	19	16	16	10	9	9	8	12	15	19	23	24	22	21	20	21	1	2	2	24	23	22
	16	10	16	15	19	12	9	8	9	12	19	15	21	21	20	23	22	24	2	1	2	23	24	22
	19	12	15	19	15	12	8	9	9	10	16	16	24	23	22	24	22	23	2	2	1	21	21	20
	16	16	10	15	12	19	12	15	19	9	9	8	21	20	21	23	24	22	24	23	22	1	2	2
	15	19	12	16	10	16	12	19	15	9	8	9	23	22	24	21	21	20	23	24	22	2	1	2
19	15	12	19	12	15	10	16	16	8	9	9	24	22	23	24	23	22	21	21	20	2	2	1	

to substantial. Increasing Poisson's ratio strengthens the collinear interactions, while decreasing it, leads to less stable junctions due to higher line energies. Taking into consideration of all these influences, [3] has proposed a modified interaction matrix (see Table 4.4). The corresponding values of interaction strengths for Nb calculated by them with Scattergood and Bacon's anisotropic approximation are presented in Table 4.5.

Table 4.5: Types of possible interaction in BCC lattice with asymmetric junction configurations [3].

	ID	Interaction Type	Interaction Coefficient (G - glissile junctions)
$\{110\}$ - $\{110\}$ interactions	1	self	0.20
	2	collinear $60^\circ$	0.82
	3	coplanar	0.20
	4	$J_1$ $0^\circ$ (G)	0.24
	5	$J_1$ $70.53^\circ$ (G)	0.20
	6	$J_2$	0.31
	7	$J_3$	0.28
$\{110\}$ - $\{112\}$ or $\{112\}$ - $\{110\}$ interactions	8	Collinear $90^\circ$	0.90
	9	Collinear $30^\circ$	0.64
	10	$J_4$ $0^\circ$ (G)	0.25
	11	$J_4$ $70.53^\circ$ (G)	0.20
	12	$J_5$ $0^\circ$ (G)	0.20
	13	$J_5$ $70.53^\circ$ (G)	0.17
	14	$J_6$ $29.50^\circ$	0.20
	15	$J_6$ $58.52^\circ$	0.20
	16	$J_7$ $58.52^\circ$	0.27
	17	$J_7$ $79.98^\circ$	0.25
	18	$J_8$ $35.26^\circ$	0.26
	19	$J_8$ $90^\circ$	0.27
$\{112\}$ - $\{112\}$ interactions	20	$J_9$	0.28
	21	$J_{10}$ $28.56^\circ$	0.23
	22	$J_{10}$ $72.98^\circ$	0.23
	23	$J_{11}$	0.26
	24	$J_{12}$	0.19

#### 4.2.2 Dislocation storage and recovery framework

The dislocation storage/recovery framework is a rather simple concept which defines the evolution of the total dislocation density in a uniform microstructure with time or strain, under the influence of mechanisms such as dislocation strengthening, storage, and dynamic recovery. Such a formulation is particularly suitable for multiscale modeling because of its kinematic character and its potential to reproduce stress/strain curves with all deformation stages in a continuous fashion.

Teodosiu et al. [111], Kocks and Mecking [112] proposed a generalized version of storage and recovery framework that treats uniform dislocation densities on each slip system. This framework assumes that the local microstructure mostly consists of dislocations immobilized (stored) by interaction with other dislocations. For each slip system  $\xi$ , the stored density  $\rho$  is much larger than the instantaneous mobile density and is therefore assimilated to the total density. It is also assumed that there are always enough mobile dislocations to sustain the imposed strain rate and compensate for the losses by storage and annihilation. Thus, the continuous storage of mobile dislocations is accounted for, and the mobile density does not explicitly appear in the model. The most important part of the framework is defining the Mean Free Path (MFP) of dislocations. A segment of average length  $l$ , moving by an incremental step  $\delta l$ , in a volume  $V$  produces a shear strain  $\delta\gamma = \frac{b\delta l}{V}$ . If it is immobilized, the stored density is increased by  $\delta\rho = \frac{l}{V}$ . The mean free path  $\Lambda$  is the average length traveled by mobile dislocation segments during a strain increment. The storage probability is then defined as  $\delta l/\Lambda$  and the storage rate is  $\frac{\delta l/\Lambda}{\delta\rho/\delta\gamma} = \frac{b}{\Lambda}$ . As the length of the dislocation segment changes when it moves, the mean free path is a virtual quantity that has to be defined for each strain increments. Thus the net storage rate for a slip system  $\xi$  during a strain increment can be expressed in terms of the shear strain rate  $\dot{\gamma}^\xi$  by equation,

$$\begin{aligned}\frac{d\rho^\alpha}{dt} &= \frac{1}{b} \left( \frac{s_a^\alpha}{\mu b K_{hkl}} - y_{hkl} \rho^\alpha \right) \left| \frac{d\gamma^\alpha}{dt} \right| \\ \dot{\rho}^\xi &= \frac{1}{b} \left( \frac{s_a^\xi}{\mu b K_{hkl}} - y_{hkl} \rho^\xi \right) \left| \dot{\gamma}^\xi \right|\end{aligned}\quad (4.14)$$

where  $K_{hkl}$  is a mean free path coefficient and  $y_{hkl}$  an orientation-dependent factor responsible for dynamic recovery. The first term on the right-hand side of Eq. (4.14) is the dislocation multiplication or storage rate. The second term accounts annihilation of screw dislocations by thermally activated cross-slip and its subsequent rearrangements. When dynamic recovery is not active i.e.,

in stage II, the model yields a constant strain-hardening rate  $\theta_{II}/\mu = \alpha^2/2K\Lambda$ . Introducing dynamic recovery yields the strain hardening rate in stage III.

The above dislocation recovery and storage framework requires parameters, which depends on evolution of dislocation substructure with strain. For an accurate description of a dislocation multiplication and annihilation rates, these parameters are calculated using DDD. The following sections briefly discusses the DDD works of Madec and Kubin [113] for calculation of dislocation mean free path. In their DDD framework, the dislocation densities stored for each slip system were considered as the only state variable. They hypothesized that since both parent segments and junction lines have similar interactions with incoming mobile segments, it is convenient to lump junction densities into the densities stored in the active slip systems. Another advantage of this convention is that, it indirectly considers higher order reactions or multi-junctions between dislocation lines [114, 113], which frequently forms from an interaction production of two dislocation lines reacting with a third dislocation segment. This convention is applied in the following ways :

- mobile dislocations of system  $\xi$  may react with the stored forest density on system  $\beta$  or vice versa (see Fig. 4.1).
- junction formation for both cases can be denoted as  $\xi \rightarrow \beta$  or  $\beta \rightarrow \xi$ , where the first identifier indicates the active or gliding system.
- junction segments of type  $\xi \rightarrow \beta$  or  $\beta \rightarrow \xi$  are then assimilated into stored densities in slip systems  $\xi$  or  $\beta$  respectively.

This convention also restricts stored densities of weakly active slip systems to a small number.

Once a junction line of type  $\xi \rightarrow \beta$  is formed and lumped into slip system  $\xi$ , it cannot constitute a

forest obstacle for further incoming segments in system  $\beta$ , but it can react with all other forest slip systems of  $\xi$ . Using this convection the rate of multiplication of dislocations in a slip system can be defined.

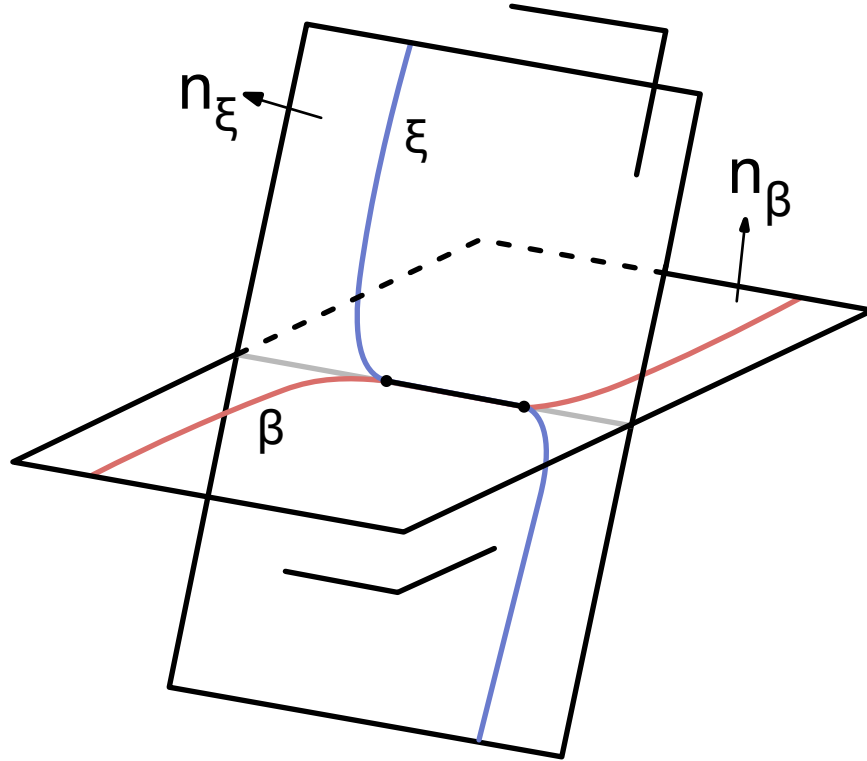


Figure 4.1: A schematic figure showing dislocation reaction between segments on active slip-system  $\xi$  (blue) and a forest system  $\beta$  (red).

### 4.2.3 Dislocation multiplication

Consider a scenario in which the dislocation lines in slip system  $\xi$  interacts with an inactive forest dislocations  $\rho^\beta$  of average length  $\bar{l}^\beta$  on slip system  $\beta$ . Then as per the convention defined earlier, all the junctions formed during the glide of dislocations  $\xi$  are assigned to slip system  $\xi$ . Thus the total amount of dislocation segments in  $\xi$  would contain two parent segments and one junction segment (Fig. 4.1). During a shear increment  $d\gamma^\xi$ , the area swept by the dislocation is  $dA^\xi =$

$d\gamma^\xi V/b$ . Let  $dN^{\xi \rightarrow \beta}$  to be the number of interactions occurring in this swept area  $dA^\xi$  and  $\varphi$  be the geometrical factor signifying the projected length of forest dislocations along the directions perpendicular to the active slip plane. Then the total length of the dislocation line stored in the volume  $dA^\xi \varphi \bar{l}^\beta$  after reaction with forest density  $\rho^\beta = dN^{\xi \rightarrow \beta} / \varphi dA^\xi$  is  $dN^{\xi \rightarrow \beta} \bar{l}^\beta$ . Therefore, the number of interactions is given as,

$$dN^{\xi \rightarrow \beta} = \varphi \rho^\beta dA^\xi = \frac{\varphi \rho^\beta d\gamma^\xi V}{b} \quad (4.15)$$

All interactions cannot form stable junctions under stress. Out of the total number of interactions, only a fraction  $f$  of them actually, forms stable junctions. The fraction  $f$  of stable junctions depends on the interactions strength  $\sqrt{A_{\xi\beta}}$  between slip system  $\xi$  and  $\beta$ . Thus, the number of stable junctions is then given as,

$$\begin{aligned} dN_{\text{jct}}^{\xi \rightarrow \beta} &= \frac{\varphi \sqrt{A_{\xi\beta}} \rho^\beta d\gamma^\xi V}{b} \\ dN_{\text{jct}}^{\xi \rightarrow \beta} &= \varphi f \frac{V}{b} \left( \sqrt{A_{\xi\beta}} \rho^\beta \right) d\gamma^\xi \end{aligned} \quad (4.16)$$

For each stable junction of length  $\bar{l}^\xi$ , the dislocations stored in the system is incremented by  $\bar{l}^\xi / V$ . So for  $dN_{\text{jct}}^{\xi \rightarrow \beta}$  interaction events, the total increase in dislocation density  $d\rho^\xi$  is given as,

$$d\rho^\xi = \frac{\bar{l}^\xi dN_{\text{jct}}^{\xi \rightarrow \beta}}{V} \quad (4.17)$$

Combining Eq. (4.17) with Eq. (4.16) for all slip systems, one can arrive at an expression for dislocation multiplication rate as follows.

$$\frac{d\rho^\xi}{d\gamma^\xi} = \frac{p_0 \bar{l}^\xi}{b} \left( \sum_{\beta=1, \beta \neq \xi}^{N_{\text{slip}}} \sqrt{A_{\xi\beta}} \rho^\beta \right) \quad (4.18)$$

where  $N_{\text{slip}}$  is the total number of slip systems and  $p_0 = \varphi f$ .  $\bar{l}^\xi$  is the average stored dislocation length which can be approximated as  $\bar{l}^\xi = k_0 / \sqrt{\sum_{\beta} A_{\xi\beta} \rho^\beta}$  with  $k_0$  being a dimensionless

constant. Since the average length of stored dislocation segments is directly proportional to the dislocation density, therefore the ratio should be constant [16].

$$\frac{\rho_{\text{jct}}^{\xi}}{\rho^{\xi}} = \frac{\bar{l}_{\text{jct}}^{\xi}}{\bar{l}^{\xi}} = \kappa_0 \quad (4.19)$$

This ratio is important as it will be used later to simplify the dislocation multiplication rate.

So far it was assumed that the forest dislocations segments were inactive. Relaxing this conditions results in a modification to the junction densities and the average length of stored dislocation content. A dislocation segment moving on a forest system  $\beta$  interacts with active slip system  $\xi$  and can form junctions on slip system  $\beta$ . Thus a fraction of stored dislocation content on  $\xi$  is transferred to system  $\beta$  i.e.

$$\rho^{\xi} = \rho_0^{\xi} - \rho_{\text{jct}}^{\beta \rightarrow \xi} \quad (4.20)$$

where  $\rho_0^{\xi}$  is the dislocation density on the active slip system  $\xi$  for non-active forest. Similarly, the average dislocation segment length can be modified as

$$\bar{l}^{\xi} = \frac{k_0}{\sqrt{\sum_{\beta=1}^{N_{\text{slip}}} A_{\xi\beta} (\rho^{\beta} + \rho_{\text{jct}}^{\xi \rightarrow \beta})}} \left( \frac{\rho^{\xi}}{\rho^{\xi} + \rho_{\text{jct}}^{\beta \rightarrow \xi}} \right) \quad (4.21)$$

Substituting Eq. (4.21) in Eq. (4.18), the dislocations multiplication rate in the case of active forest systems can be derived.

$$\frac{d\rho^{\xi}}{d\gamma^{\xi}} = \frac{1}{b} \frac{p_0 k_0}{\sqrt{\sum_{\beta=1}^{N_{\text{slip}}} A_{\xi\beta} (\rho^{\beta} + \rho_{\text{jct}}^{\xi \rightarrow \beta})}} \left( \frac{\rho^{\xi}}{\rho^{\xi} + \rho_{\text{jct}}^{\beta \rightarrow \xi}} \right) \left( \sum_{\beta=1} \sqrt{A_{\xi\beta} \rho^{\beta}} \right) \left( 1 - \frac{\rho_{\text{jct}}^{\beta \rightarrow \xi}}{\rho^{\xi}} \right) \quad (4.22)$$

Devincre et al. [16] proposed a simplified version of Eq. (4.22) using the parameters described earlier.

$$\frac{d\rho}{d\gamma} = \frac{1}{b\Lambda} = \frac{p_0 k_0}{b} \frac{\rho_{\text{forest}}}{\sqrt{\rho_{\text{total}} (1 + \kappa)^{3/2}}} \left( 1 - \frac{\kappa}{n-1} \right) \quad (4.23)$$

where  $n$  is the number of slip systems,  $\kappa = \kappa_0/(1 - \kappa_0)$  i.e. the fraction of junction density to the fraction of non-junction density and  $\Lambda$  is the dislocation mean free path. Lumping all constant coefficients into a dimensionless and orientation-dependent coefficient  $K_{\text{hkl}}$ , the mean path  $\Lambda$  can eventually be set in the simple form.

$$\Lambda = \frac{K_{\text{hkl}}}{\sqrt{\bar{a}\rho_{\text{total}}}} \quad (4.24)$$

The coefficient  $K_{\text{hkl}}$  depends on the average interaction strength and on the set of constants  $p_0$ ,  $k_0$  and  $\kappa_0$  (or  $\kappa$ ).

#### 4.2.4 Dislocation annihilation

**Critical annihilation distance:** Two screw dislocations of opposite sign gliding in parallel slip planes separated by a distance smaller than a critical distance  $y_s$  can mutually annihilate by cross-slip. Although this quantity is widely used in many models, there is presently no accurate theoretical prediction for it, as it derives from a thermally activated core mechanism. Furthermore, the density of screw dislocations is a small, but as yet unknown, fraction  $f$  of the total dislocation density because screw dipoles annihilate more easily than edge dipoles. As the present model is written in terms of total densities, Eq. (4.14) actually includes a length  $y_{\text{hkl}} = fy_s$ . The value of  $y_{\text{hkl}}$  is adjusted to yield the experimentally observed critical stress for the onset of the dynamic recovery stage. An example is shown in [16] for copper at room temperature where,  $y_{\{123\}} = 0.5$  nm. From the classical work of [115] one has  $y_s \approx 50$  nm in persistent slip bands of copper crystals cycled at 300 K. In that case, the ratio of screw to edge or total densities is about 1/100 and the value determined for  $y$  looks reasonable.

The critical annihilation distance is also orientation-dependent, which entails an orientation dependence of the onset of stage III in the stress-strain curves. It was shown by Kubin et al. [116]

that this effect is of geometrical origin and arises from the respective orientation dependencies of the Schmid factors in the slip and cross-slip planes. The results obtained in Kubin et al. [116] are expanded to yield a value of the quantity  $y_{hkl}$  for any orientation  $[h, k, l]$  of the loading axis.

Table 4.6 summarizes the list of variables used in the model, with adjustable parameters  $K_{hkl}$ ,  $y_{hkl}$ ,  $\rho_0^{\{110\}}$ ,  $\rho_0^{\{112\}}$ , and  $s_t^\xi$ .

Table 4.6: Material variables for dislocation density based model

Elastic			Plastic							Strain hardening			
$C_{11}$	$C_{12}$	$C_{44}$	$\rho_0^\xi$	$s_t^\xi$	$v_0$	$b$	$\Delta G_0$	$T$	$p$	$q$	$A_{\xi\beta}$	$K_{hkl}$	$y_{hkl}$
GPa	GPa	GPa	$m^{-2}$	MPa	$msec^{-1}$	$\text{\AA}$	J	K					nm

## CHAPTER 5

### RESULTS AND DISCUSSION

The outcome of the simulated deformation behavior using the constitutive framework discussed in Chapters 3 and 4 is presented in this chapter. This chapter discusses details about the crystal plasticity constitutive model calibration, sensitivity of the primary model parameters ( $\rho^{\xi}, A_{\xi\beta}$ ) and identification of relevant state parameter evolution that is crucial to capturing the physics of the deformation process.

#### 5.1 Calibration of Crystal Plasticity constitutive model

The mechanical response of a single crystal undergoing uniaxial tension (using “standard” dog-bone samples) exhibits marked spatial gradients between the central and peripheral gauge sections. Capturing the fidelity through full-field simulations requires a well suited constitutive description with proper combinations of primary state variables (input parameters). These input parameters are obtained by optimizing the simulated output with respect to a handful of experimental data. In the present study, the crystal plasticity model is calibrated by optimizing the simulated uniaxial stress-strain curves with respect to experimental data collected by [12, 75]. The optimization process used in this study has been discussed in elaborate details in Chakraborty and Eisenlohr [15].

One of the problems faced during inverse optimization of constitutive models is the computational cost involved. The simulated stress-strain response is frequently calculated based on various combinations of input parameters within a solution space until the desired accuracy is achieved. The error in each minimization is calculated using an objective function. In this particular case, an

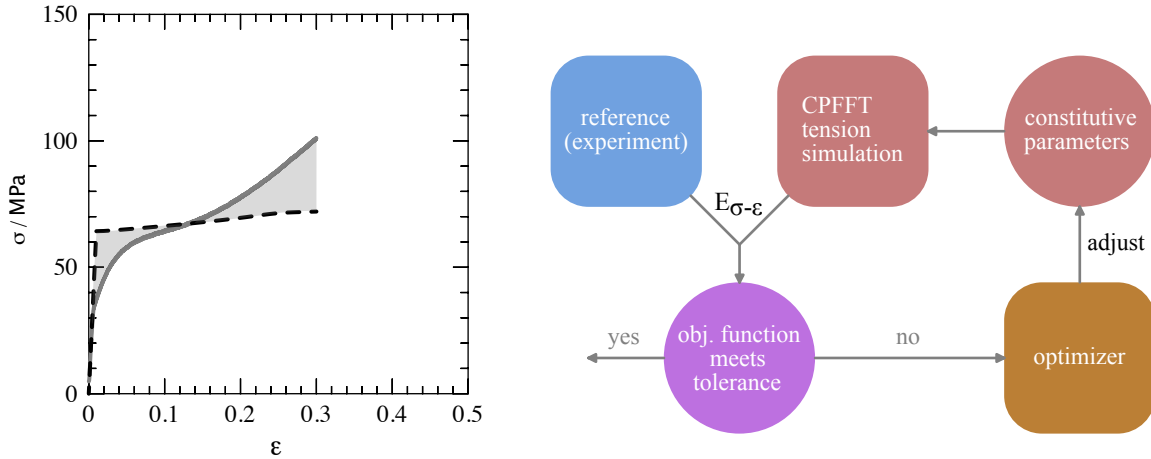
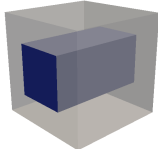
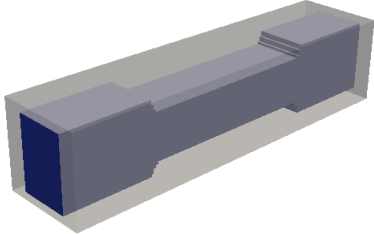


Figure 5.1: Left : Optimization function minimizing the area between two curves. The gray line represents the standard curve, which the dashed black line represents the trial curve. Right : Flow diagram of the optimization process used by Chakraborty and Eisenlohr [15].

objective function was designed to minimize the error in the area under the two stress-strain curves (see Fig. 5.1 left). The computationally expensive step in this optimization process is the CPFPT calculation step. Therefore it is essential to identify the boundary conditions which are most important to mimic the behavior of single crystal samples with a much smaller geometry (low mesh resolution).

The second column of Table 5.1 shows the geometries used to simulate the deformation behavior. To reduce the CPFPT computation cost, a rectangular block of gauge section with reduced mesh resolution is subjected to the same boundary conditions as the dogbone sample itself. A buffer layer of soft, dilatational and low stiffness material (see Chapter 3) is added surrounding the dogbone and the cube geometry to mimic free surface boundary conditions in the spectral solver. The resolution of the reduced geometry is varied from  $4 \times 4 \times 4$  to  $12 \times 12 \times 12$  for different orientations. The corresponding average computation time for these geometries is reported in the last column. The resulting stress (strain) response of each of these simplified reduced geometries is then compared to the stress (strain) response of the gauge section of the dogbone geometry us-

Table 5.1: Comparison of CPFPT computation time between simplified reduced geometry of gauge section and a proper dogbone shaped geometry. Material described by crystal plasticity law is shown in blue and the dilatational buffer layer is shown in light gray.

	<b>Geometry</b>	<b>Resolution</b>	<b>Computation time [min]</b>
reduced		$4 \times 4 \times 4$	1.617
		$6 \times 6 \times 6$	4.883
		$8 \times 8 \times 8$	10.270
		$10 \times 10 \times 10$	23.130
		$12 \times 12 \times 12$	38.100
dogbone		$35 \times 160 \times 26$	2263.300

ing Kernel Density Estimation (KDE) plots. The KDE plots of all the components of the stress (strain) behavior for both reduced and gauge section of dogbone geometry is shown in Fig. 5.2. The top row shows the correlation of the normal stress components and the bottom row shows the correlation of shear stress components. It is noted that the normal stress (strain) response of these reduced geometries along the loading direction (top row middle column Fig. 5.2) is remarkably similar (Pearson correlation  $r = 0.97$ ) to that of the gauge section of dogbone geometry. However, the other transverse normal components and the shear components vary from weak correlation (Pearson correlation  $r = 0.5$ ) to no-correlation (Pearson correlation  $r = 0.0053$ ). Given that, the absolute magnitudes of the transverse and shear stress components are way below the flow stress of the material, deviations in these components have small effects on the resultant slip behavior and therefore can be ignored. Thus the reduced geometry can be used to approximate the deformation of the gauge section of dogbone sample for faster optimization of input parameters.

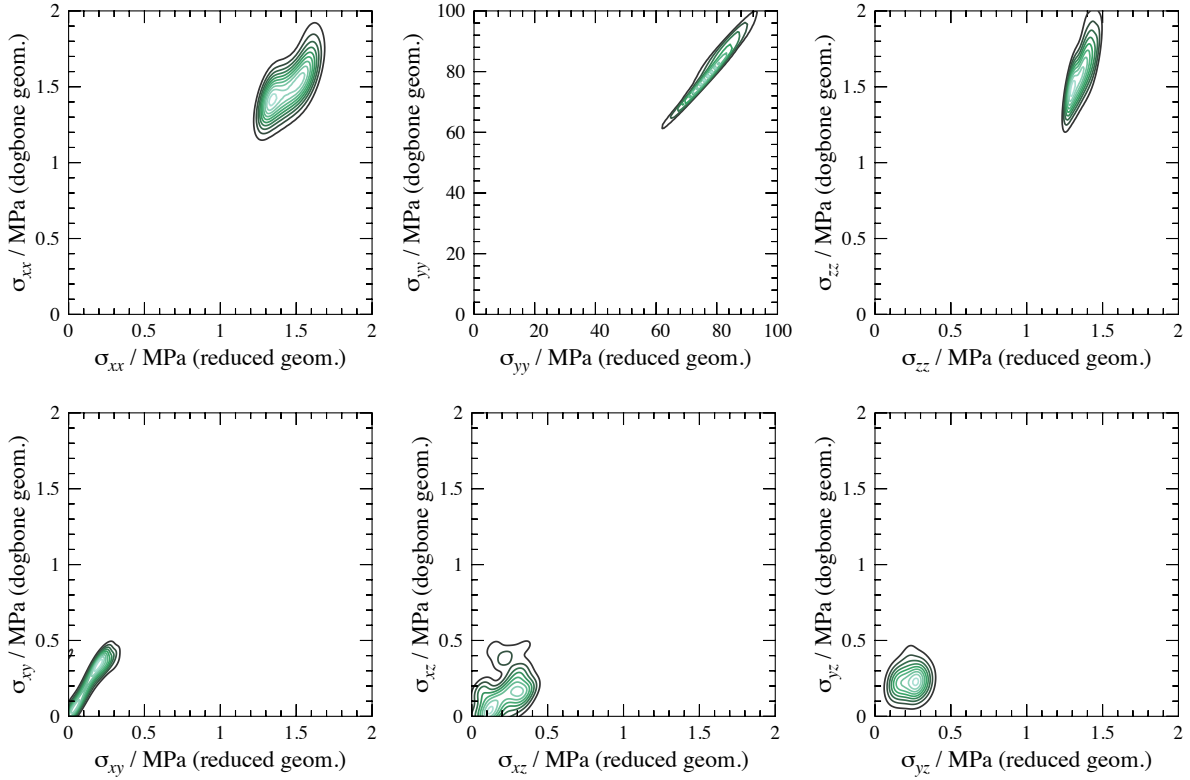


Figure 5.2: Comparison of stress components of simplified reduced geometry and gauge length section of dogbone geometry in terms of kernel density estimation maps. The top row shows the correlation of the normal stress components and the bottom row shows the correlation of shear stress components.

## 5.2 Phenomenological constitutive model results

Phenomenological models have been long used in crystal plasticity modeling to predict deformation response of materials, particularly FCC metals. As discussed in the earlier chapter, the essence of a phenomenological model relies on the CRSS for a particular slip-system. Although much work on single crystal plasticity of BCC metals has been devoted to  $\alpha$ -Fe, Mo, W and Ta, very little work has been done on Nb. Mapar et al. [117] used a rate-independent model with exponential and dynamic hardening rules to predict strain hardening in Nb. As a first attempt, a rate-dependent phenomenological crystal plasticity model (see Chapter 4) is used to predict the strain hardening. The important model parameters  $\tau_0$ ,  $\tau_{sat}$  and  $h_0$  are optimized using the frame-

work discussed in earlier section.

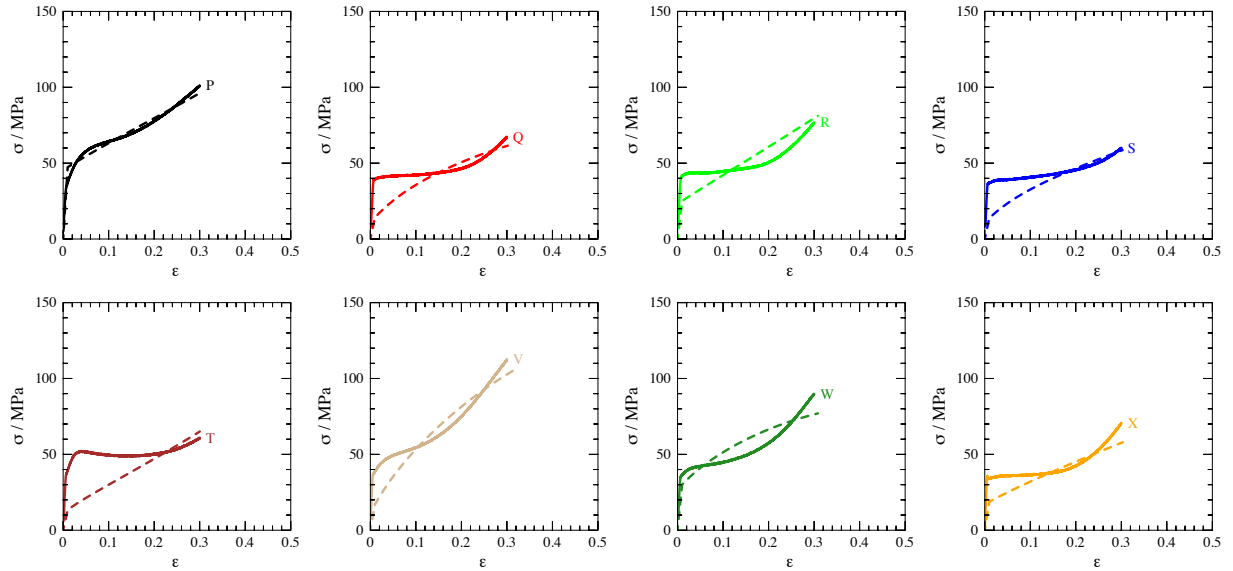


Figure 5.3: Comparison of experimentally observed axial stress-curves with the ones predicted using phenomenological crystal plasticity model as function of orientation. Solid lines indicate the measured stress-strain curves while the predicted ones are shown in dashed lines.

Figure 5.3 shows the resulting stress-strain curves predicted by the phenomenological model along with their experimentally measured ones. The model seems to work only for the orientations which do not show marked changes in the hardening rates in between stage I and stage II. However, for most of the orientations, the model fails to capture the change in hardening behavior over the strain range. In almost all cases the rate of hardening predicted by the model matches closely with the stage II hardening rate, but no sign of stage I deformation is observed in the predicted behavior. The initial CRSS  $\tau_0$ , saturation CRSS  $g_\infty$  (for two slip families  $\{110\}$  and  $\{112\}$ ) and the hardening slope  $h_0$  obtained from the best-fitted simulations for each of these orientations are shown in Fig. 5.4. A relatively small variation in hardening slope  $h_0$  and  $\tau_0$  is observed along with a wide variation in  $g_\infty$  over the range of crystal orientation.

These observations suggests that for predicting a variable hardening rate with consistent CRSS

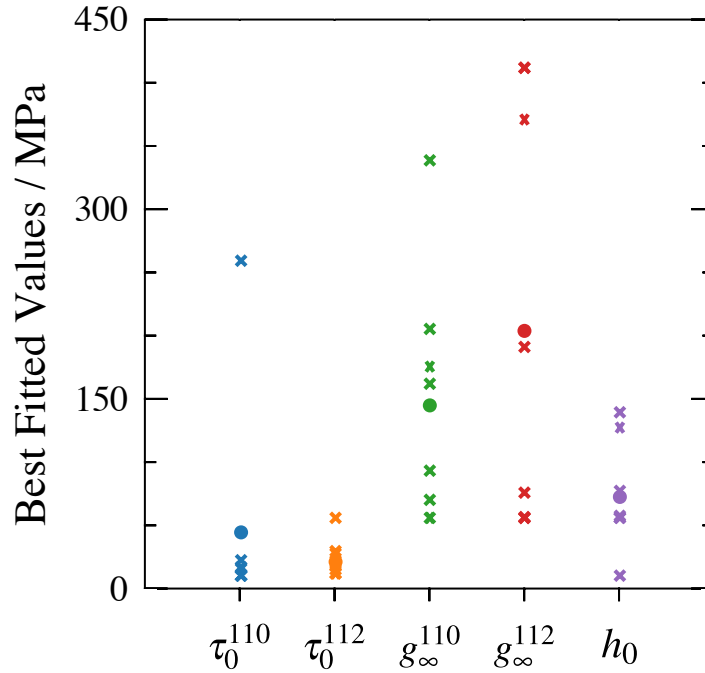


Figure 5.4: Adjustable phenomenological model parameters (initial CRSS  $\tau_0$  saturation CRSS  $g_\infty$  and hardening slope  $h_0$ ) for pure Niobium obtained from stress-strain curve optimization of 8 single crystal orientations. The crosses represent a parameter for a particular orientation. The mean of the parameters for all orientations is represented by a solid dot.

over the orientation space one needs to treat the hardening behavior in different stages separately. Such models with multiple-hardening laws for various stages has been investigated in the works of [118, 119].

### 5.3 Dislocation density based crystal plasticity model results

The dislocation density based crystal plasticity model described in section 4.2 is used to predict deformation behavior of the dogbone geometries for the orientations reported by Baars [12]. Table 5.3 presents the underlying values of the model parameters with adjustable variables.

Table 5.2: Constitutive material parameters of pure Nb used for the crystal plasticity simulations of uniaxial tension. The asterisk (\*) indicates fitting parameters.

Parameter	Value
$C_{11}$	246.5 GPa
$C_{12}$	134.5 GPa
$C_{44}$	28.73 GPa
$\mu$	39.6 GPa
$\rho_0^{\{110\}}$	*
$\rho_0^{\{112\}}$	*
$b$	3.3 Å
$v_0$	$10^{-4} \text{ m s}^{-1}$
$\Delta G_0$	$2.72 \cdot 10^{-19} \text{ J}$
$T$	300 K
$s_i^\xi$	8.5 MPa
$p$	0.85
$q$	1.27
$K_{hkl}$	*
$y_{hkl}$	*
$A_{\xi\beta}$	Table 4.5

### 5.3.1 Slip activity maps as a function of orientation

To determine the slip-activity as a function of orientation, the implemented dislocation density based crystal plasticity model is used assuming  $\langle 111 \rangle \{110\}$  and  $\langle 111 \rangle \{112\}$  as possible slip-systems populated with equal amounts of dislocations. Based on the net accumulated shear  $\Gamma_{acc}$  at the onset of slip ( $\epsilon \sim 0.002$ ), active slip family is mapped as a function of orientation. Fig. 5.5 shows the dominant slip-family determined a function of orientation. Similar slip behavior in BCC metals was also reported in the works of Calnan and Clews [120]. However, it is observed that with continued plastic deformation the active slip family changes drastically and is mostly of  $\langle 111 \rangle \{112\}$  type for majority of the orientations in the standard stereographic triangle except near the orientations with very high Schmid factor on  $\langle 111 \rangle \{110\}$ .

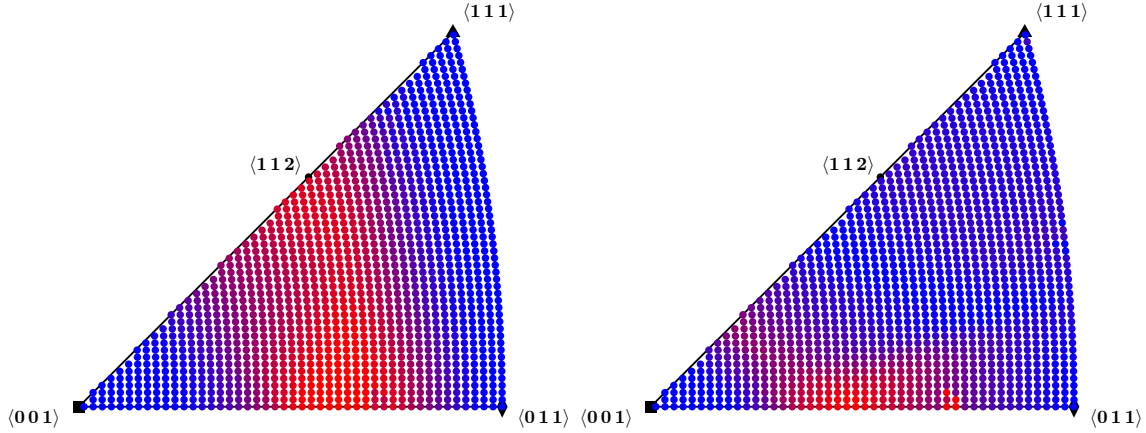


Figure 5.5: Active slip family based on net accumulated shear  $\Gamma_{acc}$  as a function of orientation. The contribution of a slip family for each of the orientations is represented by a color varying from blue for pure  $\{112\}$  to red for pure  $\{110\}$  slip. Left: active slip family maps at  $\varepsilon \sim 0.002$ . Right: active slip family maps at  $\varepsilon \sim 0.050$ .

### 5.3.2 Influence of slip family on spatially resolved deformation behavior

The reduced geometry described earlier is computationally efficient and robust for model calibration, however, it cannot reproduce spatially varying heterogeneous deformation of the dogbone shaped sample under tension. For this purpose, CPFDD simulations were done on a dogbone geometry for all the eight orientations with the optimized dislocation density model's optimized parameter set. Three different slip conditions were considered in which the deformation on the slip systems was restricted to (a) only  $\{110\}$  slip planes, (b)  $\{110\}$ ,  $\{112\}$  slip planes and (c) only  $\{112\}$  slip planes.

The local inverse pole figure, von Mises strain and von Mises stress field maps are shown in Figs. 5.6 to 5.8 respectively for all the three slip conditions mentioned above. Some interesting observations were made. In a few of the orientations  $(P, T)$ , the active slip family determined the amount of necking in the latter stages of deformation. Moreover, marked differences were observed in the final orientation of the necked region. The same behavior has also been detected in the local von Mises stress fields. In the case of the other orientations the stress localization patterns

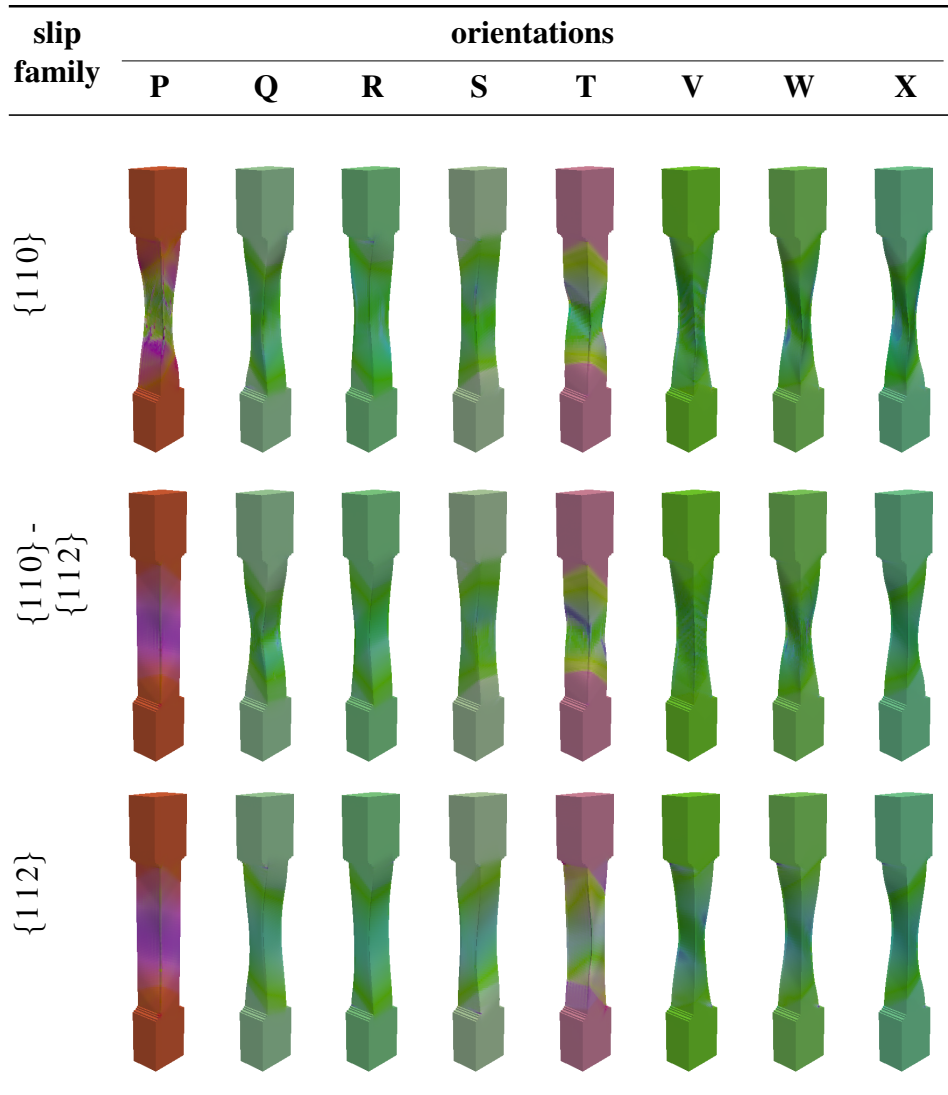


Figure 5.6: Local  $\langle 010 \rangle$  lattice reorientations maps of the deformed dogbone samples. Rows in descending order represent the simulation results obtained assuming  $\{110\}$ ,  $\{110\}$ - $\{112\}$  and  $\{112\}$  slip family respectively.

(alternating regions of high and low stress) seems to be dependent the active slip family. For some of the orientations, stress localization is only observed only when slip is restricted to single slip family. Overall, the final shape of the deformed geometry was found to be similar across all three cases for most of the orientations.

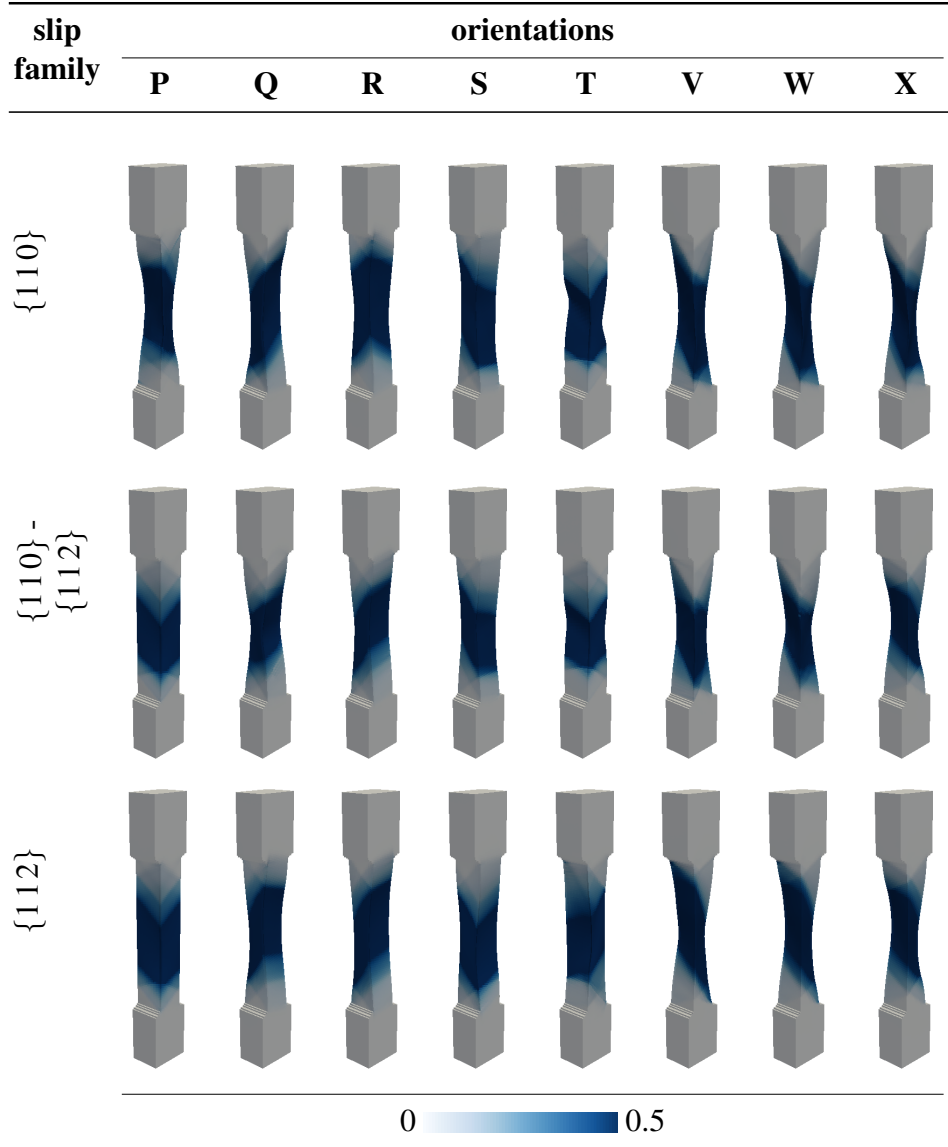


Figure 5.7: Local von Mises strain  $\varepsilon_{vM}$  maps of the deformed dogbone samples. Rows in descending order represent the simulation results obtained assuming {110}, {110}-{112} and {112} slip family respectively.

### 5.3.3 Model sensitivity to initial dislocation density

The primary state variable for the dislocation density based model is the dislocation density content on individual slip-systems. Given that it is impractical to measure dislocation content on individual slip-systems experimentally, it becomes essential to know the bounds of the CPFEM simulations up to which the predicted deformation response can be captured with reasonable accuracy.

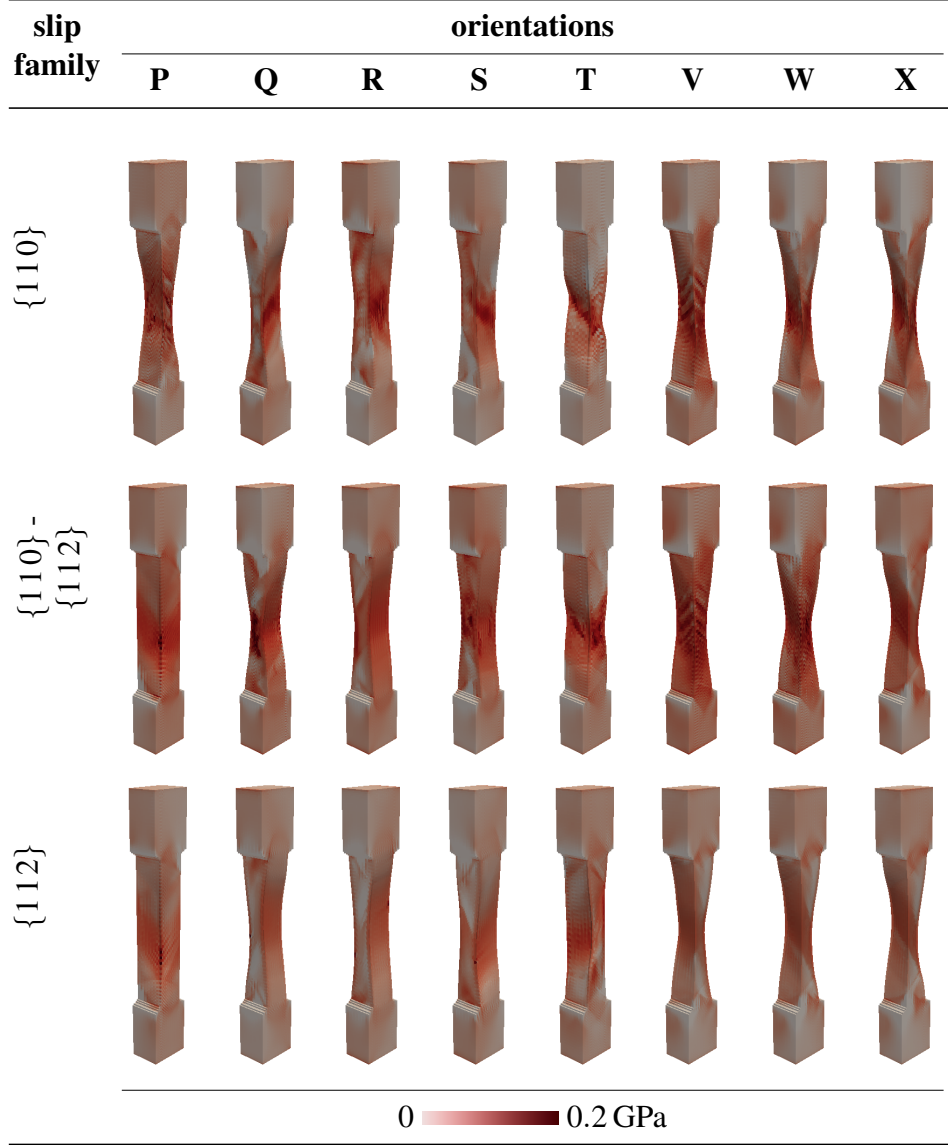


Figure 5.8: Local von Mises stress  $\sigma_{VM}$  maps of the deformed dogbone samples. Rows in descending order represent the simulation results obtained assuming  $\{110\}$ ,  $\{110\}$ - $\{112\}$  and  $\{112\}$  slip family respectively.

The influence of initial conditions on deformation response was tested by distributing dislocation content inhomogeneously among individual slip-systems. The distribution of dislocation densities followed a log-normal distribution with a mean dislocation density,  $\rho_{\text{mean}}$  and variance  $\sigma_{\rho}$ . The range of the distribution was varied by changing the variance. Three variations were tested i.e  $\sigma_{\rho} = 0.5, 1.0$  and  $2.0$  around a mean dislocation density of  $\rho_{\text{mean}} = 2 \times 10^{13}$ . For each distribu-

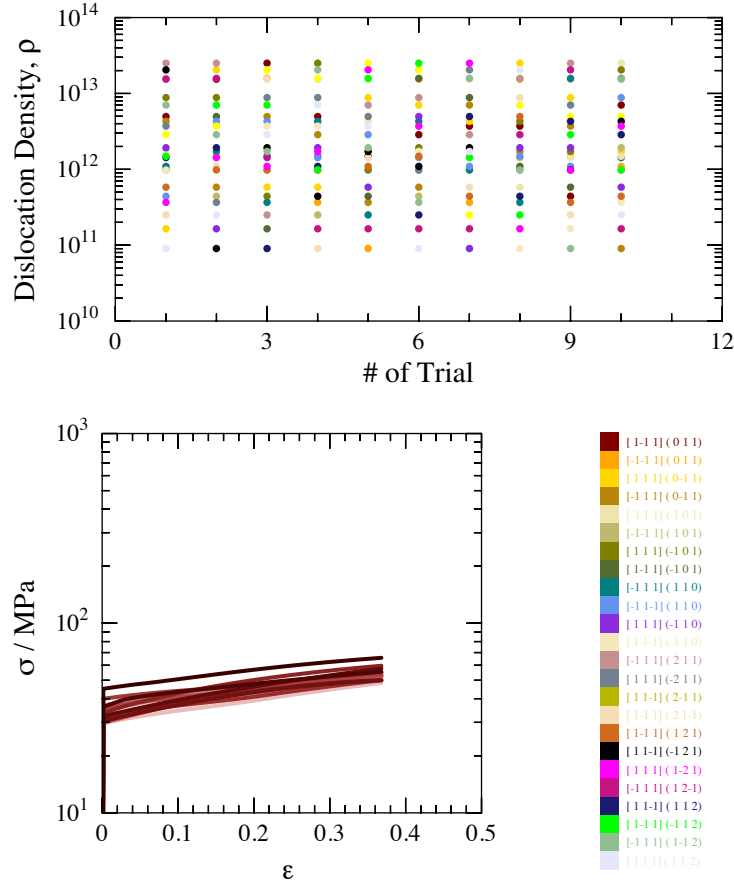


Figure 5.9: Influence of pre-deformed dislocation content on stress-strain response (lower left) simulated by dislocation density based model. The top row shows several instances of inhomogeneous distribution of dislocation content on individual slip systems for a chosen log-normal dislocation statistics. Each slip system is denoted by a color key given in the lower right legend.

tion characteristic  $(\rho_{\text{mean}}, \sigma_{\rho})$ , several random instances of the distributions were generated. The resulting effect on stress-strain response and lattice-reorientation is reported.

Fig. 5.9 shows the influence of inhomogeneous dislocation content on the stress-strain response. It was observed that the flow stress of the material is sensitive to the initial dislocation content. Fig. 5.10 shows the influence of  $\sigma_{\rho}$  on the tensile axis re-orientation for three different orientations. For each orientation and distribution characteristics, 10 different instances were simulated. It was observed that for a smaller inhomogeneity, the lattice re-orientation trajectories were limited to only a few possible directions in orientations space for each of the tested orientations.

However, with the increase in the variance of the distribution, the tensile axis re-orientation became more chaotic and unpredictable.

The above behavior is expected since the mobile dislocation content controls the deformation process. For a given loading conditions, if the slip system with highest RSS is low on mobile dislocation content, then the flow-stress has to increase to activate new sources for deformation to continue. Due to this reason, the initial flow stress observed in Fig. 5.9 increased for certain distribution instances where the slip system with highest Schmid factor has low mobile dislocation content. Secondly, the distribution of initial dislocation content on non-active systems influences the forest hardening. Thus, depending on the amount of particular forest dislocation content present during flow, the tensile axis orientation can change due to different easy paths offered during deformation. Hence, the less inhomogeneous a material is, the fewer number of paths available for the lattice to reorient during deformation.

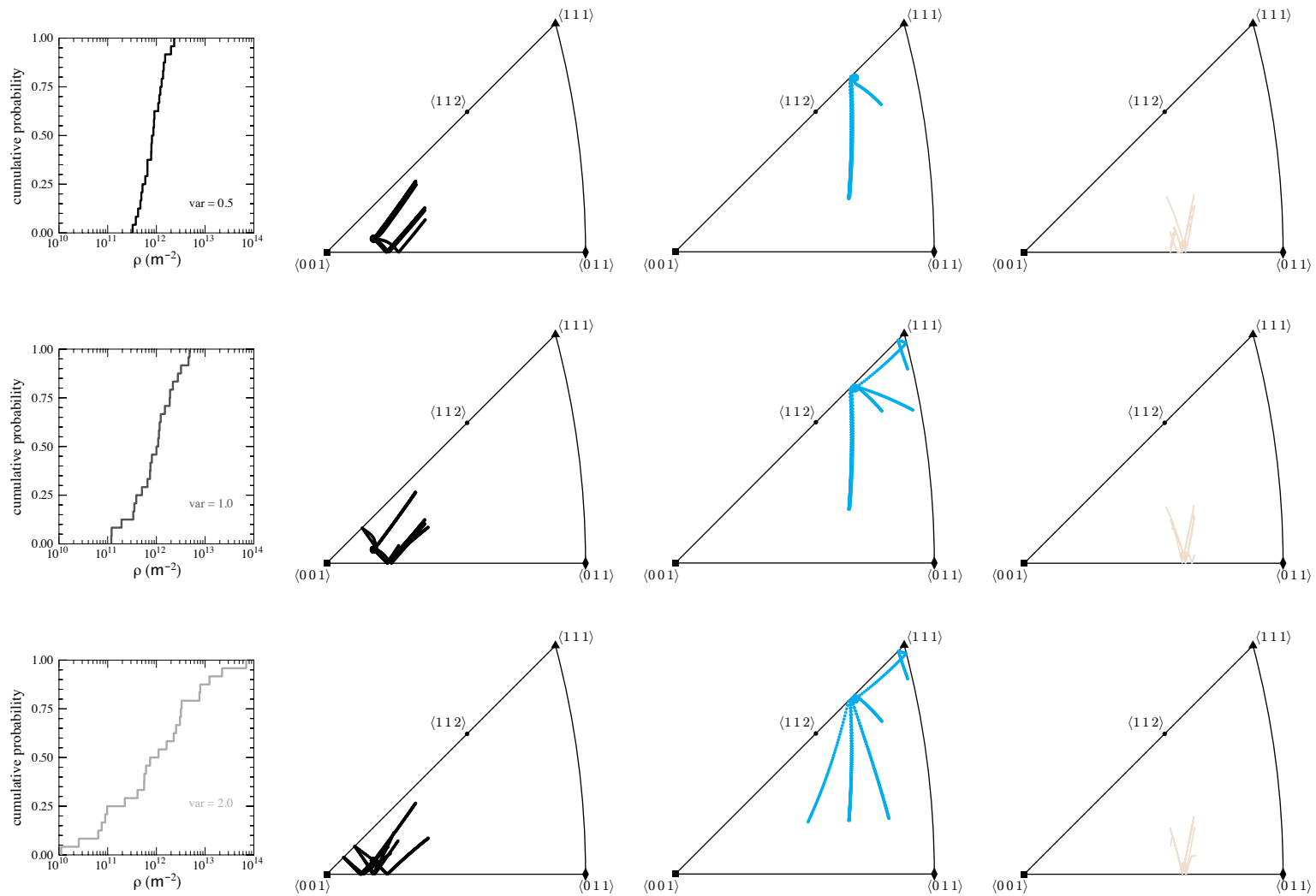


Figure 5.10: Influence of pre-deformed dislocation content on lattice reorientation for three different orientations simulated by dislocation density based model. The left column shows the probability distribution of pre-deformed dislocation content with  $\rho^m = 1 \times 10^{13} \text{ m}^{-2}$  and different variances. The corresponding lattice reorientation trajectories for three orientations are shown in the right three columns.

### 5.3.4 Influence of dislocation interaction coefficients on strain hardening

Fig. 5.11 shows the tensile axis re-orientation and axial stress-strain response of the best-fitted simulation results for the eight orientations simulated with isotropic Fe interaction coefficients [2]. The tensile axis re-orientation predicted by the model is similar to that observed by Baars [12], Jaoul and Gonzalez [8], Keh [9], Duesbery et al. [74]. The tensile axis for most of the orientations lying in the center of standard stereographic triangle changes trajectory after crossing the  $\{001\}$ – $\{101\}$  line. The maximum amount of angular distance traversed by the stress-axis in the adjacent standard triangle is determined by how close the initial orientation is to the  $\{001\}$ – $\{101\}$  boundary.

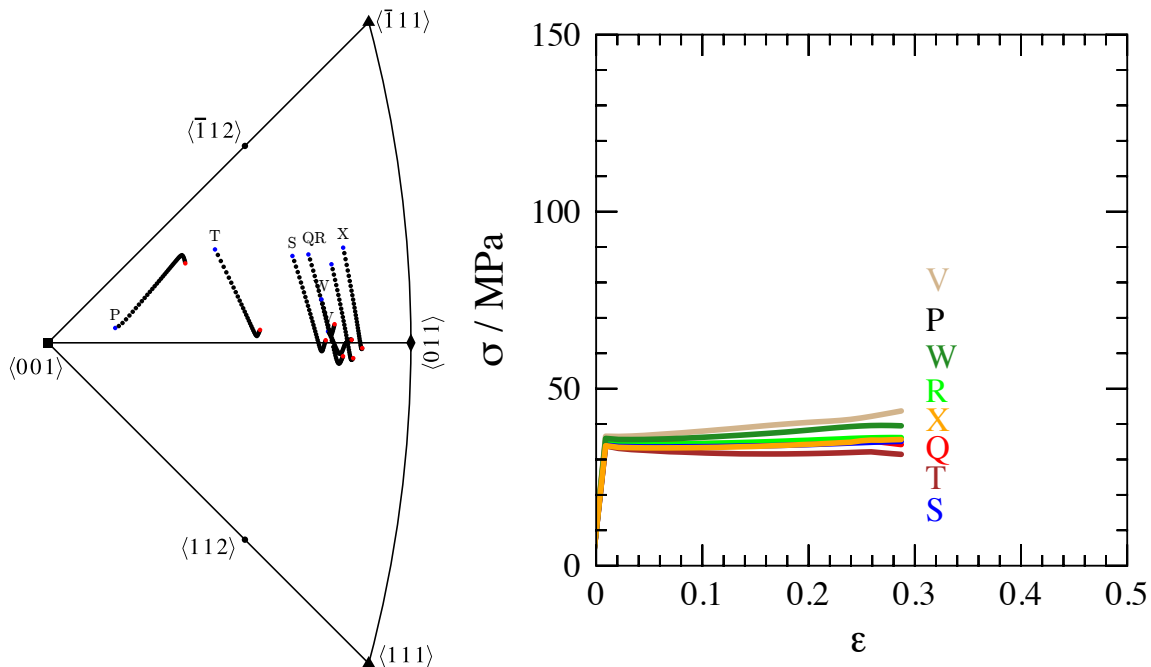


Figure 5.11: Results predicted by the dislocation density based model with isotropic  $\alpha - Fe$  interaction coefficients. Left:  $\langle 010 \rangle$  inverse pole figure for the 8 orientations showing the tensile axis re-orientation as a function of strain ( $\epsilon_{\max} = 0.30$ ). The initial tensile axis orientation is denoted by the blue dot. The final orientation after 30% strain is indicated by the red dot. The black dots in-between represents the trajectory of reorientation. Right: Corresponding axial stress-strain ( $\sigma - \epsilon$ ) predicted by the crystal plasticity model.

The rate of hardening observed in stage II deformation of the simulated single crystal uniaxial tension differs significantly from the experimental behavior. A negligible rate of hardening in stage II is observed in axial stress-strain behavior for most of the orientations. The reason for such low hardening is due to the fact that the used interaction coefficients were calculated for  $\alpha$ -Fe (BCC) assuming an isotropic elasticity. Until recently, it was believed that these interaction coefficients are directionally symmetric and depend only on the lattice structure. However, Madec and Kubin [3] predicted that the anisotropic elasticity has an effect on the dislocation interaction coefficients and is, therefore, material dependent. Moreover, it was also demonstrated that some of the dislocation junction reactions are asymmetric in nature.

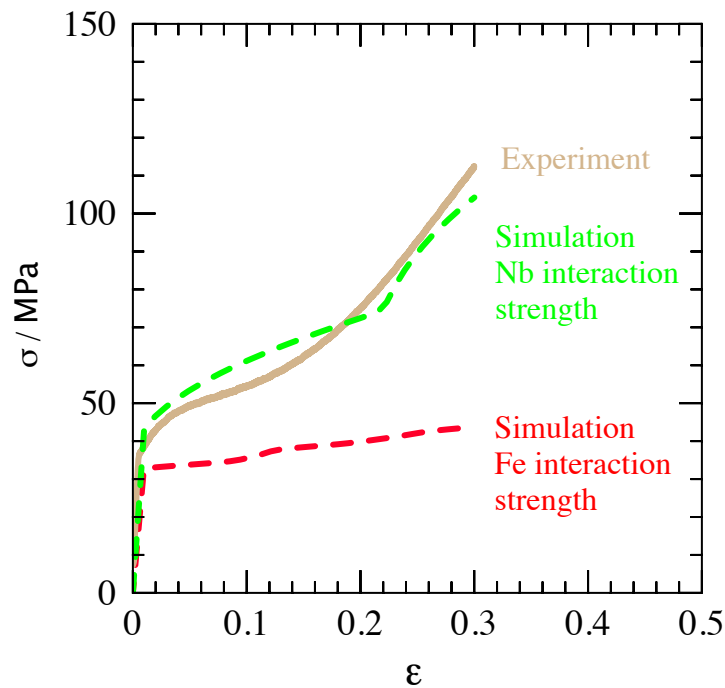


Figure 5.12: Influence of elastic anisotropy on strain hardening behavior for a particular orientation. The interaction coefficients for Fe assuming isotropic elasticity was calculated by Queyreau et al. [2]. The dislocation interaction coefficients assuming anisotropic elastic for Nb was taken from the works of Madec and Kubin [3].

Fig. 5.12 shows the influence of dislocation interaction coefficients (calculated under different

assumptions) on the rate of hardening in single crystal Nb. The black curve represents the experimentally observed stress-strain behavior. The red curve represents the stress-strain behavior simulated assuming isotropically elastic  $\alpha$ -Fe interaction coefficients, while the green curve represents the stress-strain behavior simulated using anisotropically elastic Nb interaction coefficients. It was observed that for  $\alpha$ -Fe interaction coefficients the rate of hardening is negligible, while for the Nb interaction coefficients the rate of hardening increased rapidly at onset of stage II.

### 5.3.5 Inverse optimization of dislocation mean free path coefficient

The dislocation multiplication term in the storage and recovery framework is inversely proportional to the MFP coefficient, which is orientation dependent. The MFP coefficient takes into account the probability of forming stable junctions and the number of active slip systems for the given lattice orientation. Devincre et al. [16] calculated the MFP coefficients in Al (FCC) for several symmetric orientations. In their work, it was shown that for orientations with more active slip systems the average MFP is shorter, while for low symmetry orientations (single glide case) the MFP is larger, which explains a long easy glide stage in stress-strain response.

So far these coefficients have not been reported for any BCC material in literature. Hence, in this work, the MFP coefficient is estimated using parameter optimization. It is to be noted that the optimized set of MFP coefficients are in no way absolute values for the given material or its orientations, but a result of parameter fitting with the primary objective being their qualitative trend over orientation space.

Fig. 5.13 shows the uniaxial stress–strain response for eight single crystal orientations after optimization of  $K_{hkl}$ ,  $y_{hkl}$ , and the initial dislocation content  $\rho_0^{\{110\}}$  and  $\rho_0^{\{112\}}$ . The average relative error in the difference between measured and simulated stress-strain curves for eight ori-

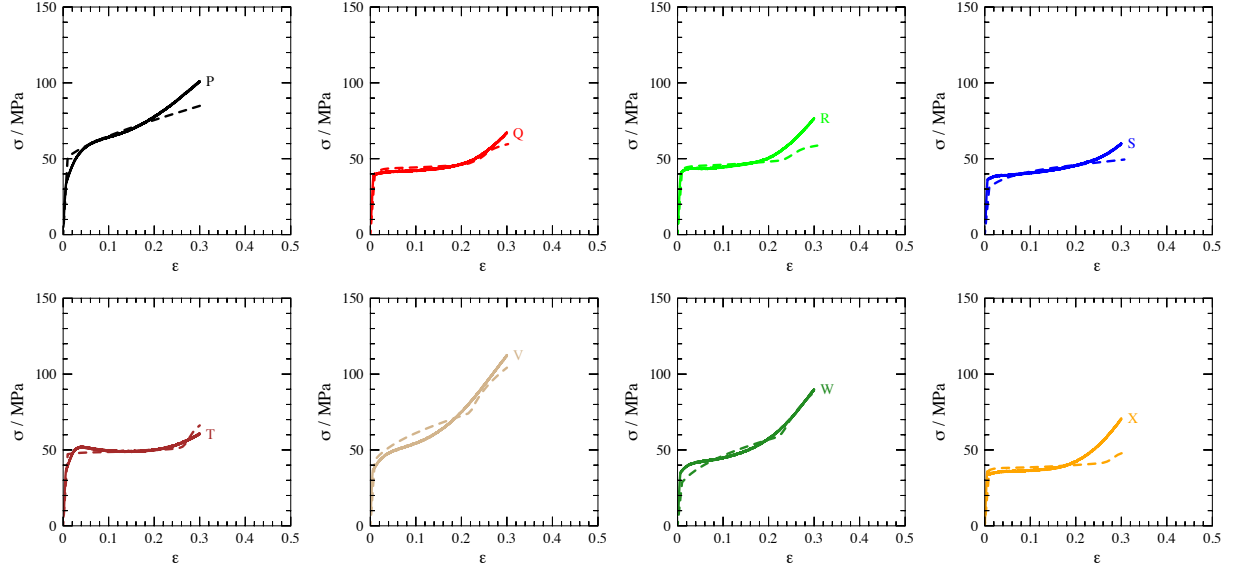


Figure 5.13: Comparison of experimentally observed (solid) and predicted (dashed) uniaxial stress–strain response for different orientations. The coefficients for mean free path  $K_{hkl}$  and dynamic recovery  $y_{hkl}$  in the model by Devincere et al. [16] were estimated using inverse optimization of the measured stress–strain curves.

entations is less than 6%. The experimentally observed variability associated with the different crystallographic tension directions is reproduced. Except for a few orientations, the stage II hardening, which starts to become apparent at strain levels of around 0.2, is generally well captured. It is observed that as the orientation moves from single glide conditions towards multiglide condition, the coefficient decreases indicating shorter average MFP i.e. higher rate of dislocation reaction and strain hardening.

Table 5.3 presents the underlying values of the adjustable parameters for all eight orientations. The annihilation distance  $y_{hkl}$ , which is governing the dynamic dislocation recovery, is not strongly dependent on the specific orientation, but assumes values of around 5 nm each. This invariance is understandable as the dislocation density accumulated during the straining is still noticeably below that density for which Eq. (4.14) would reach a dynamic equilibrium, hence, would show a strong influence of the dynamic recovery aspect.

Table 5.3: Variability in constitutive parameter values resulting from minimizing the deviation in single crystal stress–strain response for eight distinct tensile directions.

Orientation	$K_{hkl}$	$y_{hkl}$ (nm)	$\rho_0^{\{110\}}$ ( $10^{12} \text{ m}^{-2}$ )	$\rho_0^{\{112\}}$ ( $10^{12} \text{ m}^{-2}$ )
P	20.00	4.29	0.62	0.12
Q	7.25	7.25	0.12	0.05
R	12.18	7.76	0.33	0.11
S	17.45	8.34	0.09	0.02
T	15.52	5.52	0.83	0.15
V	5.56	7.16	0.08	0.07
W	7.16	4.56	0.12	0.07
X	9.58	8.58	0.04	0.11

The dislocation storage parameter  $K_{hkl}$  exhibits a notably stronger dependence on the crystallographic tensile direction. As such, the simplified storage and recovery model employed here is of limited use for general application in which complex (i.e. not only unidirectional) loadings can occur. Therefore, as a future step, the modeling of dislocation storage needs to take into account the instantaneous dislocation densities to more directly capture the kinematics and dynamics of dislocation junction formation as was already indicated by Madec and Kubin [113].

The values of initial<sup>1</sup> dislocation density ( $\rho_0^{\{110\}}$  and  $\rho_0^{\{112\}}$ ) that are necessary to match the yield stress level in each of the four single crystal experiments also exhibit an appreciable variability. Since it is difficult to accurately determine the true dislocation content in the material, a numerical study was performed to gauge the influence of this uncertainty on the predicted single crystal stress–strain response in unidirectional tension. Figure 5.14 presents for the exemplary orientation ‘V’ that even for a known (fixed) total initial dislocation content, if distributed unevenly across the individual slip systems, the resulting strain hardening can markedly differ. In the case shown, three of the realizations did not even exhibit the experimentally observed two-stage hard-

<sup>1</sup>homogeneously distributed across each of the twelve slip systems per slip family

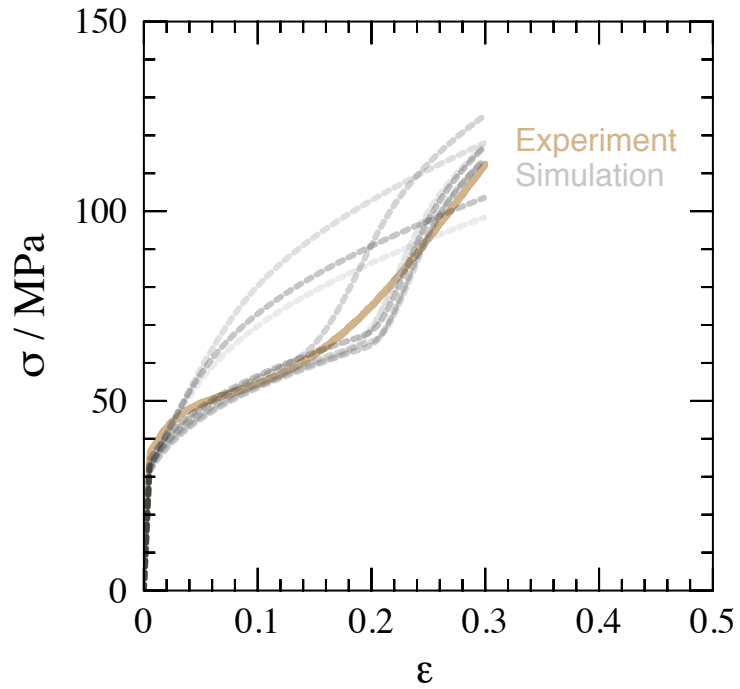


Figure 5.14: Variability in predicted single-crystal response under unidirectional tension due to different distributions among the slip systems for fixed total initial dislocation content.

ening, indicating that the precise matching of single crystal deformation is probably elusive even with rather elaborate constitutive models.

## CHAPTER 6

### CONCLUSION

In the present study, volumetric dilatation capability is added to an existing isotropic material model to capture the behavior of void-like regions in FOURIER-based spectral solvers. The ability to mimic empty space is essential to address non-compact geometries within the periodicity constraints imposed by such solvers. The model has been applied to simulate the plastic growth of a circular void in a plate under biaxial tension and the known grain-scale deformation behavior of a tensile sample containing a limited number of grains. Both cases show that the proposed formulation provides a more accurate description of void-like behavior compared to assuming a soft-elastic behavior for void volumes.

The finite strain dilatational framework is then used for crystal plasticity simulations of dog-bone shaped Niobium single crystals under tensile loading with an emphasis on multi-stage hardening, orientation dependence, and non-Schmid behavior. A constitutive model with dislocation storage and recovery rates based on Discrete Dislocation Dynamics is used to model strain hardening in stage II. Adjustable parameters in this model are identified based on an inverse strategy that uses a Nelder–Mead simplex approach to minimize the deviation between measured and simulated uniaxial single crystal tension experiments. The influence of dislocation interaction parameters and the variability on stage II hardening associated with the initial dislocation content is numerically studied and compared with tensile experiments.

The experimentally observed variability associated with the different crystallographic tension directions is reproduced effectively. Except for few a orientations, the stage II hardening, which starts to become apparent at strain levels of around 0.2, is generally well captured. The transition

from stage I to stage II is abrupt and non-smooth. This might be due to an absence of cross-slip in the constitutive description.

The annihilation distance  $y_{hkl}$ , which is governing the dynamic dislocation recovery, is not strongly dependent on the specific orientation, but assumes values of around 5 nm. The dislocation storage parameter  $K_{hkl}$  exhibits a notably stronger dependence on the crystallographic tensile direction.

The values of initial dislocation density ( $\rho^{\{110\}}$  and  $\rho^{\{112\}}$ ) that are necessary to match the yield stress level in the eight single crystal experiments also exhibits an appreciable variability. Since it is difficult to accurately determine the true dislocation content in the material, a numerical study was performed to gauge the influence of this uncertainty on the predicted single crystal stress-strain response in unidirectional tension. In the case shown, some of the realizations did not even exhibit the experimentally observed two-stage hardening, indicating that the precise matching of single crystal deformation is likely elusive even with rather elaborate constitutive models.

## 6.1 Recommendations for future work

- The transition from stage I to stage II is abrupt for the simulated stress-strain behavior. For a smooth transition in-between hardening stages, cross-slipping should be incorporated in the crystal plasticity constitutive law. Cross-slipping has been reported by several authors [121, 41, 122] to be a prominent phenomenon in BCC materials at higher temperatures. For a dislocation to cross-slip in FCC materials, the Shockley partials have to combine to form complete dislocation before gliding on a cross-slip plane, which is why cross-slip is less probable in the materials with low Stacking Fault Energy (SFE). Following the same ideology cross-slip in BCC materials should be easy since most of the BCC materials do

not form stable SF's at room temperature and above. Moreover, the availability of a vast number of possible slip planes with common  $\langle 111 \rangle$  directions makes cross-slip very likely all throughout deformation process.

- The current dislocation storage and recovery framework used to simulate the strain hardening is a simplified model and is of limited use for general application in which complex (i.e. not only unidirectional) loadings can occur. Moreover, the orientation dependence of the mean free path parameters necessitates calibration of individual orientations. Therefore, as a future step, the modeling of dislocation storage needs to take into account the instantaneous dislocation densities to more directly capture the kinematics and dynamics of dislocation junction formation as already indicated by Madec and Kubin [113].
- To correct the relative deviation in the simulated stage II hardening observed for orientations having equal probability of activating  $\langle 111 \rangle \{110\}$  and  $\langle 111 \rangle \{112\}$  slip systems, non-Schmid corrections suggested by Dezerald et al. [123] needs to be implemented.

## CHAPTER 7

### ADDITIONAL PROJECTS

#### **7.1 Influence of geometric reconstruction accuracy on grain-averaged aggregate mechanics**

##### **7.1.1 Introduction**

The elastic and, in particular, plastic mechanical behavior of single crystals is generally anisotropic. Therefore, the macroscopic mechanical response of polycrystalline materials depends primarily on the crystallite orientation distribution (“texture”). When considering their microscopic behavior at the scale of individual grains, the distributions of size and shape of constituent grains become equally important since the inherent anisotropy of single crystal deformation coupled with inter-granular interactions results in strong heterogeneity of local deformation even under uniform macroscopic loading (see, for instance, [14, 124]). Since many critical engineering aspects are governed not by average but by extreme behavior, for instance void/crack formation due to strain concentration, knowledge about and predictability of deformation at sub-granular scales is needed.

Deformation models that explicitly account for crystal plasticity have matured during the last decades and became generally quite successful in predicting macroscopic responses, i.e., at the scale of typical engineering components [76]. Application of such computational models to predict grain-scale micromechanics, however, currently results in overall agreement but notable deviations in detail compared to measurements [92]. The verification of constitutive crystal plasticity models requires experimental characterization of the initial and final material state, which primarily includes crystal orientation, plastic strain, lattice strain (stress), and defect structure. For the

simulation of grain-scale mechanics, the most critical information among these is the initial grain structure. This structure needs to be characterized non-destructively and in three dimensions, since the (easily observable) response on the surface depends notably on the actual subsurface grain structure [125, 126, 127]. Therefore, experimental techniques capable of measuring the three-dimensional arrangement of grains are essential.

With the development of third-generation synchrotron facilities such as the Advanced Photon Source (APS) at Argonne National Laboratory, X-rays of high energy (50 keV to 100 keV) and sub-micron sized beams can be generated, which have penetration depths ranging from a few millimeters to centimeters and are capable of determining properties in three dimensions, resolved at the intragranular scale. Over the years, the use of monochromatic high-energy X-rays combined with rotation of the investigated samples has led to the development of various bulk characterization techniques generally known as Three-Dimensional X-ray Diffraction (3DXRD) [128, 129, 130] or High Energy X-ray Diffraction Microscopy (HEDM) [131]. HEDM is a non-destructive way of characterizing microstructure in three dimensions [132, 133]. HEDM can be utilized with near-field and/or far-field detector positions or a combination of both. In the near-field configuration, high spatial resolution is achieved at the expense of angular resolution, by employing a small sample-to-detector distance on the order of the diffracting volume (about 1 mm to 10 mm). Orientation maps with high spatial resolution that reveal the grain morphology can be determined by post processing of the data using computationally intensive algorithms [17]. In the far-field configuration, the sample-to-detector distance is large (about 1 m) compared to the diffracting volume defined by the beam dimension. Thus, the locations of diffracted intensity on the detector are governed by (i) the incident beam energy and (ii) the lattice orientation and lattice distortion of diffracting grains. Average values of crystal orientation, lattice strain, volume and

position (centroid) can be conveniently extracted for each identified grain from the acquired sequence of detector images. Given the large effort and data intensity to measure spatially resolved grain maps using near-field HEDM compared to centroid locations using far-field HEDM, it needs to be clarified (i) how accurately a spatial tessellation based on the latter information can approximate the true grain structure that the former more directly represents, and (ii) how sensitive the grain-averaged mechanical behavior is to the geometric uncertainties around grain perimeters that result from shape reconstruction based on limited information.

The present paper first compares the geometric reconstruction accuracy when using weighted (Laguerre) Voronoi tessellation based only on grain centroids information to that resulting from combining centroids and grain volume information. Next, the plastic response of reference grain aggregates is simulated based on phenomenological crystal plasticity and compared to that of the two reconstruction alternatives to elucidate the sensitivity of grain-averaged lattice strains on the accuracy of grain morphology reconstruction.

### 7.1.2 Spatial reconstruction method

Standard Voronoi as well as weighted (a.k.a. Laguerre) Voronoi tessellation generates volume-filling cells based on a population of ‘seed’ points. The volume enclosed by the cell of site  $s_i = (\mathbf{p}_i, w_i)$ ,  $i = 1, \dots, N_{\text{grains}}$ , is

$$C_i = \left\{ \mathbf{x} \in \mathbb{R}^3 \mid d^2(\mathbf{x}, \mathbf{p}_i) - w_i \leq d^2(\mathbf{x}, \mathbf{p}_j) - w_j, j \neq i \right\}, \quad (7.1)$$

with  $d(\mathbf{x}, \mathbf{p}_i)$  being the distance between position  $\mathbf{x}$  and the (closest<sup>1</sup>) seed position  $\mathbf{p}_i$ . In case of standard Voronoi tessellation, all weights  $w_i = \text{const} = 0$ , while for Laguerre tessellation the

---

<sup>1</sup>potentially considering spatially periodic repetitions of all seed points

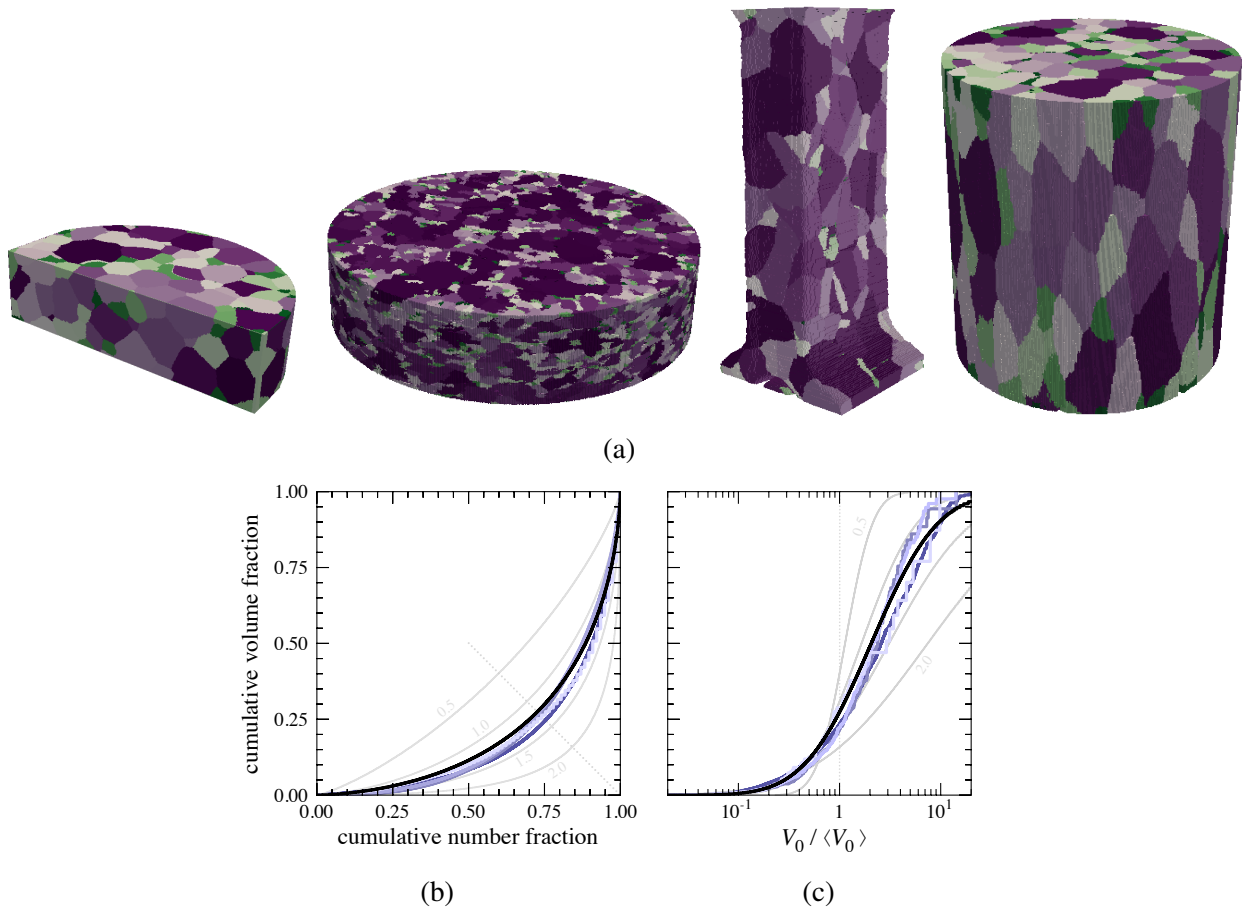


Figure 7.1: Polycrystalline aggregates (a) measured by various 3D techniques [17, 18, 19, 20] and associated grain statistics (blue curves in (b) and (c)). Sequence of four gray curves represents log-normal grain volume distributions of different variance (Eq. (7.9)); the black curve corresponds to closest fit at variance  $\sigma_{\text{distr}} = 1.2$ . Dotted line represents average grain volume.

individual weights are variable. To use Laguerre tessellation as a tool to reconstruct an aggregate of grains based on limited (spatially-averaged) data, a connection between such data and the tessellation sites (position and weight) needs to be established, as later outlined in Section 7.1.4.

### 7.1.3 Volume statistics of real and artificial grain structures

To compare the quality of grain structure reconstruction in presence/absence of grain volume information (to inform the Laguerre weights), synthetic grain structures that are statistically similar to real ones are used.

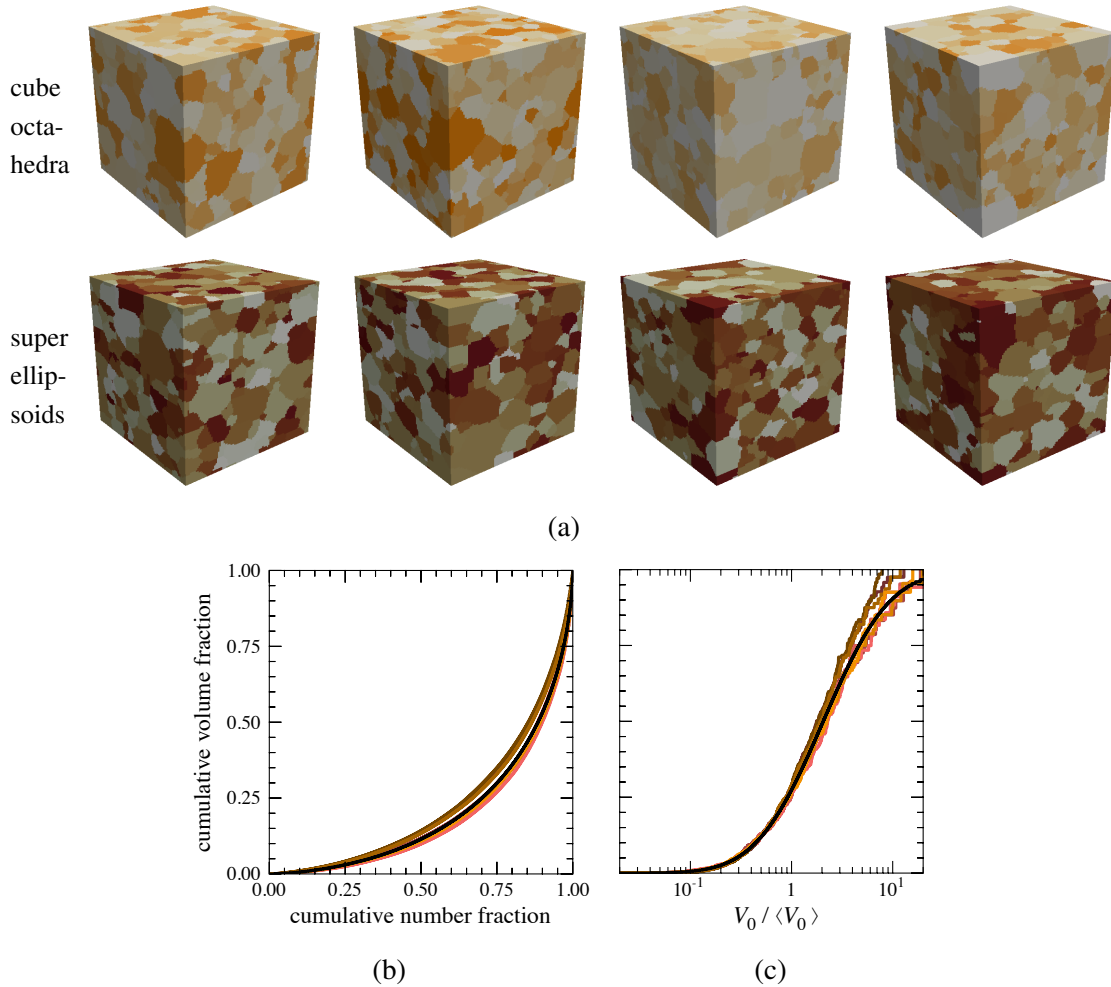


Figure 7.2: Synthetic polycrystals (a) generated by DREAM.3D [21, 22] using cube octahedra (top row) or super ellipsoids (bottom row) as grain shapes. Orange and brown curves in (b) and (c) show the associated grain statistics for both selections of grain shapes. Black line (optimal fit to experimental data) is same as in Fig. 7.1.

Four exemplary lattice orientation datasets, which were measured by various 3D techniques [17, 18, 19, 20], are shown in Fig. 7.1a and form the statistical basis of the present investigation. Grain size populations were derived from each dataset by counting the number of voxels assigned to each grain.<sup>2</sup> Figure 7.1(b) presents the relation (blue curves) between cumulative number fraction and cumulative volume fraction for each grain size population. Represented in this normalized

<sup>2</sup>Volumes of surface grains resulted from combining every member in the lower half with a random one from the upper half of their volume-sorted population.

way, all four grain populations are remarkably similar and can be approximated by a log-normal distribution of grain volume (black fit line, see Section 7.2 for details). The same datasets and log-normal grain volume distributions are presented in Fig. 7.1(c) as a volume-weighted distribution of relative grain volume (defined in 7.3), demonstrating again the close approximation of all data by a log-normal distribution with variance  $\sigma_{\text{distr}} = 1.2$ .<sup>3</sup> Assuming that this particular distribution shape faithfully represents polycrystalline aggregates, it can serve as a reference for synthetic datasets to identify systematic deviations relative to it.

Synthetic grain structures were generated by a series of filters using DREAM.3D [134] (see 7.4 for list of filters and [21, 22] for details of the generation process). A log-normal distribution of grain sizes with mean  $\mu_{\text{size}} = 1.0$  and variance  $\sigma_{\text{size}} = 0.4$  was created in the filter ‘StatsGenerator’ and matched well with experimentally observed grain size distributions (Fig. 7.1(b) and (c)). Next, based on the above grain size distribution, two versions of four polycrystals (Fig. 7.2(a)) having grain shapes of either cube octahedra or super ellipsoids were generated with the filter ‘Establish Shape Types’ to investigate the potential influence of shape anisotropy. Invoking the same statistical representation as in Fig. 7.1 demonstrates the close similarity of synthetic and measured structures in terms of their grain volumes (see Fig. 7.2(b) and (c)). In terms of grain shapes, the cube octahedral grain structures are close to equiaxed while the super ellipsoidal ones are generally more elongated as can be inferred from the ratios of maximum to minimum principal moments of inertia, i. e. the “eccentricity,” that are shown cumulatively in Fig. 7.3 (solid lines) from all synthetic grains.

---

<sup>3</sup>Translations between the frames (b) and (c) in Figs. 7.1 and 7.2 make use of the fact that the relative grain volume in (b) is simply given by the slope  $dF_V/dF_N$  since the average grain volume in that frame is  $\langle V \rangle = V_{\text{total}}/N_{\text{grains}} = 1/1 = 1$ , falling along the dotted line in (b).

The volume  $V_{\text{ref}}$  and centroid<sup>4</sup> of every constituting grain ( $N_{\text{grains}} \approx 500$ ) was extracted from each of the eight synthetic polycrystals to serve as a basis for comparing the reconstruction method variations that are presented next.

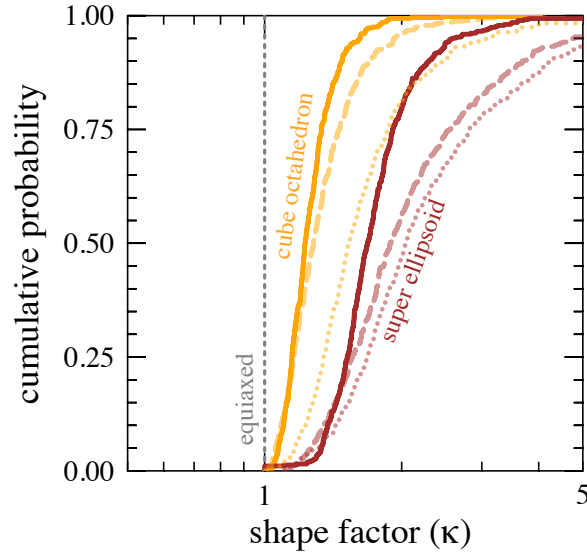


Figure 7.3: Ratio of largest to smallest principal moment of inertia (‘shape factor’) for all cube octahedral (orange) and super ellipsoidal (brown) grains. Solid lines correspond to synthetic (reference) structures shown in Fig. 7.2(a). The fainter curves result after reconstructing the reference structures using either grain volumes (dashed) or centroid distances (dotted) as a basis for Laguerre tessellation weights. In general, cube octahedral grain structures are closer to being equiaxed than those based on super ellipsoids.

#### 7.1.4 Comparison of 3D reconstruction of grain aggregates in presence/absence of grain volume information

Given that the identification of grain centroids is typically more common than determination of the associated grain volumes in far-field HEDM, we investigate how accurately the known (synthetic) polycrystals described in Section 7.1.3 can be reconstructed based solely on centroid information compared to having additional explicit knowledge of grain volumes. For both cases, termed ‘absent’ and ‘present’, the centroids are a natural choice as seed points in a Laguerre tessellation.

<sup>4</sup>spatial average of the positions of all voxels that comprise a grain

The ‘present’ case has already been studied by Lyckegaard et al. [23] with the result that a fairly accurate reconstruction can be achieved when the Laguerre weights are chosen as  $w = (r_{\text{equiv}})^2 = (3V_{\text{ref}}/4\pi)^{2/3}$ , i.e. as the squared equivalent sphere radius of grain volume  $V_{\text{ref}}$ . Furthermore, they observed a slight improvement in accuracy when correcting each seed position by the offset between the initial seed position of each grain and the centroid resulting after a first tessellation.

In the ‘absent’ case, i.e. without explicit knowledge of the correct grain volumes, selection of Laguerre weights is not straightforward. One possible choice, which is used in the present study, is  $w = (d_{\text{nn}})^2$  with  $d_{\text{nn}}$  being the distance between a grain centroid and its nearest neighboring one.

The reconstruction accuracy resulting from both above conditions, i.e. with and without explicit knowledge of the grain volume, is presented in Fig. 7.4 as joint probability density of correct grain volume  $V_{\text{ref}}$  and relative deviation  $V_{\text{tess}}/V_{\text{ref}}$  (outer rows) or  $\kappa_{\text{tess}}/\kappa_{\text{ref}}$  (inner rows) between tessellated and correct volume or shape factor, respectively. In case of Laguerre weights being derived from known grain volume information (‘present’, upper half in Fig. 7.4), most of the reconstructed grains are within about 20 % of the correct volume and show a systematic decrease of reconstruction accuracy with decreasing grain size. The slight reduction in grain volume reconstruction accuracy between more equiaxed (cube octahedral) and less equiaxed (super ellipsoidal) grain shape that is observed in the upper row of Fig. 7.4 is expected since the Laguerre tessellation is isotropic by design, hence, will become increasingly inaccurate with increasing structural anisotropy. Similarly, the reconstruction accuracy in terms of grain shape factor (second row in Fig. 7.4) is higher for the synthetic structures utilizing the more equiaxed cube octahedral grains than for the super ellipsoidal grain shapes. The two-pass correction of seed points suggested by Lyckegaard et al. [23] removes the systematic overprediction of tessellated volumes for the largest grains (compare red to green probability maps). In case of Laguerre weights being derived from

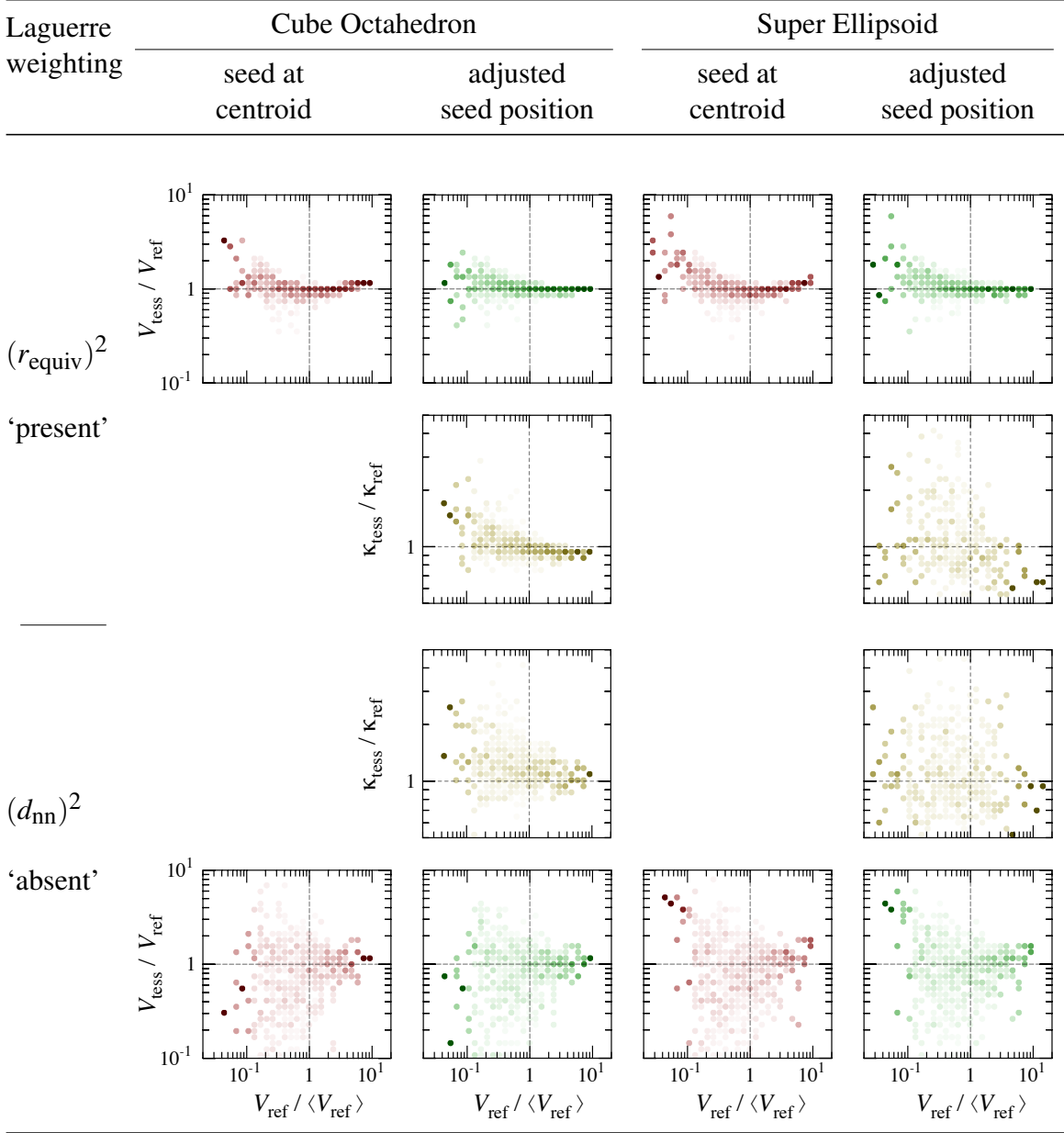


Figure 7.4: Joint probability of correct grain volume (normalized by average grain size) and relative deviation in the reconstructed grain volume  $V_{\text{tess}}/V_{\text{ref}}$  or grain shape factor  $\kappa_{\text{tess}}/\kappa_{\text{ref}}$ . Grain reconstruction uses Laguerre tessellation with grain centroids as seed positions. Seed point weights are derived from known grain volumes (upper half) or estimated from the distance to the nearest grain centroid (lower half). Left and right panels correspond to cube hexahedral and super ellipsoidal grain shapes, respectively, that were used in generating the underlying synthetic data sets (Fig. 7.2(a)). Red maps correspond to direct use of grain centroids as seed positions, while green maps illustrate changes due to a seed position adjustment [23] that considers the new centroid location of each resulting tessellated grain. The comparisons of shape factor deviations (yellow maps) utilized only those latter reconstructed structures.

nearest neighbor distances of centroids (‘absent’, lower half in Fig. 7.4), the overall agreement between correct and tessellated volume is substantially weaker—as will be discussed in connection with Fig. 7.6. Furthermore, the systematic deterioration of accuracy in grain volume as well as grain shape reconstruction with decreasing grain size is much more pronounced in the ‘absent’ case compared to the ‘present’ case.

Given the above established uncertainties of grain volumes reconstructed by Laguerre tessellation with and without knowledge of correct grain volumes, it is informative to determine the associated uncertainty of the grain-averaged lattice strains as margin of error when comparing measurements to simulations. To answer this question, Crystal Plasticity Fast Fourier Transform (CPFFT) simulations were performed, the results of which are reported in next section.

### 7.1.5 Grain averaged lattice strains of reconstructed structures

A finite strain framework is adopted in which the deformation gradient  $\mathbf{F} = \mathbf{F}_e \mathbf{F}_p$  at each material point is multiplicatively decomposed into elastic  $\mathbf{F}_e$  and plastic  $\mathbf{F}_p$  components, thus introducing an intermediate (or ‘lattice’) configuration. The second PIOLA–KIRCHHOFF stress  $\mathbf{S} = \mathbb{C} : (\mathbf{F}_e^T \mathbf{F}_e) / 2 = f(\dot{\mathbf{F}}, \boldsymbol{\eta})$  reflects the elastic lattice distortion ( $\mathbb{C}$  being the fourth-order elastic stiffness tensor) and drives the plastic velocity gradient  $\mathbf{L}_p(\mathbf{S}, \boldsymbol{\eta}) = \dot{\mathbf{F}}_p \mathbf{F}_p^{-1}$  as well as the evolution of internal state variables  $\boldsymbol{\eta}$  (see [76] for details).

The constitutive model used in the present study is similar to the phenomenological description of Peirce et al. [1] for cubic lattice symmetry. The internal state is captured through slip resistances  $\tau_0$  per slip system  $\xi$ , which evolve with shear  $\gamma$  according to a relationship initially proposed by

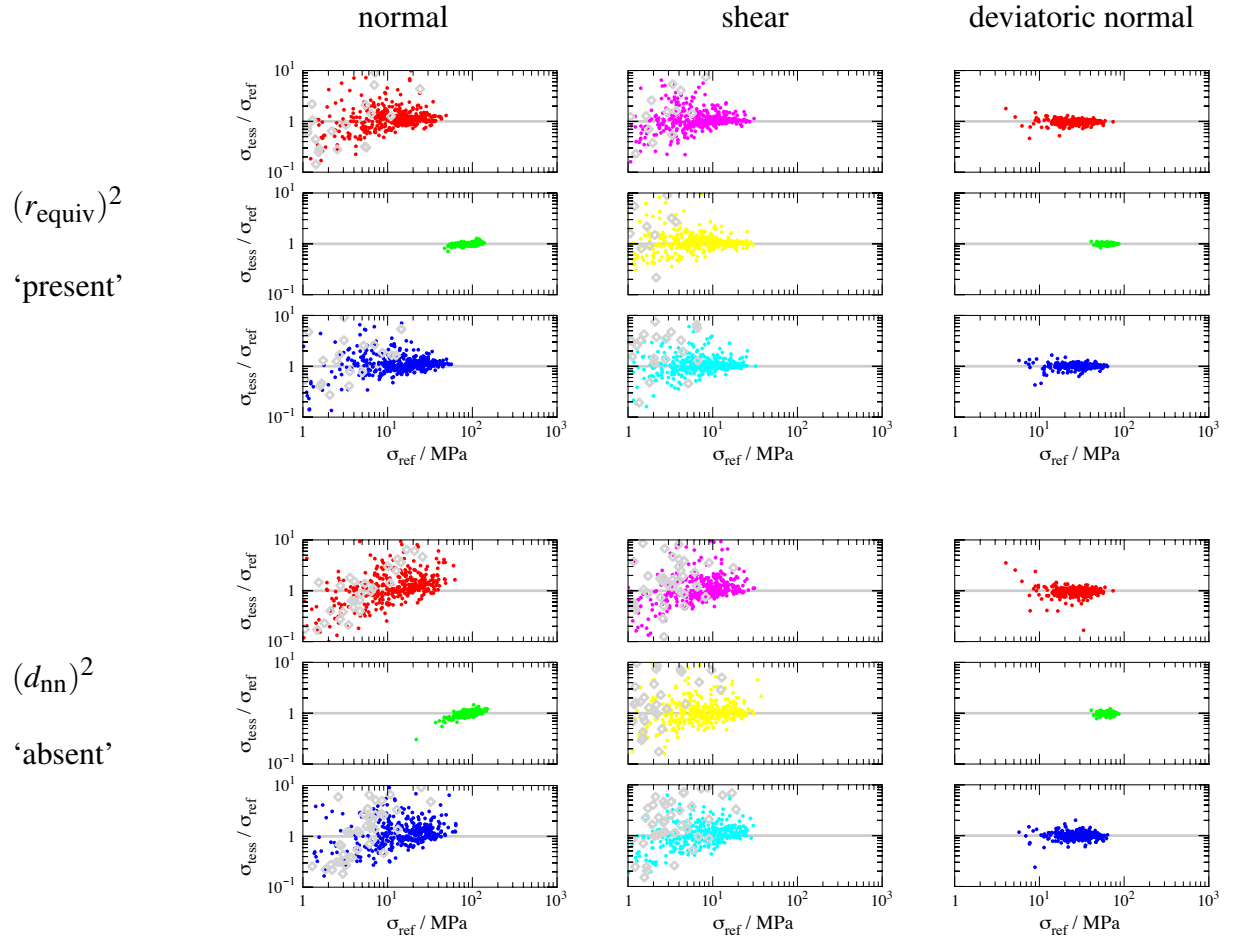


Figure 7.5: Deviations of normal, shear, and deviatoric normal components of grain-averaged Cauchy stress  $\sigma_{\text{tess}}$  in reconstructed grain structures relative to corresponding stress components  $\sigma_{\text{ref}}$  resulting in the (cube octahedron) reference grain structures. Tessellations in upper panel employ known grain volume information ( $r_{\text{equiv}}$ ) for Laguerre weights, while in lower panel the nearest centroid distances ( $d_{\text{nn}}$ ) are used instead. The seed positions were adjusted [23] in both tessellation alternatives.

Hutchinson [98] and later improved by Kalidindi et al. [99]

$$\dot{g}^{\xi} = q_{\xi\beta} h_0 \left( 1 - \frac{\tau_0^{\beta}}{g_{\infty}^{\beta}} \right)^a |\dot{\gamma}^{\beta}|. \quad (7.2)$$

The slip system interactions are controlled by the hardening matrix  $q_{\xi\beta}$ . The shear rate on each

Table 7.1: Material parameters; elastic constants  $C_{ab}$ , reference shear rate  $\dot{\gamma}_0$ , stress exponent  $n$ , initial and saturation slip resistance  $\tau_0$  and  $g_\infty$ , hardening parameters  $h_0, q_{\xi\beta}$ , and  $a$ .

Parameter	Value	Unit
$C_{11}$	106.75	GPa
$C_{12}$	60.41	GPa
$C_{44}$	28.34	GPa
$\dot{\gamma}_0$	$10^{-3}$	$s^{-1}$
$n$	20	
$\tau_0$	31	MPa
$g_\infty$	63	MPa
$a$	2.25	
$h_0$	75	MPa
Coplanar $q_{\xi\beta}$	1	
Non-coplanar $q_{\xi\beta}$	1.4	

system is given by

$$\dot{\gamma}^\xi = \dot{\gamma}_0 \left| \frac{\tau^\xi}{g_\infty^\xi} \right|^n \text{sign } \tau^\xi, \quad (7.3)$$

where  $\dot{\gamma}_0$  is a reference shear rate,  $n$  the stress exponent, and  $\tau^\xi = \mathbf{S} : (\mathbf{m}^\xi \otimes \mathbf{n}^\xi)$  the resolved shear stress. The plastic velocity gradient

$$\mathbf{L}_p = \dot{\gamma}^\xi \mathbf{m}^\xi \otimes \mathbf{n}^\xi \quad (7.4)$$

is additively composed from all shear rates, where  $\mathbf{m}^\xi$  and  $\mathbf{n}^\xi$  are unit vectors along the slip direction and slip plane normal, respectively. Table 7.1 summarizes the adjustable parameters used to mimic a material similar to aluminum.

For the periodic structures investigated in this study, spectral methods are an efficient alternative to the finite element method (FEM) for solving the mechanical boundary value problem of static equilibrium [135, 136, 137, 80, 82]. Here, we employ a finite strain spectral solver developed by Eisenlohr et al. [82] and Shanthraj et al. [88] that includes a flexible material point model

(DAMASK) to incorporate the constitutive law described above. All (periodic) grain aggregates are discretized on a regular  $100 \times 100 \times 100$  grid.

Due to the periodic nature of the geometry, boundary conditions for simulating the chosen reference case of uniaxial tension along the  $y$ -direction have to be specified as volume-averaged deformation gradient rate and complementary (first PIOLA–KIRCHHOFF) stress

$$\frac{\langle \dot{\mathbf{F}} \rangle}{10^{-3} \text{ s}^{-1}} = \begin{bmatrix} * & 0 & 0 \\ 0 & 1 & 0 \\ 0 & 0 & * \end{bmatrix} \quad \text{and} \quad \frac{\langle \mathbf{P} \rangle}{\text{Pa}} = \begin{bmatrix} 0 & * & * \\ * & * & * \\ * & * & 0 \end{bmatrix}, \quad (7.5)$$

with ‘\*’ indicating mixed boundary conditions, where either stress (or deformation) is prescribed so that deformation (or stress) needs to be iteratively adjusted. In the simulations, above conditions are maintained during 100 increments of 1 s each (such that the final  $\langle F \rangle_{yy} = 1.1$ ).

To elucidate the influence of reconstruction quality on the average lattice strain predicted from crystal plasticity simulations of grain aggregates, the four synthetic grain aggregate geometries that are based on cube octahedral grain shapes were selected as reference. The above specified deformation was simulated for those references as well as for the associated two (seed corrected) reconstruction alternatives, where one tessellation utilizes grain volume information, the other estimating it from nearest centroid distances (termed ‘present’ and ‘absent’ case).

Figure 7.5 compares for both tessellation cases (upper and lower panel) the relative deviation of average Cauchy stress in each reconstructed grain from its reference result. The relative deviations observed for the same stress component are very similar for both cases. For both reconstructed structures, the (green) normal stress component along the loading direction agrees very closely to that found in the respective reference structure. The magnitude of the other two normal stress components as well as of the three shear stress components is in general substantially lower than

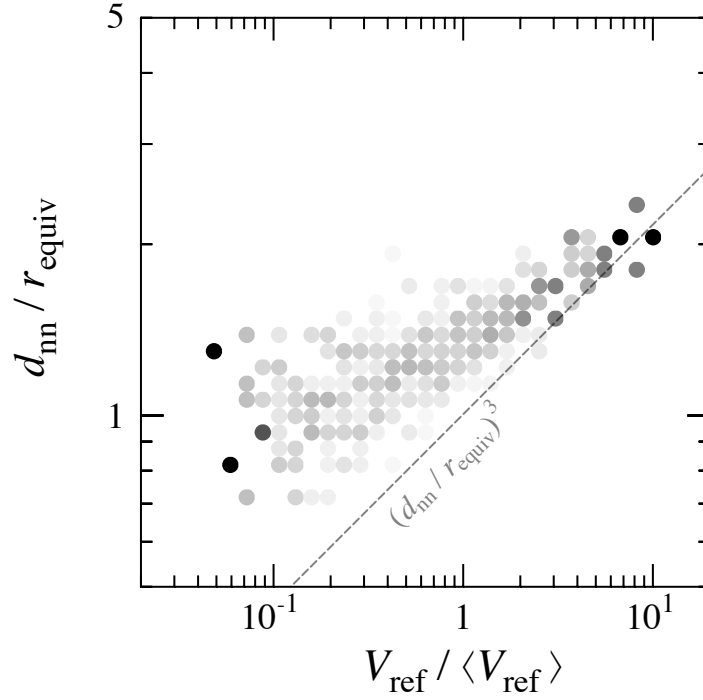


Figure 7.6: Joint probability of volume  $V_{\text{ref}}$  of synthetic grains and the distance  $d_{\text{nn}}$  from each grain centroid to the nearest neighboring one. Quantities are normalized by the average grain volume  $\langle V_{\text{ref}} \rangle$  and its equivalent radius  $r_{\text{equiv}} = (3\langle V_{\text{ref}} \rangle / 4\pi)^{1/3}$ , respectively. Cumulative probability is scaled to unity within each (vertical) bin of normalized grain volume. Centroid distance progressively deviates from expected relation (dashed line) with decreasing volume of grain, resulting in a weak correlation between the distance to the nearest grain centroid and the volume of a grain.

the normal stress observed along the loading direction. The deviations of these five components progressively increase with decreasing (reference) stress magnitudes, i.e., they fan out toward the left, occasionally even resulting in a reversal of sign (illustrated by open diamonds in Fig. 7.5). The rightmost column in Fig. 7.5 shows the relative deviation of *deviatoric* normal components, i.e., excluding the mean stress  $\sigma_{\text{sph}} = (\sigma_{11} + \sigma_{22} + \sigma_{33})/3$ . In contrast to the normal stress components shown in the leftmost column, the relative deviation of the deviatoric normal components is markedly reduced and essentially independent of the magnitude of reference deviatoric stress.

### 7.1.6 Discussion

As shown in Fig. 7.4, the uncertainty in the volume of a reconstructed grain is much larger when the tessellation is estimating the Laguerre weights from nearest centroid distances compared to when directly using the known reference volumes. This increased uncertainty can be connected to the weak correlation found between the volume of a grain and its distance  $d_{nn}$  to the nearest neighboring grain centroid, which is illustrated in Fig. 7.6. For a given  $d_{nn}$ , the potential grain volume associated with that distance falls into a range of about a factor of three for the relatively large grains (right end of Fig. 7.6), while for the relatively small grains (left end) this range increases to about an order of magnitude. This increasing uncertainty is caused by the progressive deviation with decreasing grain size of the most likely nearest neighbor distances toward values above the natural correlation  $V_{\text{ref}}^{1/3} \propto d_{nn}$  (dashed line in Fig. 7.6). Since small grains are likely to be situated in a neighborhood of larger grains, the distance to the centroid of their nearest neighboring grain is frequently unrelated to and far larger than its own equivalent radius. Such a disconnect is less probable for a relatively large grain since, for many conceivable neighborhoods, the closest centroid distance is primarily determined by the size of the large grain itself.

Although a sizable difference emerged in the quality of reconstruction between grain structures tessellated with the Laguerre weights either derived from grain volumes or estimated from nearest centroid distances (see Fig. 7.4), under the uniaxial loading applied in the present study, both tessellated grain structures show very similar deviations from the reference structure in terms of observed lattice strains (i.e. stress). Figure 7.7 collects deviations across all six Cauchy stress components from both tessellations in a joint probability plot. The observed increase in *relative* deviations (uncertainty) with decreasing (reference) stress magnitude is compatible with an *absolute* uncertainty

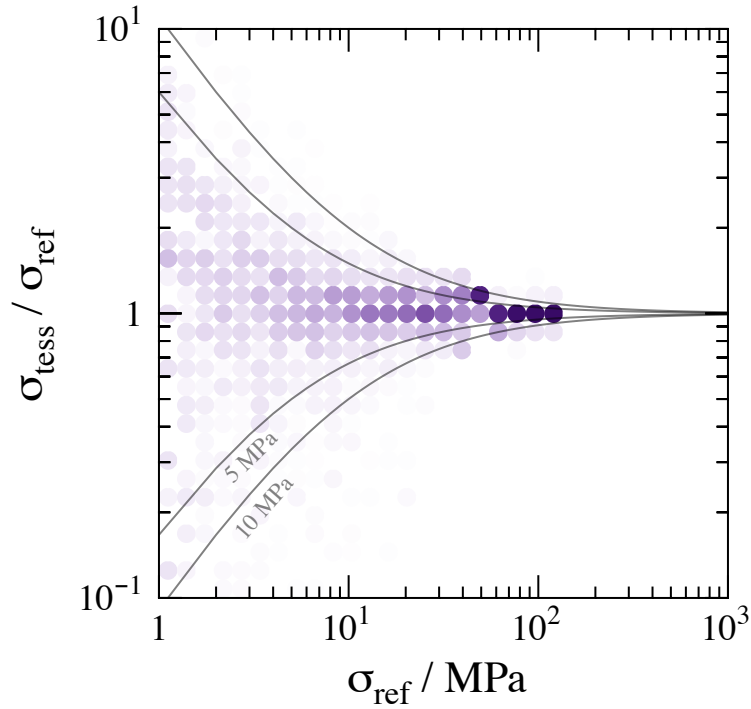


Figure 7.7: Joint probability of stress magnitudes  $\sigma_{\text{ref}}$  in reference structure and relative deviations  $\sigma_{\text{tess}}/\sigma_{\text{ref}}$  combined from both tessellated structures. Cumulative probability is scaled to unity within each bin of stress magnitudes. Solid lines exemplify relative deviations in stress due to absolute differences of 5 MPa and 10 MPa. With increase in magnitude of stress, the relative deviations in stress due to difference in grain morphologies diminishes.

in the range of 5 MPa to 10 MPa as illustrated by the solid lines in Fig. 7.7. The apparently much closer agreement between deviatoric normal stress components (Fig. 7.5 right) compared to the normal stress components containing hydrostatic stress (Fig. 7.5 left) can be rationalized with a similar argument. The deviatoric stress projection results in an overall shift to absolutely larger values for the two transverse stress components ( $xx$  and  $zz$ , red and blue in Fig. 7.5). Therefore, the large relative deviations observed at small stress magnitudes tend to shrink when considered at larger stress magnitudes.

## 7.2 Cumulative volume fraction of log-normal grain size distributions

Assuming individual grain volumes in a polycrystal to follow a log-normal distribution, their cumulative number fraction  $F_N$  as function of grain volume  $V_{\text{grain}}$  is given by

$$F_N = \frac{1}{2} \left( 1 + \operatorname{erf} \left[ \frac{\ln V_{\text{grain}}/\mu}{\sqrt{2}\sigma} \right] \right) \quad (7.6)$$

and the average grain volume is

$$\langle V \rangle = \mu \exp \left( \frac{\sigma^2}{2} \right). \quad (7.7)$$

Therefore, the relative grain volume corresponding to a particular cumulative number fraction follows as

$$\frac{V_{\text{grain}}}{\langle V \rangle} = \exp \left( \sqrt{2}\sigma \operatorname{erf}^{-1} [2F_N - 1] - \frac{\sigma^2}{2} \right). \quad (7.8)$$

The relation between cumulative volume fraction  $F_V$  and cumulative number fraction is established by integration of Eq. (7.8), yielding

$$F_V = \frac{1}{2} \operatorname{erfc} \left[ \frac{\sigma}{\sqrt{2}} - \operatorname{erf}^{-1} [2F_N - 1] \right]. \quad (7.9)$$

Conveniently, Eq. (7.9) does not depend on the actual grain volume magnitudes but only on the shape of their distribution, which is governed by the variance  $\sigma_{\text{distr}}$  as illustrated by the sequence of gray curves in Fig. 7.1.

## 7.3 Grain size normalization

The ‘relative grain volume’ of each grain in a population of  $N_{\text{grains}}$  occupying an overall volume  $V_{\text{total}}$  (typically counted in voxels) is defined as the grain volume,  $V_{\text{grain}}$ , normalized by the average grain volume:

$$V_{\text{rel}} = \frac{V_{\text{grain}}}{\langle V \rangle} = \frac{V_{\text{grain}}}{V_{\text{total}}} N_{\text{grains}}. \quad (7.10)$$

The cumulative volume fraction as a function of relative grain volume can then be used to compare different grain populations on the same scale.

## 7.4 Generation of synthetic grain structures

The pipeline listed in 7.2 is used to generate the synthetic structures shown in Fig. 7.2(a). A log-normal grain size distribution with mean  $\mu_{\text{size}} = 1.0$  and variance  $\sigma_{\text{size}} = 0.4$  created by ‘StatsGenerator’ was packed into the synthetic volume using grain shape types of either ‘cube octahedron’ or ‘super ellipsoid’.

Table 7.2: DREAM.3D pipeline for generating synthetic grain structures.

<b>Filter order</b>	<b>Filter name</b>
1	StatsGenerator
2	Initialize Synthetic Volume
3	Establish Shape Types
4	Pack Primary Phases
5	Write Output

## **BIBLIOGRAPHY**

## BIBLIOGRAPHY

- [1] D. Peirce, R. J. Asaro, and A. Needleman. An analysis of nonuniform and localized deformation in ductile single crystals. *Acta Metallurgica*, 30(6):1087–1119, 1982.
- [2] S. Queyreau, G. Monnet, and B. Devincere. Slip systems interactions in alpha-iron determined by dislocation dynamics simulations. *International Journal of Plasticity*, 25(2):361–377, 2009.
- [3] R. Madec and L. P. Kubin. Dislocation strengthening in FCC metals and in BCC metals at high temperatures. *Acta Materialia*, 126:166–173, 2017.
- [4] P. Franciosi. Glide mechanisms in b.c.c. crystals: an investigation of the case of  $\alpha$ -iron through multislip and latent hardening tests. *Acta Metallurgica*, 31(9):1331–1342, 1983.
- [5] W. A. Spitzig and A. S. Keh. The effect of orientation and temperature on the plastic flow properties of iron single crystals. *Acta Metallurgica*, 18(6):611–622, 1970.
- [6] A. S. Keh and Y. Nakada. Plasticity of iron single crystals. *Canadian Journal of Physics*, 45(2):1101–1120, 1967.
- [7] J. Kumagai, S. Takaki, S. Suzuki, and H. Kimura. Orientation dependence of quasi-three-stage work hardening in high purity iron single crystals. *Materials Science and Engineering: A*, 129(2):207–215, 1990.
- [8] P. B. Jaoul and D. Gonzalez. Deformation plastique de monocristaux de fer. *Journal of the Mechanics and Physics of Solids*, 9(1):16–38, 1961.
- [9] A. S. Keh. Work hardening and deformation sub-structure in iron single crystals deformed in tension at 298 K. *Philosophical Magazine*, 12(115):9–30, 1965.
- [10] M. S. Duesbery and R. A. Foxall. A detailed study of the deformation of high purity niobium single crystals. *Philosophical Magazine*, 20(166):719–751, 1969.
- [11] A. Seeger and W. Wasserbach. Anomalous Slip – A Feature of High-Purity Body-Centred Cubic Metals. *physica status solidi (a)*, 189(1):27–50, 2002.
- [12] D. C. Baars. *Investigation of active slip systems in high purity single crystal niobium*. PhD thesis, 2013.
- [13] F. Roters, P. Eisenlohr, T. R. Bieler, and D. Raabe. *Crystal Plasticity Finite Element Methods*

*in Materials Science and Engineering*. Wiley-VCH, Weinheim, 2010.

- [14] Z. Zhao, M. Ramesh, D. Raabe, A. M. Cuitiño, and R. Radovitzky. Investigation of three-dimensional aspects of grain-scale plastic surface deformation of an aluminum oligocrystal. *International Journal of Plasticity*, 24:2278–2297, 2008.
- [15] A. Chakraborty and P. Eisenlohr. Evaluation of an inverse methodology for estimating constitutive parameters in face-centered cubic materials from single crystal indentations. *European Journal of Mechanics / A Solids*, 66C:114–124, 2017.
- [16] B. Devincre, T. Hoc, and L. Kubin. Dislocation Mean Free Paths and Strain Hardening of Crystals. *Science*, 320(5884):1745–1748, 2008.
- [17] W. Ludwig, P. Reischig, A. King, M. Herbig, E. M. Lauridsen, G. Johnson, T. J. Marrow, and J. Y. Buffière. Three-dimensional grain mapping by x-ray diffraction contrast tomography and the use of Friedel pairs in diffraction data analysis. *Review of Scientific Instruments*, 80(3):033905, 2009.
- [18] W. Ludwig, A. King, P. Reischig, M. Herbig, E. M. Lauridsen, S. Schmidt, H. Proudhon, S. Forest, P. Cloetens, S. R. Du Roscoat, J. Y. Buffière, T. J. Marrow, and H. F. Poulsen. New opportunities for 3D materials science of polycrystalline materials at the micrometre lengthscale by combined use of X-ray diffraction and X-ray imaging. *Materials Science and Engineering: A*, 524(1-2):69–76, 2009.
- [19] R. Pokharel, J. Lind, S. F. Li, P. Kenesei, R. A. Lebensohn, R. M. Suter, and A. D. Rollett. In-situ observation of bulk 3D grain evolution during plastic deformation in polycrystalline Cu. *International Journal of Plasticity*, 67:217–234, 2015.
- [20] P. A. Shade, M. A. Groeber, J. C. Schuren, and M. D. Uchic. Experimental measurement of surface strains and local lattice rotations combined with 3D microstructure reconstruction from deformed polycrystalline ensembles at the micro-scale. *Integrating Materials and Manufacturing Innovation*, 2(1):5, 2013.
- [21] M. Groeber, S. Ghosh, M. D. Uchic, and D. M. Dimiduk. A framework for automated analysis and simulation of 3D polycrystalline microstructures. Part 1: Statistical characterization. *Acta Materialia*, 56(6):1257–1273, 2008.
- [22] M. Groeber, S. Ghosh, M. D. Uchic, and D. M. Dimiduk. A framework for automated analysis and simulation of 3D polycrystalline microstructures. Part 2: Synthetic structure generation. *Acta Materialia*, 56(6):1274–1287, 2008.
- [23] A. Lyckegaard, E. M. Lauridsen, W. Ludwig, R. W. Fonda, and H. F. Poulsen. On the Use of Laguerre Tessellations for Representations of 3D Grain Structures. *Advanced Engineering*

- Materials*, 13(3):165–170, 2011.
- [24] H. and Padamsee, editor. *Proceedings of the 1st TESLA Workshop*. 1990.
- [25] Proceedings of International Workshop on Next-Generation Linear Colliders. Technical report, 1988.
- [26] M. Hein. *High-Temperature-Superconductor Thin Films at Microwave Frequencies*. Springer Berlin Heidelberg, Berlin, Heidelberg, 1999.
- [27] Y. Wang, T. Plackowski, and A. Junod. Specific heat in the superconducting and normal state (2-300 K, 0-16 T), and magnetic susceptibility of the 38 K superconductor MgB<sub>2</sub>: evidence for a multicomponent gap. *Physica C: Superconductivity*, 355(3-4):179–193, 2001.
- [28] X. X. Xi, A. V. Pogrebnyakov, S. Y. Xu, K. Chen, Y. Cui, E. C. Maertz, C. G. Zhuang, Q. Li, D. R. Lamborn, J. M. Redwing, Z. K. Liu, A. Soukiassian, D. G. Schlom, X. J. Weng, E. C. Dickey, Y. B. Chen, W. Tian, X. Q. Pan, S. A. Cybart, and R. C. Dynes. MgB<sub>2</sub> thin films by hybrid physical-chemical vapor deposition. *Physica C: Superconductivity*, 456(1-2):22–37, 2007.
- [29] D. E. Oates, A. C. Anderson, C. C. Chin, J. S. Derov, G. Dresselhaus, and M. S. Dresselhaus. Surface-impedance measurements of superconducting NbN films. *Physical Review B*, 43(10):7655–7663, 1991.
- [30] B. W. Maxfield and W. L. McLean. Superconducting Penetration Depth of Niobium. *Physical Review*, 139(5a):A1515–A1522, 1965.
- [31] H. Stuart. *Niobium: Proceedings of the International Symposium*. Metallurgical Society of AIME, Warrendale, Pa., 1984.
- [32] P. Dhakal, G. Ciovati, P. Kneisel, and G. R. Myneni. Enhancement in Quality Factor of SRF Niobium Cavities by Material Diffusion. *IEEE Transactions on Applied Superconductivity*, 25(3):1–4, 2015.
- [33] T. R. Bieler, N. T. Wright, F. Pourboghrat, C. Compton, K. T. Hartwig, D. Baars, A. Zamiri, S. Chandrasekaran, P. Darbandi, H. Jiang, E. Skoug, S. Balachandran, G. E. Ice, and W. Liu. Physical and mechanical metallurgy of high purity Nb for accelerator cavities. *Physical Review Special Topics – Accelerators and Beams*, 13(3):031002, 2010.
- [34] *FRIB SRF Cavities*, 2012. 7th SRF Materials Workshop.
- [35] *Ingot niobium – the Choice Materials for Future SRF Cavity Applications?*, 2012. 7th SRF Materials Workshop.

- [36] A. Mapar, D. Kang, T. R. Bieler, F. Pourboghrat, and C. C. Compton. Refining Crystal Plasticity Finite Element Model for Deformation of Single Crystal Niobium. In *7th SRF Materials Workshop*, 2012.
- [37] *Overview of cavity requirements for high intensity and high energy*, 2012. 7th SRF Materials Workshop.
- [38] H. Padamsee. *RF Superconductivity*. Wiley-VCH Verlag GmbH & Co. KGaA, Weinheim, Germany, 2009.
- [39] J. Knoblock. Field emission and thermal breakdown in superconducting niobium cavities for accelerators. *IEEE Transactions on Applied Superconductivity*, 9(2):1016–1022, 1999.
- [40] E. Schmid and W. Boas. *Kristallplastizität*. Springer Berlin Heidelberg, Berlin, Heidelberg, 1935.
- [41] G. I. Taylor and C. F. Elam. The Distortion of Iron Crystals. *Proceedings of the Royal Society A: Mathematical, Physical and Engineering Sciences*, 112(761):337–361, 1926.
- [42] H. Gough. The Behaviour of a Single Crystal of Iron Subjected to Alternating Torsional Stresses. *Proceedings of the Royal Society A: Mathematical, Physical and Engineering Sciences*, 118(780):498–534, 1928.
- [43] W. Fahrenhorst and E. Schmid. Über die plastische Dehnung von  $\alpha$ -Eisenkristallen. *Zeitschrift für Physik*, 78(5-6):383–394, 1932.
- [44] J. J. Cox, G. T. Horne, and R. F. Mehl. *Trans ASM*, 49:118, 1956.
- [45] H. Bilger. On the recovery of plastically deformed iron single crystals above room temperature. *physica status solidi (b)*, 18(2):K135–K138, 1966.
- [46] Jr F. L. Vogel and R. M. Brick. *J. Metall AIME*, page 700, 1953.
- [47] A. Seeger. Why anomalous slip in body-centered cubic metals? *Materials Science and Engineering A*, 319-321:254–260, 2001.
- [48] J. R. Low Jr. and A. M. Turkalo. Slip band structure and dislocation multiplication in silicon-iron crystals. *Acta Metallurgica*, 10(3):215–227, 1962.
- [49] T. Taoka, S. Takeuchi, and E. Furubayashi. Slip Systems and Their Critical Shear Stress in 3% Silicon Iron. *Journal of the Physical Society of Japan*, 19(5):701–711, 1964.
- [50] S. Takeuchi, E. Furubayashi, and T. Taoka. Orientation dependence of yield stress in 4.4%

- silicon iron single crystals. *Acta Metallurgica*, 15(7):1179–1191, 1967.
- [51] F. E. Neumann. *Vorlesungen über die Theorie der Elastizität der festen Körper und des Lichtäthers*. B. G. Teubner-Verlag, Leipzig, 1885.
- [52] J. W. Christian. Some Surprising Features of the Plastic Deformation of the Body-Centered Cubic Metals and Alloys. *Metallurgical Transactions A*, 14:1237–1256, 1983.
- [53] M. S. Duesbery. volume 8 of *Dislocations in Solids*, chapter The dislocation core and plasticity, pages 67–173. Elsevier, Amsterdam, 1989.
- [54] V. Vitek. Theory of the core structures of dislocations in bcc metals. *Crystal Lattice Defects*, 5:1, 1974.
- [55] Q. Qin and J. L. Bassani. Non-schmid yield behavior in single crystals. *Journal of the Mechanics and Physics of Solids*, 40(4):813–833, 1992.
- [56] B. Escaig. Sur le glissement dévié des dislocations dans la structure cubique a faces centrées. *Journal de Physique*, 29(2-3):225–239, 1968.
- [57] B. Escaig. Dissociation And Mechanical Properties. Dislocation Splitting And The Plastic Glide Process In Crystals. *Le Journal de Physique Colloques*, 35(C7):C7–151–C7–166, 1974.
- [58] J. Bonneville and B. Escaig. Cross-slipping process and the stress-orientation dependence in pure copper. *Acta Metallurgica*, 27(9):1477–1486, 1979.
- [59] E-Ichi Furubayashi. Behavior of Dislocations in Fe-3% Si under Stress. *Journal of the Physical Society of Japan*, 27(1):130–146, 1969.
- [60] F. Louchet, L. P. Kubin, and D. Vesely. In situ deformation of b.c.c. crystals at low temperatures in a high-voltage electron microscope Dislocation mechanisms and strain-rate equation. *Philosophical Magazine A*, 39(4):433–454, 1979.
- [61] T. Imura. In M. Meshii, editor, *Proc. US-Japan Symp. Mechanical Properties of BCC Metals*, pages 65–73, Warrendale, PA, 1982. TMS-AIME.
- [62] A. Seeger. Progress and problems in the understanding of the dislocation relaxation processes in metals. *Materials Science and Engineering: A*, 370(1-2):50–66, 2004.
- [63] R. A. Foxall and C. D. Statham. Dislocation arrangements in deformed single crystals of niobium-molybdenum alloys and niobium-9 at.% rhenium. *Acta Metallurgica*, 18(11):1147–1158, 1970.

- [64] J. P. Hirth and J. Lothe. *Theory of dislocations*. John Wiley & Sons, New York, 1982.
- [65] R. Peierls. The size of a dislocation. *Proceedings of the Physical Society*, 52(1):34–37, 2002.
- [66] J-Y Kim, D. Jang, and J. R. Greer. Insight into the deformation behavior of niobium single crystals under uniaxial compression and tension at the nanoscale. *Scripta Materialia*, 61(3): 300–303, 2009.
- [67] R. Peierls. The size of a dislocation. *Proceedings of the Physical Society*, 52:34–37, 1940.
- [68] A. Seeger. Peierls barriers, kinks, and flow stress: Recent progress. *Zeitschrift für Metallkunde*, 93:760–777, 2002.
- [69] L. Hollang, M. Hommel, and A. Seeger. The Flow Stress of Ultra-High-Purity Molybdenum Single Crystals. *physica status solidi (a)*, 160(2):329–354, 1997.
- [70] F. Ackermann, H. Mughrabi, and A. Seeger. Temperature- and strain-rate dependence of the flow stress of ultrapure niobium single crystals in cyclic deformation. *Acta Metallurgica*, 31(9):1353–1366, 1983.
- [71] T. E. Mitchell, R. A. Foxall, and P. B. Hirsch. Work-hardening in niobium single crystals. *Philosophical Magazine*, 8(95):1895–1920, 1963.
- [72] E. Votava. Eine neue Methode zur Herstellung verformungsfreier Einkristall-Zugproben hochschmelzender Metalle und einige Ergebnisse über die plastische Deformation von Niob-Einkristallen. *physica status solidi (b)*, 5(2):421–434, 1964.
- [73] G. Taylor and J. W. Christian. The effect of high vacuum purification on the mechanical properties of niobium single crystals. *Acta Metallurgica*, 13(11):1216–1218, 1965.
- [74] M. S. Duesbery, R. A. Foxall, and P. B. Hirsch. The Plasticity Of Pure Niobium Single Crystals. *Le Journal de Physique Colloques*, 27(C3):C3–193–C3–204, 1966.
- [75] D. Kang, D. C. Baars, T. R. Bieler, and C. Compton. Study of Slip in High Purity Single Crystal Nb for Accelerator Cavities. In C. Antoine, S. Bousson, and G. Martinet, editors, *Proceedings of SRF 2013*, pages 461–465. JACoW, 2014.
- [76] F. Roters, P. Eisenlohr, L. Hantcherli, D. D. Tjahjanto, T. R. Bieler, and D. Raabe. Overview of constitutive laws, kinematics, homogenization, and multiscale methods in crystal plasticity finite element modeling: Theory, experiments, applications. *Acta Materialia*, 58:1152–1211, 2010.

- [77] E. H. Lee. Elastic-plastic deformation at finite strains. *J. Appl. Mech. ASME*, 36(1):1–6, 1969.
- [78] F. Roters, P. Eisenlohr, C. Kords, D. D. Tjahjanto, M. Diehl, and D. Raabe. DAMASK: The Düsseldorf Advanced Material Simulation Kit for studying crystal plasticity using an FE based or a spectral numerical solver. In O. Cazacu, editor, *Procedia IUTAM: IUTAM Symposium on Linking Scales in Computation: From Microstructure to Macroscale Properties*, volume 3, pages 3–10, Amsterdam, 2012. Elsevier.
- [79] P. Eisenlohr, F. Roters, M. Diehl, C. Kords, and P. Shanthraj. DAMASK Web page. 2014.
- [80] A. Prakash and R. A. Lebensohn. Simulation of micromechanical behavior of polycrystals: finite elements versus fast Fourier transforms. *Modelling and Simulation in Materials Science and Engineering*, 17:064010–64016, 2009.
- [81] B. Liu, D. Raabe, F. Roters, P. Eisenlohr, and R. A. Lebensohn. Comparison of finite element and fast Fourier transform crystal plasticity solvers for texture prediction. *Modelling and Simulation in Materials Science and Engineering*, 18(8):085005, 2010.
- [82] P. Eisenlohr, M. Diehl, R. A. Lebensohn, and F. Roters. A spectral method solution to crystal elasto-viscoplasticity at finite strains. *International Journal of Plasticity*, 46:37–53, 2013.
- [83] A. K. Kanjarla, R. A. Lebensohn, L. Balogh, and C. N. Tomé. Study of internal lattice strain distributions in stainless steel using a full-field elasto-viscoplastic formulation based on fast Fourier transforms. *Acta Materialia*, 60(6-7):3094–3106, 2012.
- [84] M. Montagnat, O. Castelnau, P. D. Bons, S. H. Faria, O. Gagliardini, F. Gillet-Chaulet, F. Grennerat, A. Griera, R. A. Lebensohn, H. Moulinec, J. Roessiger, and P. Suquet. Multi-scale modeling of ice deformation behavior. *Journal of Structural Geology*, 2013.
- [85] D. Ma, P. Eisenlohr, E. Epler, C. A. Volkert, P. Shanthraj, M. Diehl, F. Roters, and D. Raabe. Crystal plasticity study of monocrystalline stochastic honeycombs under in-plane compression. *Acta Materialia*, 103:796–808, 2016.
- [86] S. L. Wong, M. Madivala, U. Prahl, F. Roters, and D. Raabe. A crystal plasticity model for twinning- and transformation-induced plasticity. *Acta Materialia*, 118:140–151, 2016.
- [87] N. Lahellec, J. C. Michel, H. Moulinec, and P. Suquet. Analysis of inhomogeneous materials at large strains using fast Fourier transforms. In C. Miehe, editor, *IUTAM Symposium on Computational Mechanics of Solid Materials at Large Strains*, volume 108 of *Solid Mechanics and its Applications*, pages 247–258, Dordrecht, The Netherlands, 2001. Kluwer Academic Publishers.

- [88] P. Shanthraj, P. Eisenlohr, M. Diehl, and F. Roters. Numerically robust spectral methods for crystal plasticity simulations of heterogeneous materials. *International Journal of Plasticity*, 66:31–45, 2015.
- [89] M. Schneider and M. Kabel. The Lipmann-Schwinger equation in elasticity for porous media. In *The Mechanics of Multifunctional Materials*, pages 79–82, 2014.
- [90] R. A. Lebensohn, J. P. Escobedo, E. K. Cerreta, D. Dennis-Koller, C. A. Bronkhorst, and J. F. Bingert. Modeling void growth in polycrystalline materials. *Acta Materialia*, 61(18):6918–6932, 2013.
- [91] R. A. Lebensohn and R. Pokharel. Interpretation of Microstructural Effects on Porosity Evolution Using a Combined Dilatational/Crystal Plasticity Computational Approach. *JOM*, 66(3):437–443, 2014.
- [92] R. Pokharel, J. Lind, A. K. Kanjarla, R. A. Lebensohn, S. F. Li, P. Kenesei, R. M. Suter, and A. D. Rollett. Polycrystal Plasticity: Comparison Between Grain-Scale Observations of Deformation and Simulations. *Annual Review of Condensed Matter Physics*, 5(1):317–346, 2014.
- [93] D. D. Tjahjanto, S. Turteltaub, and A. S. J. Suiker. Crystallographically based model for transformation-induced plasticity in multiphase carbon steels. *Continuum Mechanics and Thermodynamics*, 19(7):399–422, 2008.
- [94] P. Shanthraj, B. Svendsen, L. Sharma, F. Roters, and D. Raabe. Elasto-viscoplastic phase field modelling of anisotropic cleavage fracture. *Journal of the Mechanics and Physics of Solids*, 99:19–34, 2017.
- [95] D. Peirce, R. J. Asaro, and A. Needleman. Material rate dependence and localized deformation in crystalline solids. *Acta Metallurgica*, 31(12):1951–1976, 1983.
- [96] D. Raabe, M. Sachtleber, Z. Zhao, F. Roters, and S. Zaefferer. Micromechanical and macromechanical effects in grain scale polycrystal plasticity experimentation and simulation. *Acta Materialia*, 49(17):3433–3441, 2001.
- [97] M. Diehl. A spectral method using fast Fourier transform to solve elastoviscoplastic mechanical boundary value problems. Master’s thesis, München, 2010.
- [98] J. W. Hutchinson. Bounds and self-consistent estimates for creep of polycrystalline materials. *Proceedings of the Royal Society A*, 348:101–127, 1976.
- [99] S. R. Kalidindi, C. A. Bronkhorst, and L. Anand. Crystallographic texture evolution in bulk deformation processing of fcc metals. *Journal of the Mechanics and Physics of Solids*, 40

- (3):537–569, 1992.
- [100] S. R. Kalidindi. Modeling anisotropic strain hardening and deformation textures in low stacking fault energy fcc metals. *International Journal of Plasticity*, 17(6):837–860, 2001.
- [101] A. D. Rollett. *Strain hardening at large strains in aluminum alloys*. PhD thesis, Drexel University, Philadelphia, 1988., 1988.
- [102] A. D. Rollett, R. A. Lebensohn, M. Groeber, Y. Choi, J. Li, and G. S. Rohrer. Stress hot spots in viscoplastic deformation of polycrystals. *Modelling and Simulation in Materials Science and Engineering*, 18(7):074005, 2010.
- [103] U. F. Kocks, A. S. Argon, and M. F. Ashby. Thermodynamics and Kinetics of Slip. *Progress in Materials Science*, 19:1–291, 1975.
- [104] G. I. Taylor. The Mechanism of Plastic Deformation of Crystals. Part I. Theoretical. *Proceedings of the Royal Society A*, 145(855):362–387, 1934.
- [105] P. Franciosi, M. Berveiller, and A. Zaoui. Latent hardening in copper and aluminium single crystals. *Acta Metallurgica*, 28(3):273–283, 1980.
- [106] R. Madec, B. Devincere, and L. P. Kubin. From Dislocation Junctions to Forest Hardening. *Physical Review Letters*, 89(25), 2002.
- [107] D. Cereceda, A. Stukowski, M. R. Gilbert, S. Queyreau, L. Ventelon, M-C Marinica, J. M. Perlado, and J. Marian. Assessment of interatomic potentials for atomistic analysis of static and dynamic properties of screw dislocations in W. *Journal of Physics: Condensed Matter*, 25(8):085702–, 2013.
- [108] D. Weygand, M. Mrovec, T. Hochrainer, and P. Gumbsch. Multiscale Simulation of Plasticity in bcc Metals. *Annual Review of Materials Research*, 45(1):369–390, 2015.
- [109] S. J. Basinski and Z. S. Basinski. *Dislocations in solids, vol. 4*, chapter Plastic deformation and work hardening, pages 261–362. North Holland, Amsterdam, 1979.
- [110] S. Aubry, S. P. Fitzgerald, S. L. Dudarev, and W. Cai. Equilibrium shape of dislocation shear loops in anisotropic  $\gamma$ -Fe. *Modelling and Simulation in Materials Science and Engineering*, 19(6):065006–, 2011.
- [111] C. Teodosiu, J. L. Raphanel, and L. Tabourot. Finite element simulation of the large elasto-plastic deformation of multicrystals. In A.A. Balkema, editor, *Large plastic deformation : fundamental aspects and application to metal forming*, pages 153–168, Rotterdam, 1993.

- [112] U. F. Kocks and H. Mecking. Physics and phenomenology of strain hardening: the FCC case. *Progress in Materials Science*, 48(3):171–273, 2003.
- [113] R. Madec and L. P. Kubin. Second-order junctions and strain hardening in bcc and fcc crystals. *Scripta Materialia*, 58(9):767–770, 2008.
- [114] V. V. Bulatov, L. L. Hsiung, M. Tang, A. Arsenlis, M. C. Bartelt, W. Cai, J. N. Florando, M. Hiratani, M. Rhee, G. Hommes, T. G. Pierce, and T. D. de la Rubia. Dislocation multi-junctions and strain hardening. *Nature*, 440(7088):1174–1178, 2006.
- [115] U. Essmann and H. Mughrabi. Annihilation of dislocations during tensile and cyclic deformation and limits of dislocation densities. *Philosophical Magazine A*, 40(6):731–756, 1979.
- [116] L. P. Kubin, B. Devincere, and T. Hoc. Inhibited dynamic recovery and screw dislocation annihilation in multiple slip of fcc single crystals. *Philosophical Magazine*, 86(25-26):4023–4036, 2006.
- [117] A. Mapar, D. Kang, T. R. Bieler, F. Pourboghrat, and C. C. Compton. A comparative study of stress update algorithms for rate-independent and rate-dependent crystal plasticity Nb. In *Proceedings of SRF2015*, number MOPB057, 2015.
- [118] A. Mapar, H. Ghassemi-Armaki, F. Pourboghrat, and K. S. Kumar. A differential-exponential hardening law for non-Schmid crystal plasticity finite element modeling of ferrite single crystals. *International Journal of Plasticity*, 91:268–299, 2017.
- [119] J. L. Bassani and T-Y Wu. Latent Hardening in Single Crystals II. Analytical Characterization and Predictions. *Proceedings of the Royal Society A: Mathematical, Physical and Engineering Sciences*, 435(1893):21–41, 1991.
- [120] E. A. Calnan and C. J. B. Clews. LXV. The development of deformation textures in metals.—Part II. Body-centred cubic metals. *The London, Edinburgh, and Dublin Philosophical Magazine and Journal of Science*, 42(329):616–635, 1951.
- [121] T. E. Mitchell and W. A. Spitzig. Three-stage hardening in tantalum single crystals. *Acta Metallurgica*, 13(11):1169–1179, 1965.
- [122] D. P. Ferriss, R. M. Rose, and Wulff. J. Deformation of tantalum single crystals. *Trans. AIME Metall. Soc*, 224:975–81, 1962.
- [123] L. Dezerald, D. Rodney, E. Clouet, L. Ventelon, and F. Willaime. Plastic anisotropy and dislocation trajectory in bcc metals. *Nature Communications*, 7:11695, 2016.

- [124] H. Lim, J. D. Carroll, C. C. Battaile, T. E. Buchheit, B. L. Boyce, and C. R. Weinberger. Grain-scale experimental validation of crystal plasticity finite element simulations of tantalum oligocrystals. *International Journal of Plasticity*, 60:1–18, 2014.
- [125] A. Zeghadi, S. Forest, A-F Gourgues, and O. Bouaziz. Ensemble averaging stress–strain fields in polycrystalline aggregates with a constrained surface microstructure – Part 2: crystal plasticity. *Philosophical Magazine*, 87(8-9):1425–1446, 2007.
- [126] C. Zhang, H. Li, P. Eisenlohr, W. J. Liu, C. J. Boehlert, M. A. Crimp, and T. R. Bieler. Effect of realistic 3D microstructure in crystal plasticity finite element analysis of polycrystalline Ti-5Al-2.5Sn. *International Journal of Plasticity*, 69:21–35, 2015.
- [127] M. Diehl, P. Shanthraj, P. Eisenlohr, and F. Roters. Neighborhood influences on stress and strain partitioning in dual-phase microstructures. An investigation on synthetic polycrystals with a robust spectral-based numerical method. *Meccanica*, 51(2):429–441, 2016.
- [128] H. F. Poulsen. An introduction to three-dimensional X-ray diffraction microscopy. *Journal of Applied Crystallography*, 45(6):1084–1097, 2012.
- [129] J. Oddershede, S. Schmidt, H. F. Poulsen, H. O. Sørensen, J. Wright, and W. Reimers. Determining grain resolved stresses in polycrystalline materials using three-dimensional X-ray diffraction. *Journal of Applied Crystallography*, 43(3):539–549, 2010.
- [130] J. Oddershede, B. Camin, S. Schmidt, L. P. Mikkelsen, H. O. Sørensen, U. Lienert, H. F. Poulsen, and W. Reimers. Measuring the stress field around an evolving crack in tensile deformed Mg AZ31 using three-dimensional X-ray diffraction. *Acta Materialia*, 60(8):3570–3580, 2012.
- [131] S. F. Li, J. Lind, C. M. Hefferan, R. Pokharel, U. Lienert, A. D. Rollett, and R. M. Suter. Three-dimensional plastic response in polycrystalline copper via near-field high-energy X-ray diffraction microscopy. *Journal of Applied Crystallography*, 45(6):1098–1108, 2012.
- [132] W. Ludwig, S. Schmidt, E. M. Lauridsen, and H. F. Poulsen. X-ray diffraction contrast tomography: a novel technique for three-dimensional grain mapping of polycrystals. I. Direct beam case. *Journal of Applied Crystallography*, 41(2):302–309, 2008.
- [133] G. Johnson, A. King, M. G. Honnicke, J. Marrow, and W. Ludwig. X-ray diffraction contrast tomography: a novel technique for three-dimensional grain mapping of polycrystals. II. The combined case. *Journal of Applied Crystallography*, 41(2):310–318, 2008.
- [134] M. A. Groeber and M. A. Jackson. DREAM.3D: A Digital Representation Environment for the Analysis of Microstructure in 3D. *Integrating Materials and Manufacturing Innovation*, 3(1):5, 2014.

- [135] H. Moulinec and P. Suquet. A fast numerical method for computing the linear and nonlinear properties of composites. *Comptes rendus de l'Académie des sciences. Série II, Mécanique, physique, chimie, astronomie*, 318:1417–1423, 1994.
- [136] H. Moulinec and P. Suquet. A numerical method for computing the overall response of nonlinear composites with complex microstructure. *Computer Methods in Applied Mechanics and Engineering*, 157(1-2):69–94, 1998.
- [137] R. A. Lebensohn. N-site modeling of a 3D viscoplastic polycrystal using fast Fourier transform. *Acta Materialia*, 49(14):2723–2737, 2001.